MSc Thesis

Aeropropulsive Design Optimization Studies of a Blended Wing Body Aircraft

Shubham Deshmukh

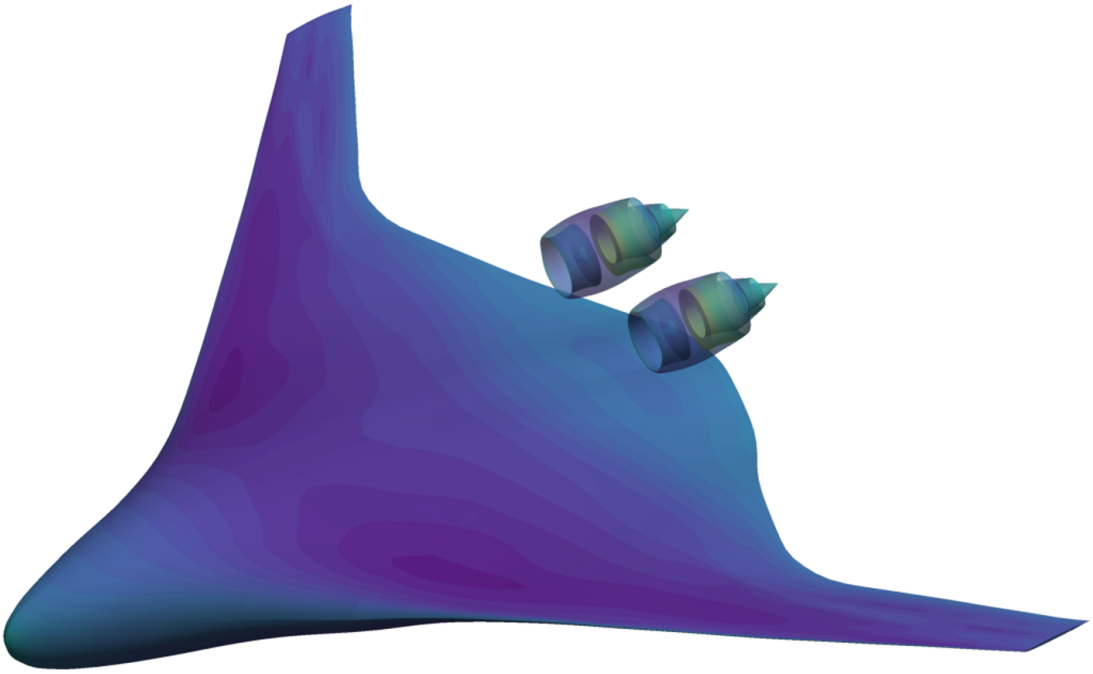

TU Delft

MDO Lab

MASTERS THESIS

AEROPROPULSIVE DESIGN OPTIMIZATION STUDIES OF A BLENDED WING BODY AIRCRAFT

In partial fulfillment towards the degree of
Master of Science at Delft University of Technology

by

Shubham DESHMUKH

Composition of the thesis committee:

Dr.ir. B.W. van Oudheusden	*Chair*	Delft University of Technology
Dr.ir. Alexander van Zuijlen	*Supervisor*	Delft University of Technology
Dr.ir. Gianfranco la Rocca	*Examiner*	Delft University of Technology
Prof. Joaquim R. R. A. Martins	*External Supervisor*	University of Michigan, Ann Arbor
ir. Alasdair Christison Gray	*Invited Member*	University of Michigan, Ann Arbor

To humanity:

We are all tourists on Earth.
May we all live in harmony and die in tranquillity.

CONTENTS

ACKNOWLEDGEMENTS

Around December 2020, I came coming across some YouTube videos from the MDO lab on Aerodynamic Shape Optimization and watched Shamsheer's PhD defense. Curious about their work, I cold texted Marco on LinkedIn and asked about his experience at UM and TU Delft. His answer was probably one of the most thorough and helpful than I had received from any person before. At that time I did not apply for a PhD at UM, but came to Delft to pursue a masters because I wanted to be thorough (perfectionist tendencies are hard to go away). Fast-forward to today, I am finishing my MSc at TU Delft with my thesis at the MDO lab. I have been fortunate to get the best of both worlds. This was only possible thanks to Prof. Martins who welcomed me at the MDO Lab and Dr. Alexander who jointly supervised me from Delft during the course of this thesis.

I my almost three years at TU Delft, I have hardly spent one full year in Delft. This is partly because I wanted to travel and experience living in different countries, and also because TU provided me with that flexibility. As cool as it was for me to live in three different countries during these three years, shifting places every couple of months was equally hard. Not because I had to change 7 apartments in 3 years, but because I had to leave all the new friends I met and those beautiful places behind. This journey would not have been possible without all the great friends and colleagues that I met during these years, who made made it a journey worth reliving. I want to thank all these people from the bottom of my heart.

To all the MDO lab mates: Anil, Ali, Alex^2, Andrew, Cody, David, Eirikur, Eytan, Hannah, Hugo, Josh, Lucas, Marco, Marie, Sabet, Saja, Sham, Shugo and Yingqian. Thank you for making me feel so welcome at the lab, and for helping out with all the bugs, my installation cries and brainstorming sessions to bearing with my working hours. I hope the counter on the white board, asking about my whereabouts, has stopped. Wish you all great success and happiness in your future!

To all the beautiful people in Ann Arbor and UM who made the city feel like home: Rishav, Stefanie, Ankita, Avinash, Daksh, Pratik, Paul, Huseyin, Miles, Saurav, Srikar, Vishwa and the pugs: Violet, Hugo, Poppy and Chumlee. I can't outline the importance that you all have played in my time in Ann Arbor. Thank you for all the love and support that you have given to me!

To my friends and flatmates from Delft: Pranav, Kavin, Vishruti, Siddharth[2], Pratik[2], Srijit, Gopal, Prajwal, Shubham, Felix, George, Amit, Ravi and all others who I might have missed. Thank you for sticking with me throughout these years, even when I was away from Delft. And my faraway friends from undergrad and school who have stuck with me for more than a decade (or two), thank you for bearing me all this while. To my family, who have been there all along and have sufficed with just video calls and sparse visits since I left my hometown 14 years ago. Thank you for being my life long support.

To all my friends, colleagues, supervisors, and family: thank you for being a part of this journey. I hope I have added at least a small amount of value to your lives compared to all that you have added to mine. As a friend once said to me before we departed:

'Le Monde est Petit'

We WILL meet again!
Thank you for all your love,
Shubham

List of Figures

List of Tables

NOMENCLATURE

ANK	Approximate Newton-Krylov
AoA	Angle of attack
AXIS	axisymmetric
AZ	Actuator zone
BC	Boundary condition
BLI	Boundary Layer Ingestion
BPR	Bypass Ratio
BWB	Blended Wing Body
CFD	Computational Fluid Dynamics
CRM	Common Research Model
CTW	Conventional Tube and Wing
DOE	Design of Experiments
DV	Design variable
FFD	Free-form deformation
FPR	Fan Pressure Ratio
HBTF	High Bypass Turbofan
HPC	High Pressure Compressor
IATA	International Air Transport Association
iCST	intuitive Class-Shape Transformation
IDF	Individual Discipline Feasible
IDWarp	Inverse Distance Warping
L0	Finest mesh
L1	Fine mesh
L2	Coarse mesh
L3	Coarsest mesh
LE	Leading edge
LPC	Low Pressure Compressor
MACH	Framework for MDO of aircraft configurations with high fidelity
MDAO	Multi-Disciplinary Analysis and Optimization
MDF	Multiple Discipline Feasible
MDO	Multi-Disciplinary Optimization
MOO	Multi-Objective Optimization
MTOW	Maximum Take-Off Weight
NAXIS	non-axisymmetric
NM	Nautical Miles
OWN	Over-the-Wing Nacelle
PR	Pressure Recovery
RANS	Reynolds-Averaged Navier-Stokes
SLS	Sea Level Static
SNOPT	Sparse Nonlinear OPTimizer
TE	Trailing edge
TIT	Turbine Inlet temperature
TSFC	Thrust Specific Fuel Consumption
XDSM	eXtended Design Structure Matrix

$\bar{\rho}$	averaged density
$\bar{p_s}$	averaged static pressure
$\bar{V_x}$	averaged velocity in x-direction
$\Delta x, w$	horizontal wing displacement DV
$\Delta z, w$	vertical wing displacement DV
$\dot{m}_13$	mass flow rate at bypass exit
$\dot{m}_2$	mass flow rate at fan face
$\dot{m}_7$	mass flow rate at core exit
$\dot{m}_{fuel}$	engine fuel consumption rate
η	efficiency
η_i	inlet efficiency
v_∞	freestream velocity
ρ	density
ρ_13	density at bypass exit
ρ_2	density at fan face
ρ_7	density at core exit
AoA_w	angle of attack of the wing
$area_2$	density at fan face
$area_7$	area at core exit
$area_{13}$	area at bypass exit
C_l	lift coefficient
$C_{D,w+nac}$	combined drag coefficient of wing and nacelle
$C_{D,nac}$	drag coefficient of nacelle
$C_{D,w}$	drag coefficient of wing
$C_{L,w_{con}}$	lift constraint on the wing
$C_{L,w}$	lift coefficient of wing
C_p	pressure coefficient
D_{nac}	nacelle drag
D_w	wing drag
F_m	momentum force
F_p	pressure force
F_S	force on the surface
F_{net}	net force
$g_{geo,e}$	geometric/thickness constraints on the engine
$g_{geo,w}$	geometric/thickness constraints on the wing
$g_{vol,w}$	volumetric constraint on the wing
M	Mach number
M_2	Mach number at fan face
M_∞	freestream Mach number
p_s	static pressure
p_t	total pressure
p_∞	freestream pressure
$R_{\dot{m}}$	mass flow rate residual
R_{ρ_s}	density residual
R_{area_s}	area residual
R_{p_s}	static pressure residual
T_t	total temperature
$X_{shape,e}$	engine shape design variables
$X_{shape,w}$	wing shape design variables

ABSTRACT

With the increasing demand for flights, the environmental impact of aviation is on the rise. To tackle this challenge, it is necessary to look into the design of unconventional aircraft configurations and engine design improvements to improve overall fuel efficiency. The Blended Wing Body (BWB) aircraft is one of the most promising unconventional configurations for future airliners. Several studies have looked at the design optimization of the BWB and its engine-integration effects. However, most of these studies were limited by either a lack of coupling between the aerodynamic and propulsion models or restricted design freedom for nacelle design and engine-airframe integration. Thus, there is a need to explore the benefits of aeropropulsive trade-offs using non-axisymmetric nacelle designs and refining its relative placement above the wing.

The work performed in this thesis focuses on realizing these aeropropulsive trade-offs by optimizing the engine and the BWB wing simultaneously using selectively non-axisymmetric engine design variables, including design variables for wing shape and engine placement. To achieve this objective, a free-form deformation (FFD) based parameterization scheme is developed for non-axisymmetric engine parameterization along with design variables for modifying wing shape and relative engine placement. ADflow CFD solver is used for the aerodynamic discipline, and the PyCycle thermodynamic cycle library is used for the propulsion discipline. Coupled aeropropulsive optimizations are performed by extending the MACH-Aero framework using coupled derivatives in an Individual Discipline Feasible (IDF) architecture for gradient-based optimization using the SNOPT optimization algorithm.

A set of studies are performed to establish the effectiveness of the proposed FFD-based parameterization for engine optimization in isolation. Later, the engine is mounted onto the BWB in an over-the-wing configuration, and the effect of non-axisymmetric engine design is explored in conjunction with engine placement and wing shape modifications. Optimizing the engine location with axisymmetric nacelle and wing shape design variables reduces the wing drag by 11.5% and engine fuel consumption by 2.3% compared to the baseline engine location. Using non-axisymmetric nacelle design variables further drops the fuel consumption by 1.1%. A comparison of this optimized engine-airframe design with an optimized engine in isolation shows that placing the engine in an over-the-wing configuration with the BWB reduces the thrust-specific fuel consumption by 4.4%. Non-axisymmetric nacelle design also improves the quality of engine inflow by eliminating local super velocities at the inlet lip. This study shows the benefits of an OWN configuration for the BWB and quantifies the performance gains from optimizing the engine location with non-axisymmetric nacelles.

1

INTRODUCTION

The aviation industry currently produces about 2.5-3% of global CO_2 emissions[1]. With the growing demand for commercial aviation, at a rate of 4.4% per annum[2], these emissions are expected to rise rapidly in the coming years. Thus, there is an urgent need to transition towards sustainable aviation to achieve the goal of net zero emissions. Two main drivers to achieve this goal are: *evolution of current aircraft designs to make them more fuel-efficient* and *transition to sustainable fuels* [3]. These transitions will serve the aviation industry not only from a viewpoint of sustainability, but it will also lead to a reduction in fuel costs due to increased efficiencies, which, in turn, will help make commercial flights cheaper and more accessible.

Since the beginning of commercial flight, there have been gradual improvements in aircraft design, but the Conventional Tube and Wing (CTW) architecture has remained the same. Figure 1.1 shows the evolution of aircraft designs over the last century and the associated "stair-step" changes with dotted lines. To make a significant step change in the progress towards sustainable aviation, it is imperative that we transition to more promising unconventional aircraft concepts like the Blended Wing Body (BWB), also called Hybrid Wing Body (HBW), and high aspect ratio wing designs like the Truss-Braced Wing (TBW) [2].

The BWB aircraft is one of the most promising unconventional configuration [2]. Liebeck [4] proposed a long-range second-generation Boeing BWB aircraft, which showed a 27% reduction in fuel burn per seat mile at 2010 technology levels. The future BWB designs with advanced airframe and propulsion technologies hold the promise to reduce fuel consumption by about 39% with respect to the current Boeing-777-like aircraft and about 12% as compared to the advanced CTW designs with the same future technology assumptions [5]. The 2050 Aircraft Technology Net Zero Roadmap by IATA puts the BWB concept in a similar range of 13-18% efficiency gains with future technology levels [3]. This reduction in fuel consumption is mainly possible due to the lower drag of the BWB design, which has a lift-to-drag (L/D) ratio in the range of about 21-26, compared to 15-20 for the CTW aircraft [6]. The BWB concept is also better suited for carrying future fuels, like hydrogen, more efficiently than the CTW aircraft and has a significant potential for noise reduction [3, 5, 7].

1

Aircraft design is a highly coupled aspect that depends upon the interaction of multiple disciplines, like aerodynamics, propulsion, structure, and controls, to converge to a feasible design. Multi-disciplinary optimization (MDO) provides a way to simultaneously optimize aircraft design for multiple disciplines at once to reach feasible optimal designs. The current study utilizes an MDO methodology to conduct aeropropulsive design optimizations of a reference BWB aircraft concept proposed by Boeing [4]. A detailed literature review performed later in this chapter shows that while most previous aeropropulsive optimization studies for BWBs were based on uncoupled multi-disciplinary analysis methods, only a few studies have focused on the aeropropulsive coupling for the BWB design optimization. But most of these studies were limited by the design freedom for engine shape modification and its relative location on the wing. These design variables are found to have a significant impact on performance of the integrated engine and airframe [8, 9]. Thus, there is a need to look into the coupled aeropropulsive optimization of engine-integrated airframe configurations for the BWB aircraft with an enlarged design space for engine design and placement.

To achieve this objective, an FFD-based parameterization scheme is developed in this study to perform coupled aeropropulsive design optimizations using the MACH-Aero framework in conjunction with PyCycle [10], which is a thermodynamic cycle modeling library built on top of the OpenMDAO framework. The FFD-based parameterization scheme allows for a significantly larger design space than other commonly used engine parameterization methods, including provisions for non-axisymmetric nacelle modifications. This aeropropulsive optimization methodology is then used to understand the changes in optimal engine designs for different thrust requirements. In addition, an aerodynamic optimization study is performed for the reference BWB aircraft wing in isolation. Finally, the engine and wing designs are integrated and optimized simultaneously to understand the effect of engine integration and placement on wing drag and engine fuel consumption. These studies are performed with varying levels of design freedom to quantify the benefits of the proposed parameterization scheme.

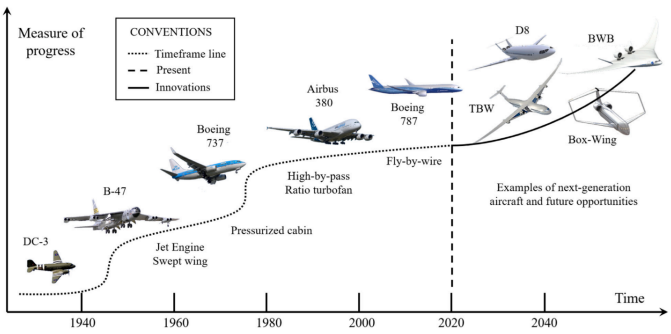

Figure 1.1: Evolution of aircraft designs and features over the years [2]

1.1. BACKGROUND OF AEROPROPULSIVE DESIGN OPTIMIZATION METHODS FOR AERO-ENGINES

This section outlines the current trends of methods used in aeropropulsive design optimization studies in the literature. Firstly, a distinction between coupled and uncoupled aeropropulsive optimization methods is made to understand the differences in the two approaches and their applicability for different problems. Next, multiple approaches for modelling the engine intake fan and core are discussed with their suitability to the type of application. Lastly, a description of the prominent engine parameterization schemes used in the literature is provided, along with their limitations.

THE NEED FOR COUPLED AEROPROPULSIVE OPTIMIZATION

According to Gray [11], coupled aeropropulsive analysis models capture the affect of the aerodynamics on the propulsion system and vice versa, simultaneously. Hence, in these cases both the propulsion and the aerodynamics model update with the changes in the operating conditions or geometry changes in the other model. While the uncoupled models are useful in making first order engineering approximations [11], they are not useful where there is a strong coupling between the flow field and the engine performance, for example, in a boundary-layer ingestion (BLI) engine. Renganathan *et al.* [9] demonstrated that for a trailing edge mounted over-the-wing nacelle (OWN), the engine pressure recovery is strongly dependent on the airframe aerodynamics, while the installation drag is weakly affected by the engine setting. In such cases, a coupling between the propulsion and the aerodynamics model is needed to accurately predict the engine performance and installation penalty. Yildirim *et al.* [12] also state that this coupled nature is essential for off-design conditions when performing multi-point aeropropulsive optimizations. As such, the propulsion or nacelle design optimization studies which use uncoupled analysis models cannot realize the benefits of aeropropulsive trade-offs and the prediction accuracy that is obtained by using coupled aeropropulsive models.

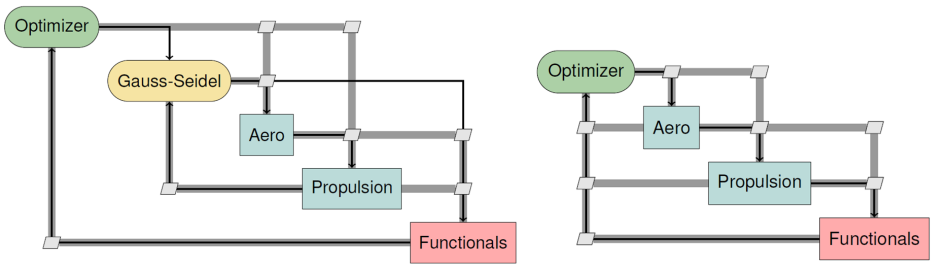

(a) MDF architecture for aeropropulsive MDO (b) IDF architecture for aeropropulsive MDO

Figure 1.2: XDSMs of MDF and IDF architectures for a notional aeropropulsive design optimization problem [11]

1

In the scenario of multi-disciplinary design optimization, a strong coupling ideally means that the aerodynamic and propulsion model solutions are consistent with each other. However, in an MDO involving the aerodynamics and propulsion disciplines, this coupling can be achieved using both the multi-disciplinary feasible (MDF) and the individual-discipline feasible (IDF) architectures. Figure 1.2 shows the XDSMs of MDF and IDF architectures applied to a notional aeropropulsive design optimization problem. While the MDF architecture maintains consistency between the disciplines within each optimizer iteration, it requires a non-linear solver to bring this consistency in both the disciplines. This approach is required in the actuator zone based fan modelling approach that is discussed above. On the other hand, in an IDF architecture the two disciplines are coupled using consistency constraints. As such, in an IDF architecture the disciplines can remain infeasible (loosely coupled) in the initial iterations of the optimizer, but as the optimization converges, they become feasible or tightly coupled.

CFD MODELLING APPROACHES FOR ENGINE INTAKE FAN AND CORE

While there has been significant progress on the analysis front for turbofan engine design and integration, the computational cost of detailed CFD analysis of full engine flow path, like the one carried out by Turner *et al.* [13] for the GE90 engine, is still very prohibitive. This computational cost gets even more pronounced when the engine design needs to be be integrated with the airframe and optimized. However, the mean effect of fan blades and core on the flow field can be represented using much simpler, cost-effective alternatives, like an actuator zone (AZ) or inlet-outlet boundary conditions (BC) for the rotor, instead of modelling the actual rotor blades in the CFD domain.

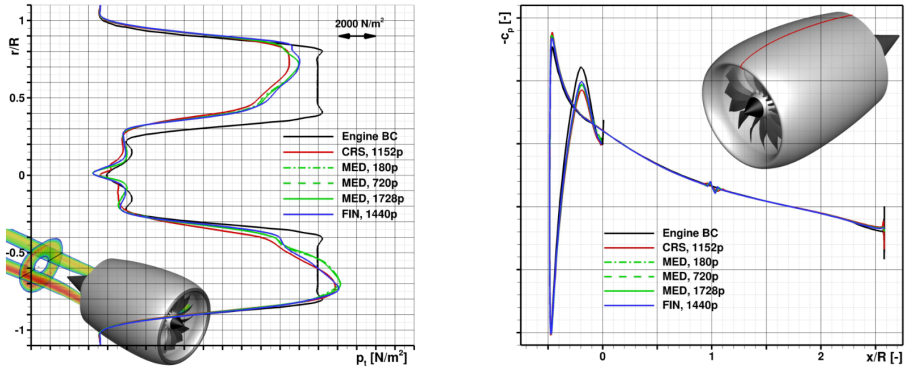

(a) Total pressure in the jet stream at 1D

(b) Nacelle pressure on the top section

Figure 1.3: Comparison of CFD modelling approaches for a HBTF: BC is the boundary condition RANS model; CRS, MED, FIN are coarse, medium and fine mesh results for the URANS analysis with rotor blades [14]

Stuermer [14] carried out a detailed comparison of the BC method and a full fan rotor with guide vanes for a UHBPR turbofan. This study showed that the main drawback of using a BC model was its inability to capture the azimuthal non-uniformity in the exhaust stream (see Figure 1.3a). In cases where the wing is not in the wake of the engine, like in the over-the-wing-nacelle (OWN), the effects of exhaust non-uniformity can be assumed to be non-vital for the prediction of integrated quantities. Additionally, the pressure profile over the nacelle was captured equally well in both the models (see Figure 1.3b). This characteristic of the BC model is desirable since it is able to capture the forces on the engine nacelle without significant deviation from the full blade model. The forces on the fan inlet and outlet can then be averaged on the boundary surfaces and the net engine thrust can be determined relatively accurately. Another fan modelling approach is the AZ model which models the effect of the fan by distributing a prescribed source term for the fan force uniformly across the actuator zone volume. This approach can also model the flow rotation induced by the fan which which is necessary for accurate prediction of fan face distortion [12].

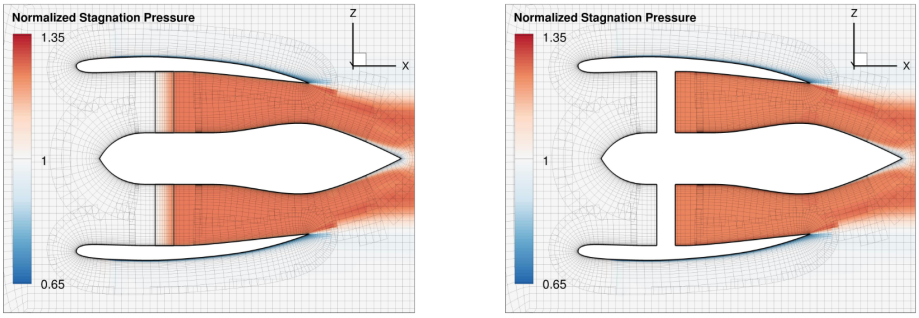

(a) AZ approach for modelling the fan effect (b) BC approach for modelling the fan effect

Figure 1.4: BC and AZ Approaches for modelling the fan effect in a podded fan: contours of total pressure show pressure jump across the fan [12]

Yildirim *et al.* [12] demonstrated the use of both AZ and BC approaches for modelling a podded fan using the ADflow CFD solver and coupling it with the PyCycle thermodynamic library to perform coupled aeropropulsive design optimization. Figure 1.4 shows the total pressure jump achieved across the modelled fan using the AZ and BC approaches. Although the AZ approach is slightly more accurate than the BC approach, it is difficult to converge inside the CFD model and the aeropropulsive coupling in this case requires an additional non-linear solver to converge the CFD and propulsion models together. The BC approach is straight forward and easier to implement as it can be modelled using a simple feed-forward coupling from the CFD to the propulsion model and the aeropropulsive coupling can be established using consistency constraints [15]. The AZ model may be more desirable in off-design conditions where the non-adiabatic losses are more

pronounced than the cruise condition [12]. Further studies by Lamkin *et al.* [16] have used a hybrid approach for modelling a turbofan engine in ADflow by using an AZ approach to represent the flow through the intake fan and a BC approach to represent the flow through the engine core using a feed-back coupling mechanism to satisfy the coupling between the CFD and propulsion models.

ENGINE PARAMETERIZATION SCHEMES AND OPTIMIZATION FRAMEWORKS

Coupled aeropropulsive design optimization studies by Gray *et al.* [15], Yildirim *et al.* [12], Lamkin *et al.* [16] and Abdul-Kaiyoom *et al.* [17] used OpenMDAO's MPhys framework [1] for high-fidelity optimization using the gradient-based optimizer SNOPT [18]. The CFD gradients were calculated using the adjoint method in the ADflow solver and the total derivatives for the coupled problem were calculated using the in-built modular analysis and unified derivatives (MAUD) architecture [19] in OpenMDAO. In these studies, the parameterization technique was based on engine cross-sections which are controlled through OpenVSP's geometry engine within the PyGeo library [20]. Figure 1.5 shows the OpenVSP based parameterization scheme used by Yildirim *et al.* [12] for a podded fan case. These studies were limited to circular and (super)elliptical cross-sections for the front nacelle.

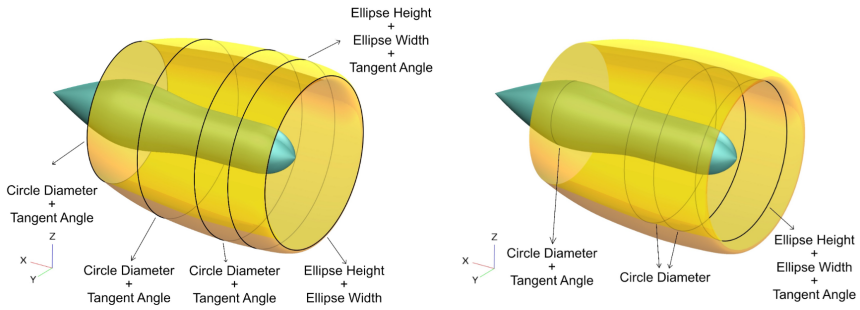

Figure 1.5: OpenVSP based nacelle parameterization used by Yildirim *et al.* [12]

Studies by Tejero *et al.* [8, 21] focused on multi-objective aerodynamic optimization of short nacelle HBPR engines using the BC approach discussed earlier. They used an intuitive Class Shape Transformations (iCST) based parameterization for the HBPR engine geometry which is capable of producing non-axisymmetric nacelle and exhaust designs, as well as changes in droop and scarf angle. Figure 1.6 shows the iCST based aero-line design variables used by Tejero *et al.* [21]. Their study demonstrated a variation of 3.5% in the nacelle mid-cruise drag between three optimal candidates for different values of the droop and scarf angles. This signifies the potential of using non-axisymmetric nacelle designs for drag reduction, especially in the front nacelle. However, these studies did not quantify the gain in engine fuel efficiency for this reduction in nacelle drag.

[1] MPhys: https://github.com/OpenMDAO/mphys

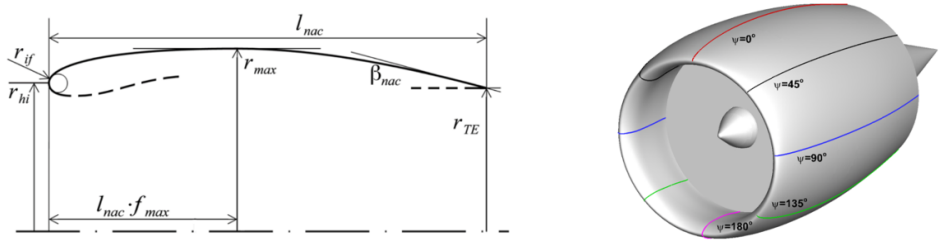

(a) iCST-based design variables on a single aeroline (b) Aerolines along the 3D nacelle

Figure 1.6: iCST aero-line based non-axisymmetric nacelle design variables [21]

Studies carried out by Tejero *et al.* [8] employed a genetic algorithm for multi-objective optimization (MOO) of the HBTF which required a large computational cost of 12000 core hours for a single MOO with CFD in-the-loop. They were able to bring down this cost by 50% using surrogate models but with an added minimum uncertainty of 1.5% with respect to the CFD in-the-loop approach. With this 50% reduction in computational cost to 6000 core hours, the computational cost of using a genetic algorithm is still very high and increases rapidly with increasing number of design variables. On the other hand, the gradient-based optimization approach used by Yildirim *et al.* [12] required only about 400-500 core hours. Such a large optimization run-time is expected when using gradient-free algorithms due to a large number of function evaluations. Figure 1.7 shows the scaling of both the gradient-based and free algorithms. The gradient-free algorithms scale almost exponentially, while the gradient-based algorithms scale much better for increasing number of design variables.

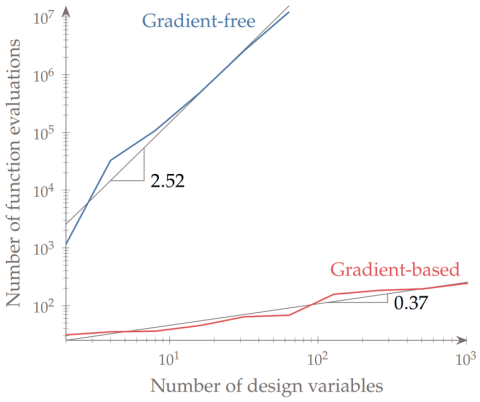

Figure 1.7: Scaling of gradient-based and gradient-free algorithms with the number of design variables [22]

1

1.2. THE CASE FOR COUPLED AEROPROPULSIVE DESIGN OPTIMIZATION OF ENGINE-INTEGRATED BWB

One of the earliest implementations of coupled aeropropulsive optimization using gradient based optimization can be traced to the work of Rodriguez [23] in 2001. Rodriguez applied a coupled aeropropulsive approach to optimize three podded nacelles for a BWB aircraft using powered boundary conditions (single-stream exhausts) in CFL3D CFD solver. A later study by Rodriguez [24] looked into aeropropulsive optimization of BLI inlets for the BWB aircraft. These studies used the complex step method for gradient calculations, which proved to be tedious for a large number of design variables. Therefore, these studies were limited to a small number of design variables and were mostly focused on demonstration of the capability to perform aeropropulsive optimization for such a complex problem. Despite a limited number of design variables, which did not include spanwise movement of the nacelle, this study showed a substantial 10% reduction in fuel burn rate compared to the baseline aircraft for the podded nacelle case. The optimizer achieved this by raising the height of the center pylon and increasing the yaw angles of the outboard nacelles to reduce the shock strength in the channels between the nacelles and the wing as shown in Figure 1.8. This study demonstrated the benefits that can be obtained through coupled aeropropulsive optimization of engine-integrated BWB configurations.

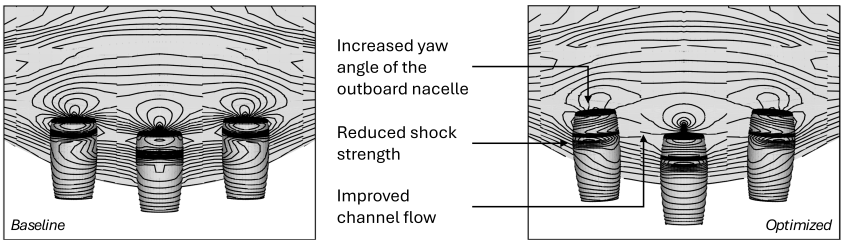

Figure 1.8: Pressure contours over the baseline and optimized podded BWB [24]

Renganathan *et al.* [9] performed detailed sensitivity analysis on aeropropulsive coupling for the Common Research Model (CRM) wing with powered over-the-wing podded nacelle configurations using RANS simulations. This study showed that for a trailing edge mounted OWN configuration:

1. The effect of change in spanwise engine location is a strong factor since it affects the strength and location of shock waves. The authors predicted the presence of a local minima for the installation drag when the inlet nacelle is close to the trailing edge. Vertical motion of nacelle closer to the wing was found to be favourable for drag reduction, but was a statistically weak factor.

2. Engine pressure recovery (PR) varies non-linearly with spanwise engine location and is strongly dependent on the shock on the suction side of the wing. PR improves as the engine moves away from the wing in the vertical direction

Based on these observations, the study concluded that there is a trade-off between installation drag and pressure recovery for the trailing edge mounted OWN. But these sensitivities are applicable only for the fixed wing and nacelle geometries and the authors advice that further optimization studies are necessary to assess the trade-offs between engine pressure recovery and installation drag. Silva *et al.* [25] performed an aerodynamic optimization study for wing redesign with an engine positioning sensitivity study for the CRM wing. This sensitivity study included wing optimization for different nacelle placement. The results of this sensitivity study are presented in Figure 1.9, which are in-line with the study of Renganathan *et al.* [9] and show that for an OWN configuration, the optimum nacelle location is closer to the trailing edge. However, this study lacked a thermodynamic propulsion model to capture the coupled aeropropulsive effects on the performance of the engine and also did not take into account the effect of nacelle shape design variables.

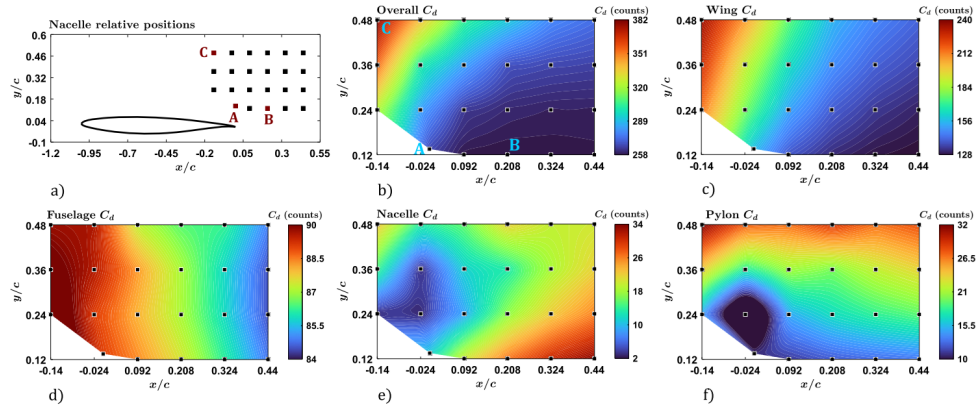

Figure 1.9: Sensitivity study for nacelle positioning. The wing is optimized for every nacelle position, while the nacelle shape is kept the same at a fixed normalized spanwise location of $\eta = 0.33$, with wing $C_l = 0.5$ [25]

Abdul-Kaiyoom *et al.* [17] performed coupled aeropropulsive design optimizations of an over-the-wing podded nacelle configuration for the CRM wing. These studies used circular and super-elliptical engine cross-sections for nacelle parameterization, as discussed in section 1.1, and also took into account the effect of change in fan pressure ratio (FPR). Although, the flow through the engine was modelled using a single nozzle, assuming a very high bypass ratio, hence the actual effect of change in bypass ratio could not be observed. Also, the changes in engine fuel consumption could only be observed using an indirect reference of the shaft power. Similar to previous studies, these optimizations were also limited to parametric studies for engine placement. This limitation was attributed to the difficulties involved with volume mesh warping for overset meshes.

Table 1.1: A summary of relevant aeropropulsive optimization studies along with the contributions of the current work

Author	CFD solver	Propulsion model	Aeropropulsive coupling	Aircraft [1] type	Optimization [2] type	Fan [3] model	Core [3] model	Wing DV	Nacelle DV	Engine placement DV
Rebassa *et al.* [26]	Fluent [$]	-	uncoupled	CTW_{pod}	GF + DOE	BC	BC	-	non-axisymmetric	-
Tejero *et al.* [27]	Fluent	-	uncoupled	CTW_{pod}	GF + DOE	BC	BC	-	non-axisymmetric	DOE only
Silva *et al.* [25]	Fluent	GASTURB	coupled	CTW_{pod}	DOE [†]	BC	-	limited	-	DOE only
Renganathan *et al.* [9]	StarCCM+	1D cycle	coupled	CTW_{pod}	DOE	BC	BC	-	axisymmetric	DOE only
Kayoom *et al.* [17]	ADflow	PyCycle (1D)	coupled	CTW_{pod}	GB + DOE	BC	-	CST-based	axisym + elliptic	DOE only
Lamkin *et al.* [16]	ADflow	PyCycle (1D)	coupled	-	GB	AZ	BC	-	axisym + elliptic	-
Gray *et al.* [28]	ADflow	PyCycle (1D)	coupled	CTW_{BLI}	GB	BC	- [e]	-	axisym + elliptic	-
Yildirim *et al.* [29]	ADflow	PyCycle (1D)	coupled	CTW_{BLI}	GB	BC	- [e]	-	axisym + elliptic	-
Ahuja *et al.* [30]	StarCCM+	$NPSS_{surrogate}$	coupled	CTW_{pod}	GF + DOE	BC	BC	CST-based	axisymmetric	DOE only
Rodriguez [24]	CFL3D	NEPP (1D)	coupled	BWB_{pod}, BWB_{BLI}	GB	BC	-	limited	axisymmetric	DVs present [‡]
Current study	**ADflow**	**PyCycle (1D)**	**coupled**	**BWB_{pod}**	**GB**	**BC**	**BC**	**FFD-based**	**non-axisymmetric**	**DVs present[*]**

[1] BLI: Boundary layer ingestion engine, pod: podded engine

[2] GF: gradient-free optimization, GB: gradient-based optimization, DOE: design of experiments

[3] BC: boundary conditions represent the fan and core boundaries, AZ: actuator zone model for fan

[$] Euler model was used for optimization, all other studies used RANS-based CFD models

[†] An iterative 2D wing-section reshaping strategy was used to achieve desired sectional lift

[e] An electric fan model was used, so only a single nozzle representing the fan flow is present

[*] Engine placement DVs are present in the wing's frame of reference, i.e., the wing is moved while keeping the engine static

[‡] Spanwise engine translation DV is not present

1.3. OBJECTIVES AND SCOPE OF THIS THESIS

Based on the literature review performed in section 1.1 and section 1.2, it can be concluded that for a trailing edge mounted OWN configuration the engine installation drag, inlet pressure recovery and fuel burn rate are strongly dependent on the relative engine-wing placement. A coupled multi-disciplinary analysis is therefore essential to properly capture the aeropropulsive trade-offs. Table 1.1 summarizes the methods and design variables used in the literature for aeropropulsive optimization studies of CTW and BWB aircraft configurations and the contributions of the current work. While preliminary aeropropulsive design optimization studies have been performed for the BWB and CTW OWN configurations, these studies are limited by the lack of engine placement and non-axisymmetric nacelle shape design variables. Hence, a detailed engine-airframe shape optimization study is needed to realize the full benefits of this aeropropulsive coupling using design variables for engine placement and non-axisymmetric changes in the nacelle, along with a co-axial engine model to observe the effect of bypass-ratio changes on the engine fuel efficiency of high-bypass turbofans.

In view of these observations and research gaps, the **objectives** of this thesis are to:

- *Develop a coupled aeropropulsive optimization strategy for design optimization of a Blended Wing Body aircraft with an over-the-wing mounted high bypass turbofan engine.*
- *Device a selectively non-axisymmetric engine parameterization scheme and study its effect on the optimized engine-airframe performance in combination with the design variables for wing shape modification and engine placement.*

This thesis was performed at the MDO Lab, University of Michigan - Ann Arbor, and the emphasis on utilizing the in-house open-source MACH-Aero framework [2] due to its unique capabilities for gradient-based high-fidelity aerodynamic shape optimization using the ADflow CFD solver [31–33]. Although this framework was initially developed for aerodynamic shape optimization, it has been extended in the past to perform high-fidelity aerostructural optimizations [34, 35]. A package to standardize high-fidelity MDO in OpenMDAO, MPhys, is also under development and has been used in previous studies [12, 16, 17]. However, using the MPhys framework is out of the scope of the current study. The current work focuses on using the established MACH-Aero framework and extending it to perform coupled aeropropulsive optimization in conjunction with the 1D thermodynamic cycle modelling library, PyCycle [10], to demonstrate the framework's compatibility with other multi-fidelity disciplinary analysis tools. Details of this optimization framework and the aeropropulsive coupling are presented in chapter 3.

[2] MACH-Aero: https://github.com/mdolab/MACH-Aero

The second objective of this thesis is to develop a parameterization that not only allows selectively non-axisymmetric engine shape modifications but also supports design variables for wing shape modification and engine placement. This is accomplished using the FFD-based parameterization in the PyGeo [20] library. Based on this FFD-based parameterization scheme, an overlapping FFD approach is proposed for parameterizing the engine geometry. using a combination of overlapping, circular FFD sections with parametric volume bounds. The detailed methodology for engine parameterization is explained later in subsection 3.4.2. The FFD-based wing parameterization strategy is similar to that adopted by Lyu and Martins [36] and is explained in subsection 3.4.1. These parameterization schemes are combined to parameterize the propulsion-integrated airframe configuration for the BWB in subsection 3.4.3.

Based on the gaps identified in the literature and the established research objective, this research addresses the following **research questions**:

1. How does the proposed FFD-based non-axisymmetric parameterization affect the optimization convergence, robustness and the optimized engine design?
    - What impact does the proposed parameterization have on the convergence of the engine optimization? What are the necessary tolerances and computational costs associated with these aeropropulsive optimizations?
    - How does the engine design change during an aeropropulsive optimization in the presence of a non-axisymmetric design space?
    - How does the engine design change for varying levels of thrust requirement? Is the proposed parameterization able to handle these changes?
    - Are there any drawbacks of the proposed parameterization that might affect its usability?
2. What are the differences in the optimized engine and wing designs in independent vs integrated optimizations using the extended design space availed through this parameterization scheme?
    - What is the effect of adding an engine placement DV on the location and performance of the integrated engine-airframe?
    - How do the non-axisymmetric DVs perform in an integrated engine-wing optimization? Is their effect any different from isolated engine optimizations?
    - What are the differences in the performance characteristics of the wing and engine when they are optimized in isolation versus in an integrated configuration?
    - Are there any design features that are present in the optimized integrated designs that can otherwise be overlooked when optimizing the engine and wing in isolation?

1.4. THESIS OUTLINE

This thesis is organized into the following chapters:

- Chapter 1 introduces the research topic and establishes the importance of conducting coupled aeropropulsive optimizations for a BWB aircraft. This is achieved through a thorough literature review, which serves as a motivation to identify the research questions addressed in this thesis.
- Chapter 2 outlines the design and characteristics of the baseline BWB aircraft, detailing the baseline wing and engine design.
- The methodology for performing aerodynamic and aeropropulsive optimizations is presented in Chapter 3. This chapter introduces the optimization framework and provides details of the aeropropulsive coupling approach. The proposed FFD-based engine parameterization scheme is explained, followed by the details of the geometric design constraints and the optimization algorithm used.
- Chapter 4 contains the results of all the optimization studies performed in this work. First, an aerodynamic shape optimization study of the BWB wing is performed in isolation, followed by aeropropulsive optimization studies of an unmounted high-bypass turbofan engine (HBTF). Then, the engine and wing are combined to perform integrated aeropropulsive design optimizations with an increasing number of design variables.
- Finally, the results and findings of this thesis are concluded in Chapter 5, with answers to the research questions established in Chapter 1 and recommendations for future work.

2

BASELINE BWB AIRCRAFT DESIGN

This chapter describes the methodology used for conducting aeropropulsive optimization studies for both isolated engine and wing cases, as well as integrated engine-airframe configurations. It includes detailed descriptions of the geometric parameters, analysis methods, parameterization strategy, design constraints, and optimization techniques. Additionally, this chapter introduces a novel FFD-based methodology for engine design parameterization and explains the development of a robust state coupling between the aerodynamic and propulsion disciplines to facilitate aeropropulsive optimization.

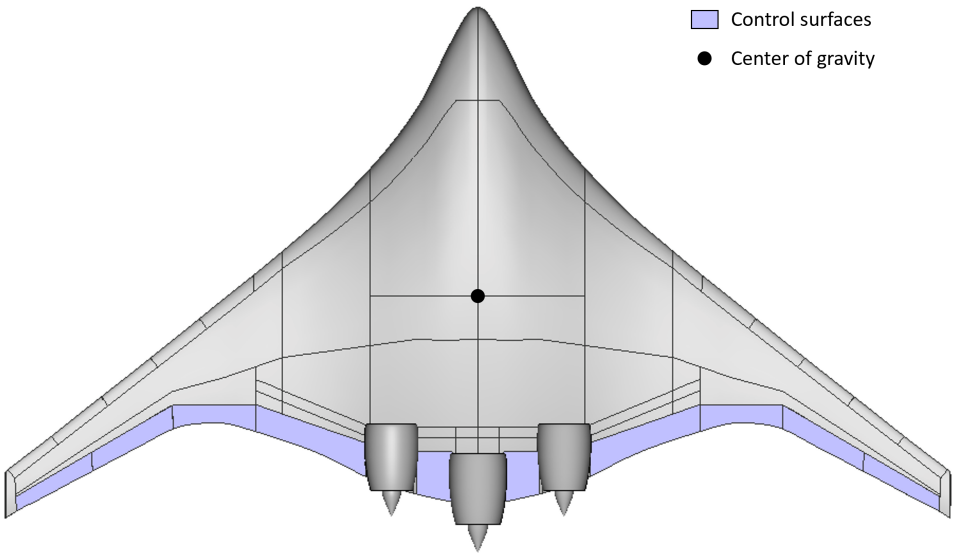

Figure 2.1: Boeing second generation BWB aircraft design in a 3-engine configuration (reconstructed from Liebeck [4])

2.1. AIRCRAFT SPECIFICATIONS

The second-generation Boeing BWB aircraft configuration [4] is used as the baseline aircraft design. This BWB concept is capable of carrying 800 passengers in a double-deck cabin configuration at a cruise Mach number of 0.85, with a range of 7000 nautical miles. The maximum take-off weight (MTOW) of this aircraft is 823,000 pounds [37] and requires 3 turbofans rated at 61,900 pounds static thrust each. Table 2.1 outlines the specifications of this BWB configuration which is represented in Figure 2.1.

Table 2.1: Aircraft specifications for the second generation Boeing BWB [37]

Quantity	Value	Units
Wing span	85.34	m
Length	43.89	m
Wing area	1473	m^2
MTOW	373306	kg
Range	7000	NM
Nominal cruising speed	0.85 M	-

2.1.1. BASELINE WING DESIGN

The baseline wing geometry for the Boeing's second generation BWB is adapted from the work of Lyu and Martins [36], which has a span of 280 ft (excluding winglets) and an overall length of 144 ft. Figure 2.2 shows the baseline BWB wing geometry. The thickness-to-chord (t/c) ratio varies from 18% at the wing centerline to 10% the wing tip. The centerline airfoil is a NASA SC(2)-0518 airfoil, which is interpolated quadratically to a NASA SC(2)-0410 airfoil at the tip.

Although, the second generation BWB concept had a 3-engine configuration, Liebeck *et al.* [38] also studied alternate engine integration architectures. Based on this experimental study, an upper S-Bend 3-engine configuration was chosen due to its BLI benefits, foreign-object damage protection and noise shielding inlets, along with a suitable center-of-gravity location [38].

Parameterization and mesh deformation in a BLI engine configuration would be very complex due to the presence of intricate surface intersections. Also, a 3-engine configuration would require additional solves of the propulsion model and coupled adjoints which would significantly increase the computational cost for the current optimization architecture. Additionally, the BLI engines also require distortion-tolerant intake fans. For these reasons, a 2-engine pod and pylon based BWB configuration was chosen for this study, with each engine rated at 92,850 lbs of sea level static (SLS) thrust.

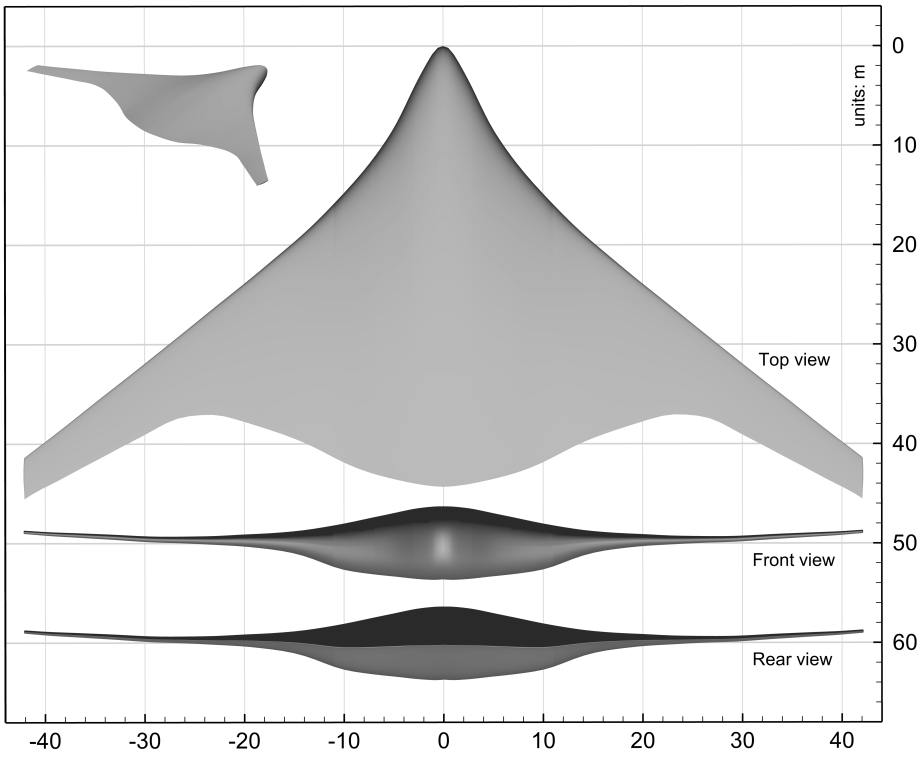

Figure 2.2: Baseline BWB wing design based on the Boeing second generation BWB

2.1.2. BASELINE ENGINE DESIGN

The GE90 engine series boasts a static thrust rating of 94000 lbs, which is close to the required SLS thrust for the 2-engine BWB configuration. Also, close approximations of the geometry and performance of GE90-94B engine are available in the literature. Hence, the GE90-94B engine was chosen as the baseline engine design for this aero-propulsive optimization study.

The GE90-94B engine design was taken from multiple literature sources [39, 40] and overlapped to find the closest common design to be used as a baseline. The engine has a fan diameter of 3.16 m and a total length of 7.29 m. As per the data available for the GE90-94B engine [41, 42], a bypass ratio (BPR) of 8.1 and a fan-pressure ratio of 1.65 (FPR) are chosen for the baseline engine design. The engine has a maximum turbine inlet temperature (TIT) of 1380 K and a fuel consumption rate of about 1.25 kg/s for a cruise thrust of about 72 kN at Mach 0.8 at an altitude of 10668 m (36000 ft) [41]. Table 2.2 and fig. 2.4 show the baseline engine specifications and component efficiencies based on the GE90-94B engine data.

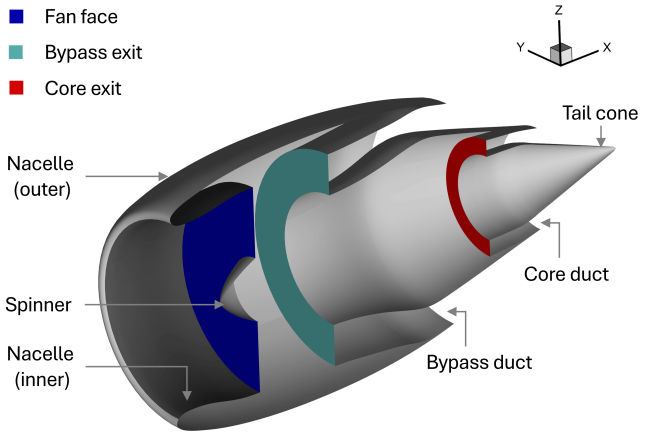

Figure 2.3: Cut-section of the baseline 3D engine design

Symbol	Value
η_{intake}	0.98
$\eta_{fan,poly}$	0.93
$\eta_{hpc,poly}$	0.91
$\eta_{lpc,poly}$	0.91
$\eta_{lpt,poly}$	0.93
$\eta_{lpt,poly}$	0.93
$\eta_{shaft,mech}$	0.99
$\Delta_{p,combustor}$	0.05
$\Delta_{p,ducts}$	0.01

Table 2.2: Engine component efficiencies [39, 42]

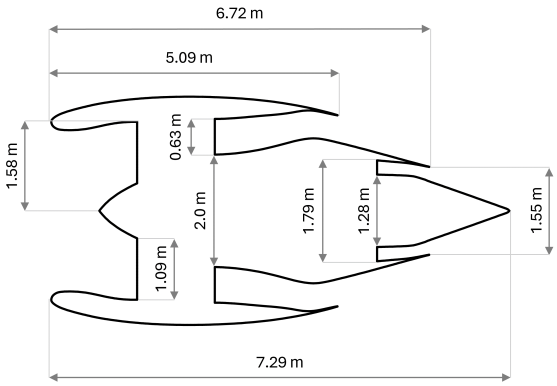

Figure 2.4: Geometric details of the baseline engine design based on GE90-94B [39, 40]

2.1.3. BASELINE INTEGRATED ENGINE-AIRFRAME DESIGN

The integration of the engine with the wing body significantly affects the performance of the combined system. In order to study this interaction, the baseline engine and wing designs described above are integrated into a single design optimization problem. The spanwise engine location for the 2-engine configuration is fixed at $y = 5.071m$ as dictated by the yaw moment conservation due to engine thrust about the center of mass in a 3-engine configuration. The initial chordwise engine location is at $x = 5.0m$ and chosen such that the trailing edge of the engine nacelle is parallel to the wing nacelle at the engine mid-section. Figure 2.5 shows the engine-airframe integrated geometry for the baseline BWB aircraft.

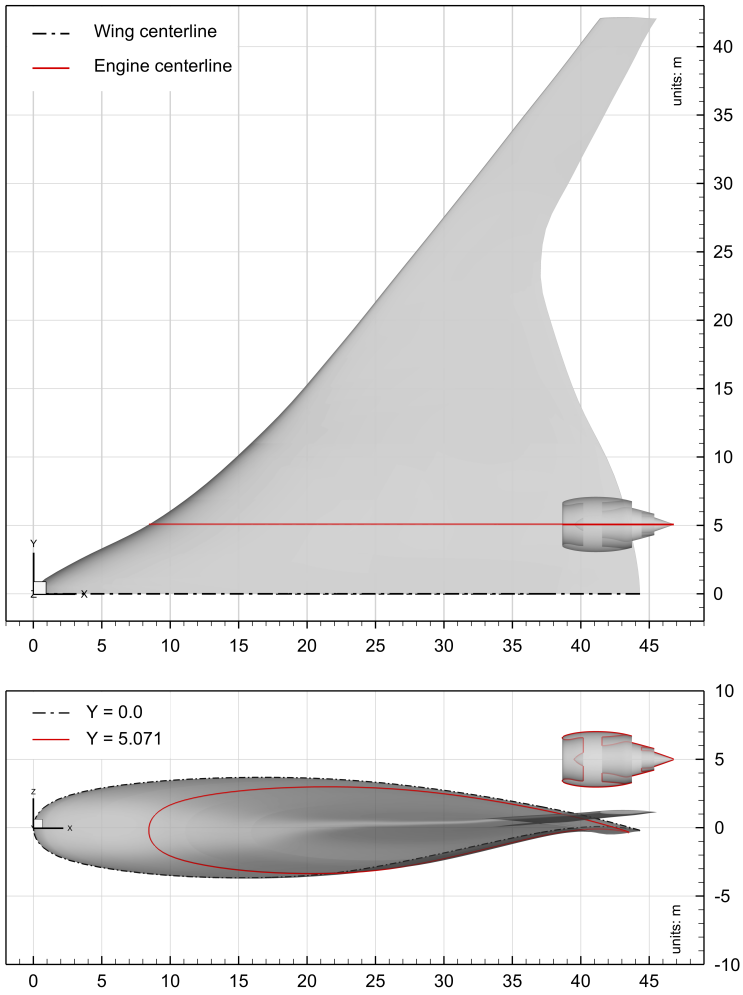

Figure 2.5: Baseline engine-airframe integrated geometry

CHAPTER SUMMARY

This chapter outlined the geometric details and operational characteristics of the Blended Wing Body aircraft used in this study. The baseline BWB wing design is based on the second generation BWB aircraft [4]. The baseline engine geometry and its operating parameters are based on the GE90-94B engine. This engine is mounted on to the BWB in an over the wing configuration. The original second generation BWB had a 3-engine configuration, but in this study a 2-engine configuration is used to reduce the complexity of the problem and to reduce the computational cost associated with additional adjoint evaluations and increased mesh size.

3

METHODOLOGY

This chapter details the methodology used to conduct aeropropulsive optimization studies for both isolated engine and wing cases, as well as for engine-airframe integration. It includes a comprehensive description of the geometric details, analysis methods, parameterization strategy, design constraints, and optimization technique. Additionally, it highlights a novel overlapping Free-Form Deformation (FFD)-based methodology for engine design parameterization and the development of a robust state coupling between the aerodynamic and propulsion disciplines to perform aeropropulsive optimization.

3.1. HIGH-FIDELITY MDO FRAMEWORK: MACH

The MDO framework of aircraft configurations with high fidelity (MACH) is used as the baseline optimization framework for this study. This framework is open-source for its aerodynamic shape optimization capabilities (MACH-Aero). The work performed in this thesis extends this MACH aero framework to integrate pyCycle as a propulsion discipline and perform coupled aeropropulsive optimizations.

3.1.1. AEROPROPULSIVE OPTIMIZATION ARCHITECTURE

The optimization architecture presented in the XDSM[43] in Figure 2.0 shows the Individual Discipline Feasible (IDF) architecture used for the coupled aeropropulsive optimizations in this study. The aerodynamic and propulsion solvers are connected in a feed forward coupling and then made feasible through consistency constraints. This architecture is used for the coupled aeropropulsive optimization studies of isolated engine and engine-integrated wing. The adjoint solver within ADflow is not highlighted explicity. Coupled gradient calculations are needed to solve for the sensitivities of the propulsion output with respect to the inputs to the CFD solver. For this purpose total derivative calculations are implemented in the framework. For single-discipline aerodynamic optimizations of the isolated wing, the propulsion discipline is removed along with the functions for calculating consistency constraints and coupled derivatives. The individual components of this XDSM constitute the methodology explained in this chapter.

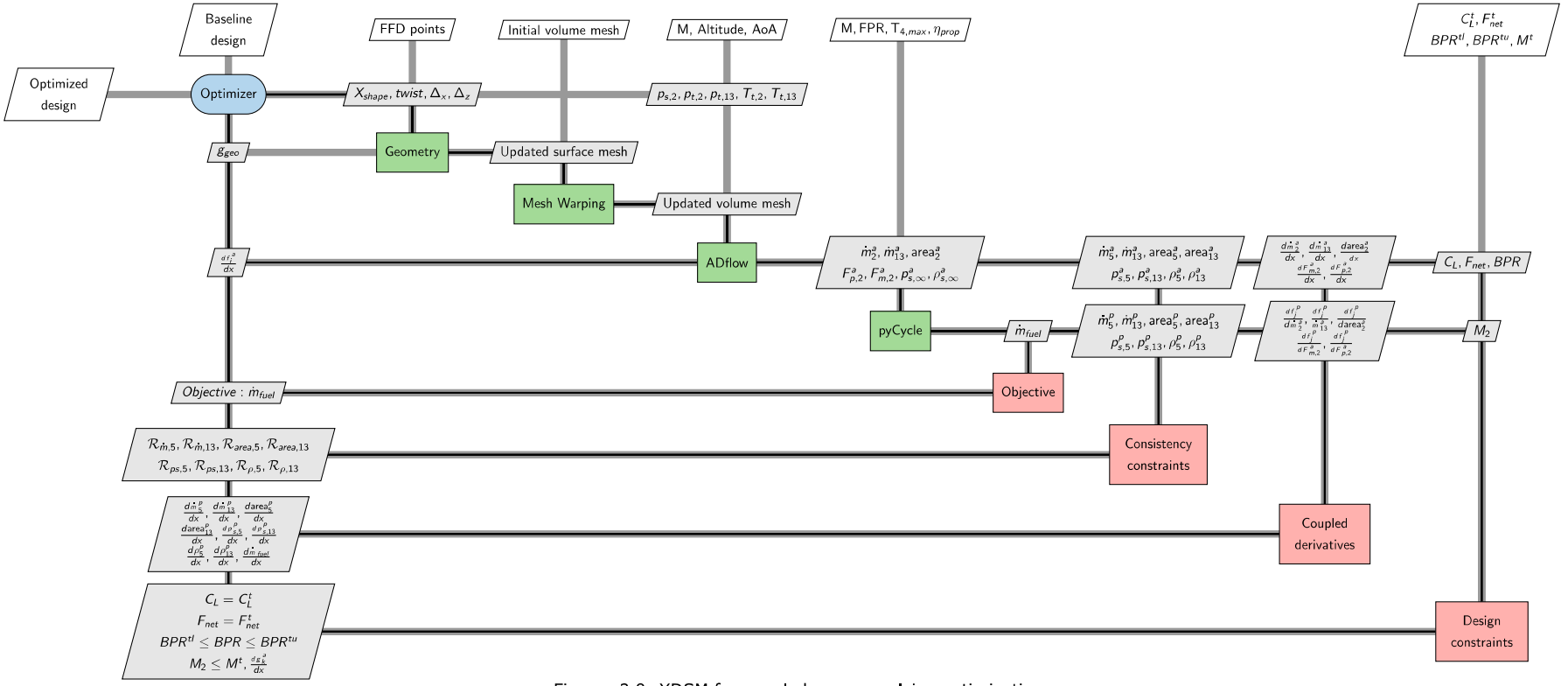

Figure: 3.0: XDSM for coupled aeropropulsive optimization

3.2. ANALYSIS MODELS

The aeropropulsive optimization involves aerodynamics and propulsion disciplines, with disciplinary solvers for each. The aerodynamics discipline uses a high-fidelity RANS solver, ADFlow, for solving the fluid flow equations. The propulsion discipline is represented using a low-fidelity 1D thermodynamic cycle modelling library, pyCycle. Both these disciplinary models are connected with a feed-forward coupling approach, going from the aerodynamics solver to the propulsion solver.

3.2.1. AERODYNAMIC MODEL: ADFLOW

The open-source Reynolds-averaged Navier–Stokes (RANS) based CFD solver, ADflow, is used for the aerodynamic analysis. ADFlow (Automatic Differentiation Flow Solver) is a massively parallel, compressible flow solver for multi-block and overset meshes [31]. The ADflow solver has been extensively validated for benchmark cases [44] and hence, a CFD validation study is not presented in this report. It has Spalart-Allmaras (SA), $k-\omega$, Shear-stress transport (SST) and v2-f turbulence models. However, only the SA model is fully-differentiated and provides gradients for adjoint calculations. For this reason, all CFD analysis presented in this report are carried out with the SA turbulence model in ADflow.

The SA model is a one equation semi-empirical turbulence model. A first-order Approximate Newton-Krylov (ANK) solver is used to converge the solution up to a residual tolerance of 10^{-3}, followed by a second-order ANK solver up to 10^{-8} and the solution is finally converged to a residual tolerance of 10^{-11} using the Newton-Krylov (NK) solver. Hence, a total residual tolerance of 10^{-11} is used for the flow solver, which helps achieve a function precision of less than 10^{-8} for the functional values. A similar 10^{-11} tolerance is used for adjoint convergence.

DRAG AND THRUST ACCOUNTING

Thrust accounting is crucial for estimating the net thrust generated by the engine. In the current work, the engine net thrust is estimated by integrating the pressure, viscous and momentum forces over all the boundaries of the engine, including the fan face, core and bypass boundaries. This calculation is done directly from the forces calculated in the CFD solver and hence provides an accurate estimate of the thrust produced by the engine. This scheme is used for estimating the engine net thrust for both cases involving isolated engine as well as engine-airframe integration. The wing drag is calculated directly by integrating the forces in the CFD solver.

BOUNDARY CONDITIONS

A boundary condition (BC) based approach, presented by Yildirim *et al.* [12] and discussed in (Introduction: Modelling approaches for engine CFD analysis) section 1.1 is used to model the engine fan boundary. The approach presented by Yildirim *et al.* utilized a single inflow-outflow BC pair to represent the engine fan compression stage and the bypass flow, without taking into account the core flow. The current model includes dual outflow boundary conditions to represent

both the bypass and the core flow. Figure 3.1 shows the CFD domain and the boundary conditions used for different boundary surfaces. The fan face is modelled with a subsonic outlet BC while the core and bypass boundaries are represented by subsonic inflow BCs. All wall surfaces, including the engine walls and wing, are modelled with a no-slip wall BC. The farfield inflow and outflow is represented by a farfield BC.

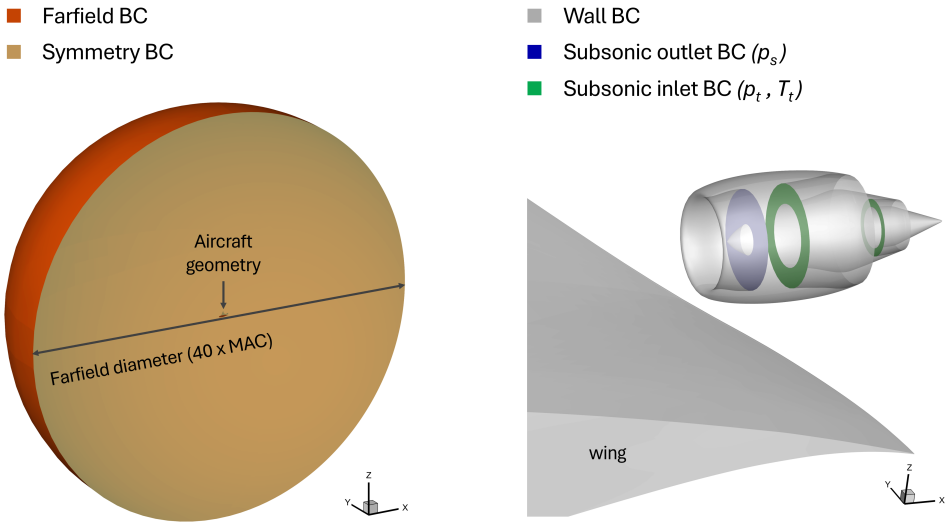

Figure 3.1: CFD domain and boundary conditions for both the wing and the engine

The subsonic inlet/outlet BCs need additional state variable definitions to be specified. The subsonic outlet BC at the fan face needs only the static pressure to be specified to fully define the boundary condition in addition to the outflow velocity unit vector. This fan face static pressure can be specified as a design variable and varied during the optimization to vary fan thrust, mach number and mass flow rate through the fan face in the propulsion model. The subsonic inlet BCs, used for the core and bypass exits (inlets in the CFD domain), require additional state information in order to be fully defined. In ADflow, the subsonic inlet BC requires total pressure and total temperature to be specified along with the inflow velocity unit vector. Similar to the subsonic outlet static pressure, the total pressure and total temperature at the inlet BCs can also be defined as design variables to match the core and bypass state variables and flow rate in the propulsion model. [1]

[1] The boundary condition design variables (BCDVs) for using multiple inlet/outlet BCs are fixed in the following pull request: https://github.com/mdolab/adflow/pull/323

3.2.2. PROPULSION MODEL: PYCYCLE

The propulsion analysis is carried out by using pyCycle [10], a 1D thermodynamic calculation library. A high-bypass turbofan model is setup in pyCycle to calculate the thermodynamic performance of the turbofan engine based on the high bypass turbofan example cycle[2]. This model calculates all thermodynamic states from the engine's fan face to the core and bypass exits of the propulsion model. The component efficiencies and engine specifications used in the pyCycle model are taken for the GE90-94B engine from the data available in the literature [39, 45] and were presented in Table 2.2. The Fan Pressure Ratio (FPR), maximum Turbine Inlet Temperature (TIT) and the polytropic efficiencies are kept constant for the turbofan model in all optimization cases.

The pyCycle model is a connection of thermodynamic component models for compressors, combustor, turbines, shafts and ducts. These component models are governed by simple thermodynamic relations for mass and energy conservation based on their defined efficiency factors. The compressor and turbine components have pre-defined efficiency maps in the pyCycle library which were used without modification. Figure 3.2 shows the interior components of the turbofan pyCycle model and its coupling with the CFD solver. The model is set-up to calculate the design-point performance of the engine at cruise conditions. At the design point, it calculates the engine's fuel consumption, along with the thermodynamic states and geometric areas of the fan face, bypass exit and the core exit. Since, pyCycle is an OpenMDAO component, it has the functionality to provide total derivatives based on the in-built component analytical derivatives. The partial derivatives for the input and output components which are connect to the CFD solver are defined manually.

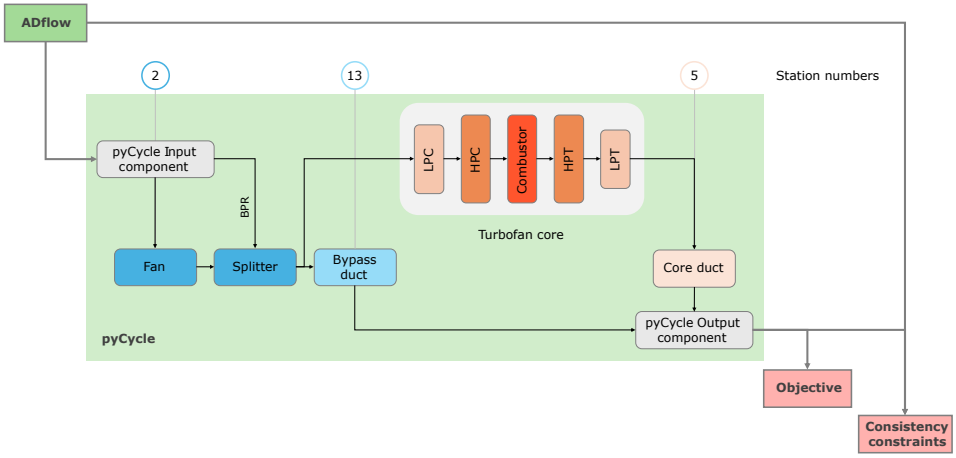

Figure 3.2: pyCycle turbofan model and its connections with other XDSM components

[2] https://github.com/OpenMDAO/pyCycle/tree/master/example_cycles

PROPULSION MODEL VERIFICATION

In the absence of the availability of actual engine data in the literature, the propulsion model is verified with other studies in the open literature. Table 3.1 shows the verification of the PyCyle model with the GE90 performance data provided in another study [39]. A difference in the results of these studies is expected due to the lack of availability of actual engine data and a lack of proper bleed estimates. However, the overall performance and design parameters match reasonably well with the values found in the literature.

Table 3.1: pyCycle engine model verification

Symbol	Value						
		Design Point (Cruise)			Off Design (Take off)		
Quantity	Units	Literature [39]	pyCycle	Δ (%)	Literature [39]	pyCycle	Δ (%)
Altitude	km	10688	10688	-	0	0	-
Mach number	-	0.85	0.85	-	0	0.001	-
TIT	K	1380	1380	-	1592	1600	0.5
FPR	-	1.65	1.65	-	1.58	1.587	0.44
LPC PR	-	1.14	1.14	-	1.1	1.018	7.45
HPC PR	-	21.5	21.5	-	23	23.063	0.27
BPR	-	8.1	8.1	-	8.4	8.372	0.33
Thrust	kN	69.2	69.2	-	375.3	367.1	2.18
$\dot{m_{air}}$	kg/s	576	582.87	1.19	1350	1334	1.19
$\dot{m_{fuel}}$	kg/s	1.079	1.018	5.65	2.968	2.864	3.5
Area bypass exit	m^2	3.5935	3.5205	2.03	3.5935	3.5205	2.03
Area core exit	m^2	1.0111	0.9493	6.11	1.0111	0.9493	6.11
Diameter fan face	m	3.1242	3.1721	1.53	3.1242	3.1721	1.53

3.2.3. AEROPROPULSIVE COUPLING

The aerodynamic and propulsion models are connected in a feed-forward coupling from the CFD model to the pyCycle model. This constitutes an individual discipline feasible (IDF) architecture with consistency constraints to maintain feasibility between the two disciplines. In an IDF architecture, the two disciplines are not consistent with each other unless the consistency constraints become feasible. Hence, it could be desirable to use a multi-disciplinary feasible (MDF) architecture where the disciplines are consistent throughout the optimization. The MDF architecture gets rid of the consistency constraints, but it however, requires additional Newton solves and calculation of coupled sensitivities of the CFD model inputs with respect to the propulsion model output. Therefore, an IDF architecture is selected for this work due to its simplicity and easier implementation.

All the turbofan components are connected in a single pyCycle model which receives inputs for the state variables at the fan face from the ADflow solver.

The thermodynamic calculations for the core and bypass are performed within the pyCycle model and the outputs are forwarded to the define the consistency constraints and the objective. Meanwhile, the states of bypass and core inlets in the CFD solver are modified at each function evaluation to satisfy these consistency constraints as explained above in the subsection 3.2.2. In this way the flow between the fan exit and core inlet is not modelled in the CFD solver, but is instead solved within the 1D pyCycle model.

Since the MACH-Aero solver does not have the capability to calculate total derivatives for aeropropulsive MDO, these total derivative calculations are implemented in the MACH-Aero framework. These total derivatives are calculated using Equation 3.1 for all pyCycle outputs.

$$\frac{dF_j^p}{dx} = \sum_i \frac{dF_j^p}{dF_i^a} \frac{dF_i^a}{dx} \tag{3.1}$$

Here, dF_j^p are the pyCycle outputs and dF_i^a are the inputs to pyCycle from the ADflow solver. The sensitivities of ADflow outputs to its inputs (dF_i^a/dx) are available from the adjoint calculations within ADflow. pyCycle, being an openMDAO component, is also able to calculate the sensitivities of its outputs with respect to its inputs (dF_j^p/dF_i^a). These sensitivities are then coupled to form total derivatives to calculate the sensitivities of the pyCycle outputs with respect to the CFD inputs (dF_j^p/dx). These are calculated for all the 7 pyCycle outputs as shown in for one of the outputs (ρ_5^p) in Equation 3.2. These are then passed to the gradient based optimizer.

$$\frac{d\rho_5^p}{dx} = \frac{d\rho_5^p}{d\dot{m}_2^a}\frac{d\dot{m}_2^a}{dx} + \frac{d\rho_5^p}{\dot{m}_{13}^a}\frac{\dot{m}_{13}^a}{dx} + \frac{d\rho_5^p}{d\text{area}_2^a}\frac{d\text{area}_2^a}{dx} + \frac{d\rho_5^p}{dF_{m,2}^a}\frac{dF_{m,2}^a}{dx} + \frac{d\rho_5^p}{dF_{p,2}^a}\frac{dF_{p,2}^a}{dx} \tag{3.2}$$

BOUNDARY STATE ESTIMATION

In order to couple the 3D CFD and the 1D pyCycle model, it is necessary to convert the 3D state data on the inlet/outlet faces (fan face, core exit and the bypass exit) in the CFD model to a singular state value with minimal loss of information. It is essential for this transformed singular value of the state variable to be as close as possible to the actual state values on the boundary face to maintain consistency between the 3D CFD and 1D propulsion model.

One way to do this transformation is to take area or mass weighted averages at these boundaries as proposed by Lamkin et al. [16]. However, it was found that the optimizer can take advantage of the area/mass averaged values by deforming the walls adjacent to the inlet/outlet boundary and causing flow separation. In such a case, even though the actual range of the state variable could exhibit a large difference on the boundary face, its averaged value could stay close to an attached flow case. One such case is shown in Figure 4.15a where the flow separates ahead

of the fan face causing a large difference in the static pressure on the boundary face. The optimizer takes advantage of this large differential in static pressure due to separation to reduce the mass flow through the fan face while maintaining the average static pressure. This difference in the actual state value at the boundary versus the area or mass averaged state value leaves room for an error-prone coupling between the aerodynamic and propulsion disciplines.

In such a case, the actual scalar value of the state variable as supplied by the optimizer could differ significantly from the actual applied value by the optimizer, as known to the optimizer, could exist in a large range on the interface plane in the CFD domain. This leads to an incorrect estimation of the averaged value of the variable. One such case is when the flow separates ahead of the fan face causing a large difference in the static pressure on the boundary face. The optimizer takes advantage of this large differential in static pressure due to separation to reduce the mass flow through the fan face while keeping a high value of the static pressure. This difference in the actual state value at the boundary versus the area or mass averaged state value leaves room for an error-prone coupling between the aerodynamic and propulsion disciplines.

In order to overcome this issue, a force-based averaging method is introduced in this study. This is done by calculating the state variables, like pressure and density, from the pressure and momentum forces acting on the boundary face. Gray et al. [28] also showed that a force-conserving averaging scheme should be chosen to perform this averaging on the interface planes. They however, used a turbo-electric propulsor which could be modelled using a single actuator zone for the fan leading to a single-stream exhaust. The present work models a high bypass turbofan engine with dual-stream nozzles and thus requires an extended set of state values to enforce this force-conserving averaging scheme on the interface planes.

The net force normal to the interface plane is the sum of the pressure and momentum forces acting on it.

$$F_S = F_p \; + \; F_m \tag{3.3}$$

These pressure and momentum forces can be expressed in the integral form as

$$F_p = \iint_S (p_s - p_\infty) \; \mathrm{d}S \tag{3.4}$$

$$F_m = \iint_S \rho(\boldsymbol{V} \cdot \hat{\boldsymbol{n}})(\boldsymbol{V} - \boldsymbol{V}_\infty) \cdot \hat{\boldsymbol{n}} \; \mathrm{d}S \tag{3.5}$$

where $\hat{\boldsymbol{n}}$ is the unit vector in the direction normal to the face. Assuming uniform scalar values across plane, the pressure and momentum forces can be simplified to

$$F_p = (\bar{p}_s - p_\infty) A \tag{3.6}$$

$$F_m = \dot{m}(\overline{\boldsymbol{V}} - \boldsymbol{V}_\infty) \cdot \hat{\boldsymbol{n}} \tag{3.7}$$

The total mass flow rate and area over the interface plane are given by

$$\dot{m} = \iint_S \rho \boldsymbol{V} \cdot \hat{\boldsymbol{n}} \, \mathrm{d}S, \qquad A = \iint_S \mathrm{d}S \tag{3.8}$$

Equating Equation 3.4 to Equation 3.6 and Equation 3.5 to Equation 3.7, canceling out the constant p_∞ and V_∞ terms, the force-averaged scalar pressure turns out to be an area averaged quantity and the force-averaged velocity as a mass averaged quantity.

$$\bar{p}_s = \frac{1}{A} \iint_S p_s \, \mathrm{d}S; \qquad \bar{V} = \frac{1}{\dot{m}} \iint_S \rho (\boldsymbol{V} \cdot \hat{\boldsymbol{n}})^2 \, \mathrm{d}S \tag{3.9}$$

Rearranging Equation 3.6, the static pressure can be calculated directly from the pressure force on the surface. The value of p_∞ remains constant for a given atmospheric condition. In case of an outlet BC, the sign ahead of the p_∞ term would change.

$$\bar{p}_s = \frac{F_p}{A} - p_\infty \tag{3.10}$$

Similarly, the force-averaged velocity can be represented in terms of the momentum force on the surface. The term $\boldsymbol{V}_\infty$ is a constant and turns out to be equal to 0. So, if the face normal is aligned with the x-direction, then the averaged velocity in the x-direction can be given by

$$\overline{V_x} = \frac{F_{m,x}}{\dot{m}} \tag{3.11}$$

Instead of using the averaged velocity, which is a direction dependent quantity, averaged density at the fan face can be used to represent another intensive state variable. This averaged density can be directly calculated from the momentum force as

$$\overline{\rho} = \frac{\dot{m}^2}{F_{m,x} \, A} \tag{3.12}$$

Using a force-based averaging maintains consistency between the net force generated at the boundary face and the propulsion model input. This method of averaging the state variables avoids the optimizer taking advantage of flow separation. When the flow separates, the pressure and momentum forces on the boundary face drop and the force-averaged value drops accordingly. Hence, a force-based averaging scheme is used for transferring the state variables from the 3D CFD boundary faces to the 1D propulsion model for thermodynamic cycle calculations and constraining the propulsion output state variables to maintain consistency between the CFD and the propulsion model.

3.3. MESH GENERATION

ADflow supports multi-block and overset meshes for CFD calculation. Although overset meshes are relatively easier to construct for complicated geometries, they are prone to mesh failures for large changes in design. Also, overset meshes introduce interpolation errors at the boundaries of the intersecting meshes . On the other hand, multi-block structured meshes are difficult to construct for complicated geometries, but can provide better accuracy, faster convergence and large mesh deformations . For this reason, all cases in this work use multi-block structured meshes, even for the engine-airframe integration case.

The meshing approach used in this project is three-fold. First, a nearfield structured mesh is generated using the Pointwise mesh generation software and then the farfield is generated by extruding the nearfield mesh using PyHyp [46]. The nearfield and farfield meshes are then stitched together to form the entire fluid domain. The finest meshes (L1) are generated using this approach and are then coarsened thrice uniformly in all direction using the cgnsutilities library [3]. The cgnsutilities halves the number of cells in each direction. Hence, the number of nodes in each block edge should follow the rule of $N = 2^n m + 1$, where the mesh can be coarsened n-1 times. The near-wall spacing and growth rate are used such that even the coarse L3 mesh has a Y+ of less than 1.

3.3.1. WING MESH

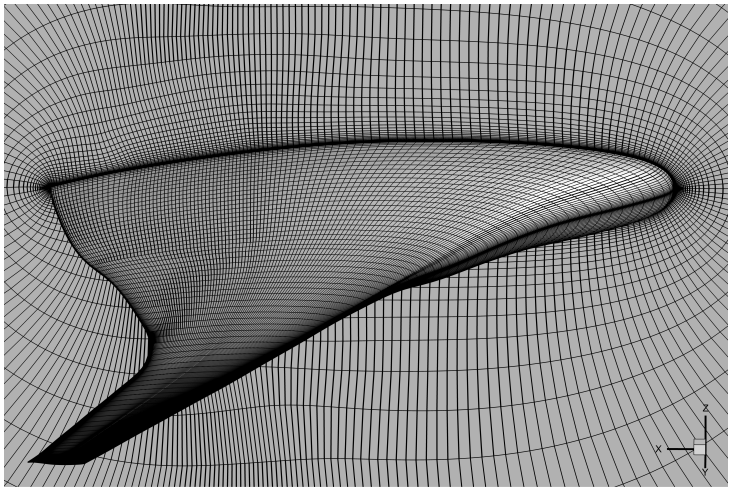

Figure 3.3: Surface mesh on the wing (L1) and the symmetry plane

The wing surface mesh consists of 83136 cells for the finest mesh (L0) with 177 layers present in the wall-normal direction up to a distance of 20 mean aerodynamic

[3] https://github.com/mdolab/cgnsutilities

chord (MAC) length. This results in a growth rate of approximately 1.1 for the L1 mesh with a first layer height of $5x10^{-6}$ m. This first cell height was found to be sufficient for the coarsest (L2) mesh to have a Y+ of less than 1. Figure 3.3 shows the wing surface mesh and and mesh at the symmetry plane for the isolated wing case.

3.3.2. ENGINE MESH

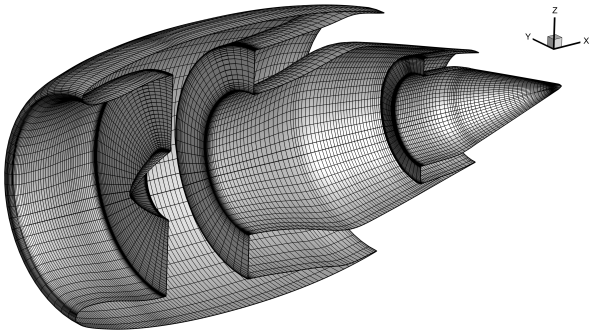

Figure 3.4: Surface mesh (L1) of the baseline engine

The volume mesh for the engine nearfield is created using an O-H topology at the spinner and tail cone tip. Since the baseline engine design is axisymmetric, a 2D mesh was constructed and the 2D mesh slice was then rotate using 128 cells in the azimuthal direction to form the complete 360° engine mesh. A first cell height of $5x10^{-6}$m was found to be sufficient to achieve a Y+ value of less than 1. The nearfield mesh is then extruded using cgnsutilities and combined with the farfield mesh which extends to 20 engine lengths for the isolated engine case. The finest L0 mesh thus constructed for the engine consisted of approximately 6.5 million cells. Figure 3.4 and Figure 3.5 show the surface mesh for the engine and a cut section of the volume mesh for the isolated engine case.

3.3.3. INTEGRATED ENGINE-AIRFRAME MESH

To construct a multi-block mesh for the combined engine-airframe case, we use the extruded nearfield meshes for the wing and the engine and join them together to form the combined nearfield using manually constructed blocks. This outer layer of this combined nearfield is then extruded into the farfield and joined with the nearfield mesh. The surface mesh for the wing and engine in this combined case is the same as that for isolated engine and wing cases. However, additional cells need to be introduced to combine the engine and wing nearfield volume meshes while maintaining the structured nature of the mesh. These combined nearfields are then extruded in the farfield resulting in a total mesh count of 63.5 million cells for the finest level L0 and about 1 million for the L2 mesh. Figure 3.7 shows a magnified region where the engine and wing meshes are connected together for three different mesh levels.

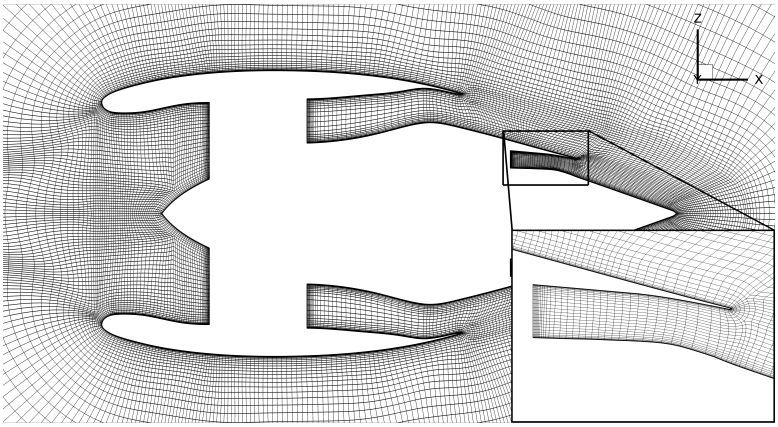

Figure 3.5: Cut-section of the engine (L1) mesh at the centerline

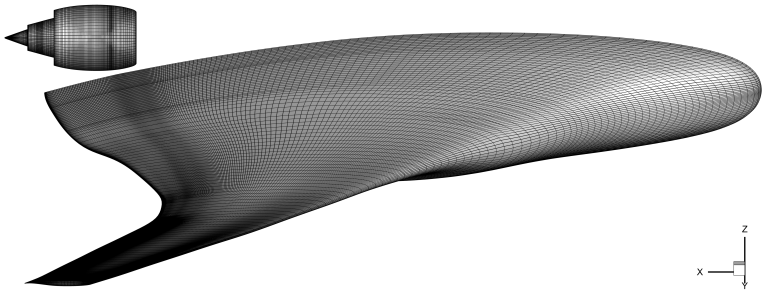

Figure 3.6: Surface mesh (L1) for the engine-airframe integration case

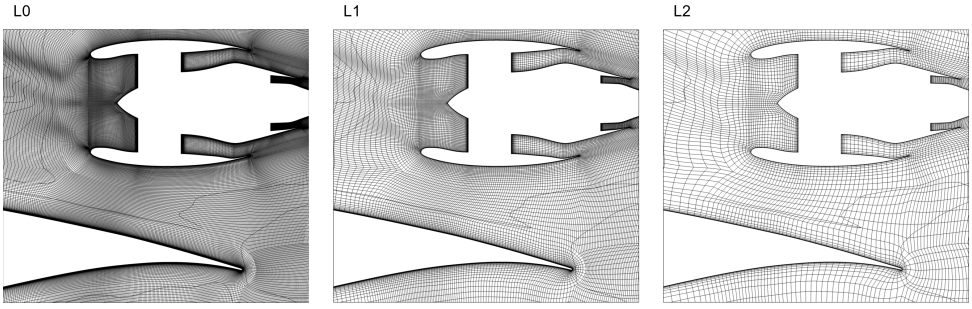

Figure 3.7: Cut-section of the engine-airframe mesh at the engine centerline for three mesh levels: L0, L1 and L2

3.3.4. GRID REFINEMENT STUDY

In order to quantify the error in solution due to mesh size, a grid refinement study was performed. For this purpose, a very fine grid (L0) is first created which is then successively coarsened using the cgnsutilities[4] tool by a factor of 2 in each direction. Hence, the coarse meshes have 1/8th mesh count of the immediate finer level. A Richardson extrapolation scheme is used to quantify the value where the solution would converge with a grid spacing on the order of zero.

The Richardon extrapolation point is calculated as defined in the MACH-Aero documentation[5]. Using cgnsutlities coarsens the mesh using a grid refinement factor (r) of 2. The actual rate of convergence of the solver (p') with successive mesh refinement can be calculated as:

$$p' = \ln\left(\frac{f_{(L2)} - f_{(L1)}}{f_{(L1)} - f_{(L0)}}\right) / \ln(r) \tag{3.13}$$

Based on this rate of convergence of the solution, the Richardson extrapolation value is given by:

$$f_{h\to 0} = f_{(L0)} + \frac{f_{(L0)} - f_{(L1)}}{r^{p'} - 1} \tag{3.14}$$

Figure 3.8 and Figure 3.9 show the results of this refinement study for the wing and engine meshes. In case of the wing mesh, the L2 mesh has an error of 7.38% compared to the L1 and the engine mesh has 1.21% error in $\dot{m}_{fuel}$ relative to its L1 mesh. The engine L1 mesh has a run time of 364s for a single analysis on 40 cores, whereas the L2 mesh takes just 16.5s. A similar increase in the computation time was observed for the wing mesh. Based on the computational time and resources which would be required for the integrated airframe case, the L2 mesh was selected for optimization in both the engine and wing cases to maintain comparability in the isolated and integrated engine-wing cases. It was later observed that the optimized designs have a similar error to the baseline mesh, hence the trend studies within the same mesh level can be considered valid. Based on this, the same L2 level surface meshes were combined for the integrated engine-wing optimization case.

3.4. PARAMETERIZATION AND MESH DEFORMATION

A free-form deformation (FFD) based parameterization scheme is used to parameterize both the wing and engine geometry using the opensource PyGeo [20] library. The PyGeo library allows for an FFD-based geometry parameterization and constraint formulation along with the geometric derivatives of these operations with respect to the design variables. This parameterization approach works by embedding the reference geometry enclosed within the FFD volume and deforming the embedded surface mesh nodes by manipulating the FFD control points.

[4] https://github.com/mdolab/cgnsutilities
[5] https://mdolab-mach-aero.readthedocs-hosted.com/en/latest/machAeroTutorials/aero_gridRefinementStudy.html

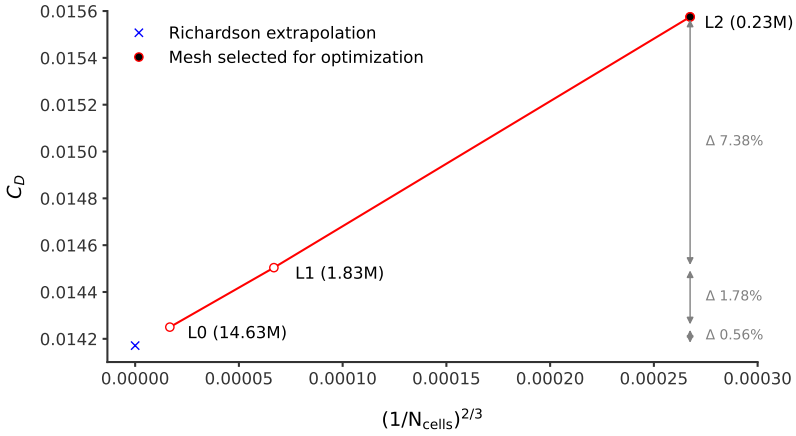

Figure 3.8: Grid refinement study for the isolated wing case

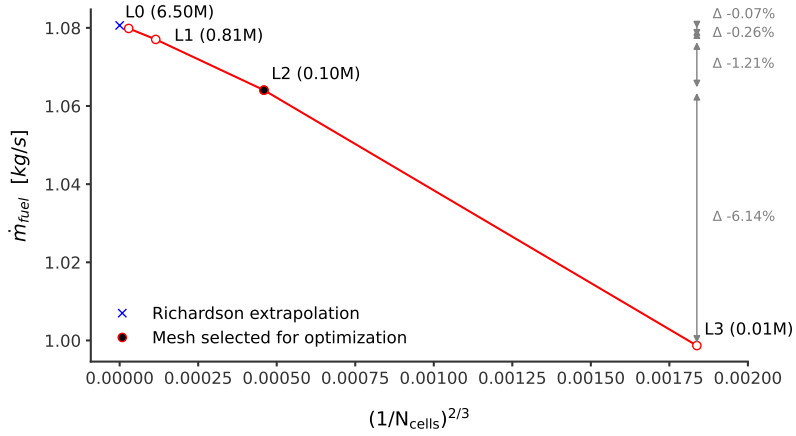

Figure 3.9: Grid refinement study for the isolated engine case

PyGeo supports nesting of the FFD volumes to provide a hierarchical structure for geometry manipulation. This approach allows for using multiple child-FFDs. Since these FFD boxes are B-Spline volumes, multiple FFDs can be superimposed to produce a continuous deformation for multiple intersecting surfaces. chapter 6 contains a verification this approach to achieve continuous geometric deformation. The current work involves a unique implementation of this hierarchical FFD structure along with the ability to superimpose the FFD volumes to construct an engine parameterization to perform complex geometry manipulation. This FFD-based engine parameterization provides a vast design space which is not accessible through the current parameterization techniques used for engine shape optimization.

3.4.1. WING PLANFORM PARAMETERIZATION

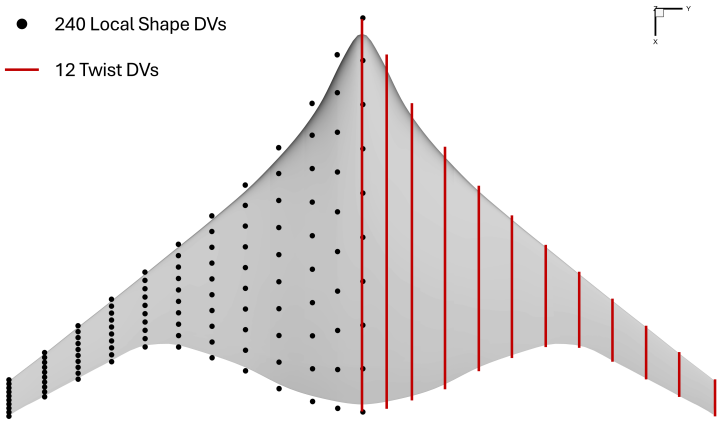

Figure 3.10: Design variables for wing shape modification

Lyu and Martins [36] used an FFD based parameterization method to parameterize the BWB geometry. In the current work, a similar parameterization technique is formulated using a body-fitted FFD for the wing. Figure 3.10 shows the FFD control points on the wing upper surface which are used for the local shape design variables and the FFD sections that are used for sectional twist DVs.

3.4.2. ENGINE PARAMETERIZATION

Most existing engine parameterization techniques make use of simple geometric design variables, which do not allow for complicated engine-nacelle design. This work proposes an overlapping circular FFD-based engine parameterization which can perform complicated local shape deformations. Using this approach, both axisymmetric and non-axisymmetric engine shape deformations can be achieved simultaneously in the same geometry.

CIRCULAR FFDS (K-OVERLAP)

As the basis functions of the FFD volume splines approach a C^0 continuity towards the end section (natural cubic splines), it is not possible to use a single FFD for embedding closed revolved surfaces. Using a single 360° FFD would lead to a C^1 discontinuity in the embedded surface at the location where the FFD sections end. Such a discontinuity in a closed revolved face is undesirable. To overcome this issue, two symmetric overlapping circular FFD volumes are used, with each FFD embedding only one half of the surface under consideration. This is accomplished by using parametric volume bounds for the FFDs by defining how much of the surface is to be embedded within each of the two FFD volumes.

Figure 3.11 shows the implementation of this method using two overlapping circular FFDs for the engine nacelle. These FFDs each consist of 13 sections in the azimuthal direction which overlap half-way with each other. The second FFD is a 180° rotated copy of the first FFD. The overlapping FFD control points of both these FFDs are moved together to have a continuous deformation on the upper and lower parts of the embedded surface to mimic the effect of a continuous circular FFD. Since, this overlap of circular FFDs takes place in the k-orientation of the FFD block, the resulting overlap is referred to as k-overlap in this report.

Such a parameterization allows for selective (non-)axisymmetric design freedom, which is typically required for aircraft engines. This parameterization technique can also be used to model other closed/circular geometries, like rockets, spacecrafts and missiles, where both axisymmetric and non-axisymmetric deformations could be desirable.

FFD SUPERPOSITION (I-OVERLAP)

The engine geometry consists of multiple intersecting surfaces, for example, the nacelle intersects with fan face and bypass exit face. Therefore, a singe continuous FFD cannot be used to parameterize the engine nacelle. A unique way to accomplish this is to use the superposition of FFDs. Since FFDs are basically volumetric B-Splines, multiple FFDs can be overlapped to cause a net geometry change which is a superposition of the effect of moving the overlapping FFD control points. Figure 3.11 shows these FFD overlap strategies for circular overlapping FFD sections.

ENGINE COMPONENT FFDS

Combining the above mentioned i and k-overlapping methods, a unique FFD-based parameterization scheme can be created for complicated 3D rotated geometries, like turbofan engines. Figure 3.12 shows an overlapping child FFD network that is used in the current work and the possible geometric design variables that can be achieved with this parameterization. It consists of overlapping circular child FFDs for different surfaces in the turbofan engine design. This parent-child FFD network consists of a parent FFD enclosing 10 children FFDs. The parent FFD, in itself, undergoes no change, but it is only used to enclose the children FFDs. All children FFDs are allowed to move in radial direction and some in chord-wise direction using shape function design variables to change the shape of different engine components.

All the inner engine FFDs, except the forward and mid-nacelle FFDs, have axisymmetric design variables to maintain axisymmetric deformations in regions where turbomachinary components are located. The design freedom of all FFDs can be easily modified to deform them either axisymmetrically or non-axisymmetrically in both i and k-directions to allow for chord-wise leading/trailing edge elongation as well as radial deformation. Figure 3.13 shows the an example of possible deformation that the engine mesh can go through during an optimization. This parameteriation allows for a significantly higher design freedom than typically parameterization

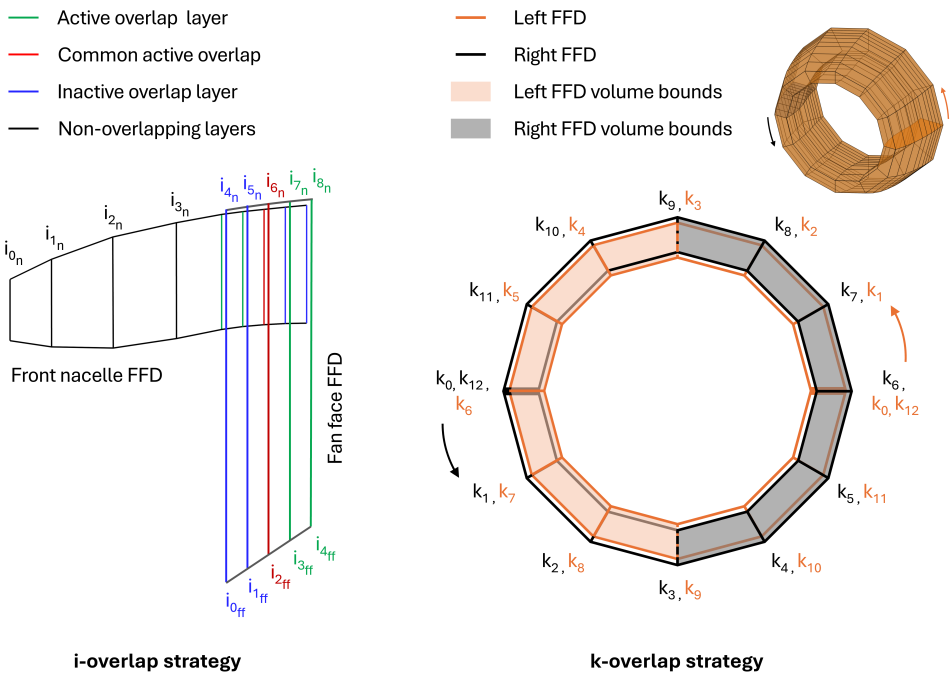

Figure 3.11: Overlapping circular FFDs for engine parameterization

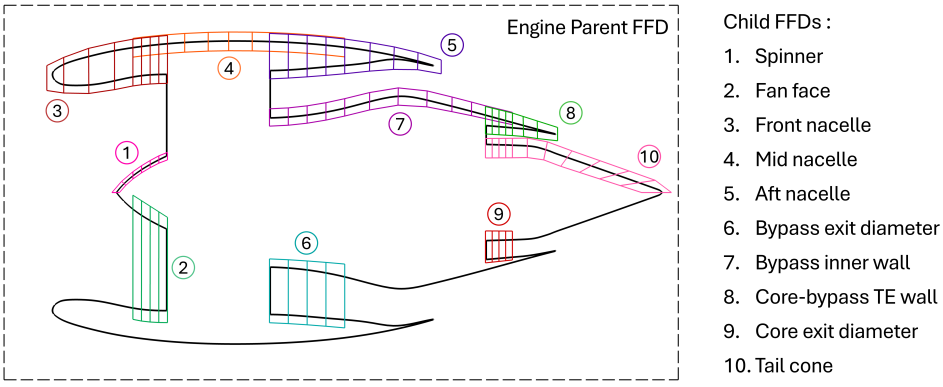

Figure 3.12: Description of overlapping FFDs for engine parameterization

methods in use today. This design freedom can be specially useful in eliminating shocks in the engine-airframe integration cases, where the nacelle geometry can be deformed non-axisymmetrically.

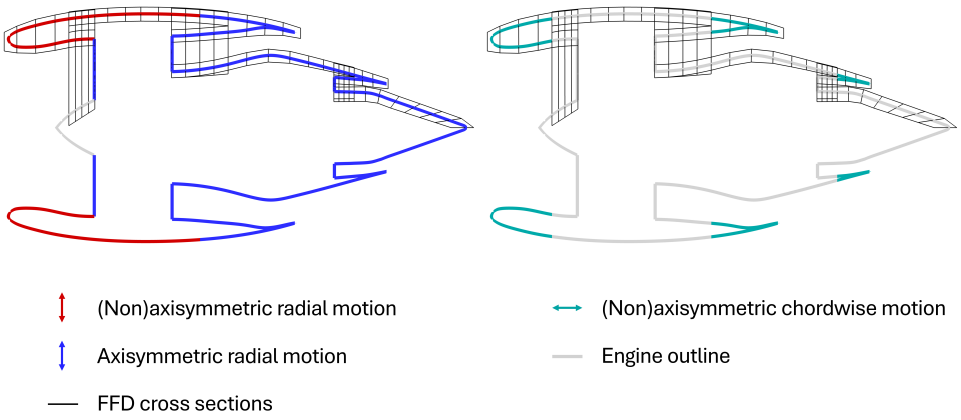

Figure 3.13: Possible deformations for different engine surfaces using shape DVs

3.4.3. INTEGRATED ENGINE-AIRFRAME PARAMTERIZATION

The integrated engine-airframe case utilizes a combination of the existing wing and engine children FFD with a global parent FFD, which envelopes all the children. All FFDs and design variables that are used for the isolated wing and engine cases can be used directly for the engine-airframe integrated case. The only consideration is to ensure that the engine FFDs do not embed any part of the wing surface and vice-versa. The full FFD network used for the combined engine-airframe case is presented in Figure 3.14.

3.4.4. MESH DEFORMATION ALGORITHM: IDWARP

The FFD-based parameterization defined above deforms the underlying geometrical surface. As this surface is deformed, the volume mesh needs to be deformed along with it to prevent the mesh from breaking, while maintaining a sufficient mesh quality for the CFD solver. Since regenerating the mesh at every iteration is very expensive and can introduce noise in the function evaluations, MACH-Aero uses the IDWarp [46] algorithm to perform mesh warping. IDWarp is an inverse-distance mesh warping algorithms based on the method proposed by Luke *et al.* [47]. IDWarp maintains a high orthogonal near the walls and deforms the near field based on the defined inverse-distance warping parameters.

3.5. DESIGN CONSTRAINTS

A combination of geometric and operability constraints are used to constrain the design space. Geometric constraints, like thickness and volume constraints, are used to satisfy the basic structural and volume requirements in the absence of a structural model. These geometric constraints are defined using the DVConstraints

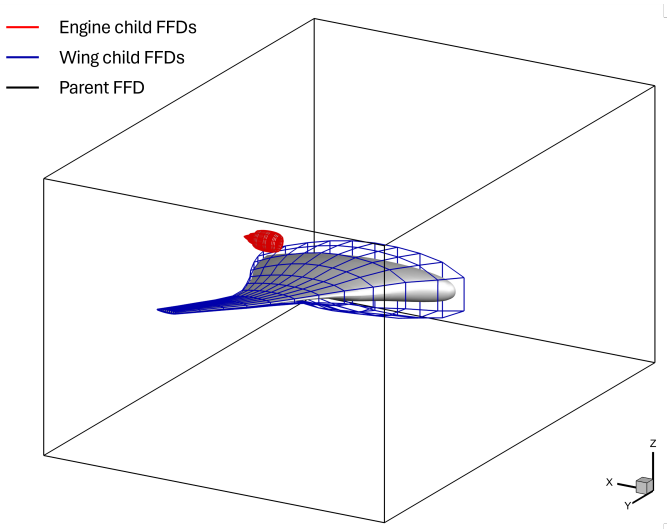

Figure 3.14: Parent-child FFD network for the engine-airframe integration case

class in the PyGeo library. A large number of thickness constraints can be used since these require only a linear solve and are very cheap to calculate. On the other hand, analytical constraints are used to constrain the functional values that define performance requirements like, lift, trim and fan face mach number. Some of these design constraints are also used to specify consistency constraints between the aerodynamics and propulsion models.

3.5.1. WING DESIGN CONSTRAINTS

The wing optimization case has geometric constraints for the wing design which include "toothpick" thickness constraints and a wing volume constraint. These constraints are represented in Figure 3.15. The thickness constraints are a crude alternative of the structural constraints and their value can vary between 0.7 to 1.5 times of the baseline. The volume constraint is defined by the volume of the wing enclosed between 5% and 95% of the local chords across the wing span. It has an upper bound of 1.2, but a lower bound of 0.99 so that the volume capacity of the optimized design remains atleast the same as the baseline. The trailing edge-leading edge constraints (LeTe constraints) force the upper and lower control points of the leading and trailing edge on the FFD to move in opposite directions. This ensures that the FFD deformation does not create a shearing twist in the presence of the local shape and twist DVs.

In addition to these geometric constraints, there are some performance constraints for the wing optimization case. A primary performance constraint is on the lift coefficient, such that the lift generated by the wing is equal to its weight in cruise flight. As per the characteristics of the second generation BWB, a lift coefficient of

0.206 is desired for the aircraft. It is assumed that the aircraft weight does not change substantially during its cruise phase and so, the Cl constraint assumes a constant value. For the longitudinal stability, a trim constraint can be formulated to make the pitching moment about the center of mass of the aircraft to be zero.

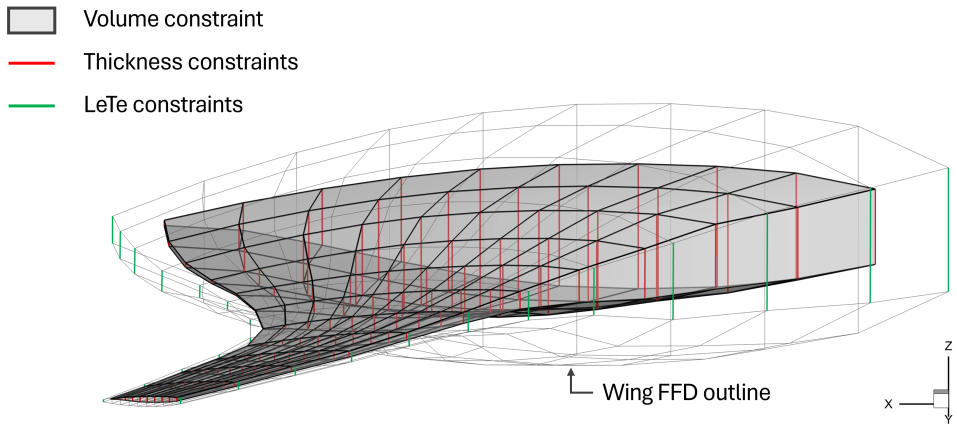

Figure 3.15: Geometric constraints for the wing design

3.5.2. ENGINE DESIGN CONSTRAINTS

The geometric constraints for the engine only consist of the 2D thickness constraints. Depending upon the design freedom in specific optimization case (axisymmetric, non-axisymmetric deformations), the thickness constraints can be applied in multiple planes passing through its central axis. Figure 3.16 shows these thickness constraints for different engine optimization cases. In case of axisymmetric deformations, only planar thickness constraints are needed. When the chord length of the front nacelle is allowed to vary non-axisymmetrically, this necessitates an axial distribution of thickness constraints in the front nacelle. Similarly, when the radial deformations in the front and mid-nacelle are allowed to be non-axisymmetric, the thickness constraints are distributed axially at the location of the circumferential FFD sections.

The engine performance constraints consist only of a BPR constraint. The bypass ratio is determined based on the ratio of mass flow rates through the fan face to the bypass exit. This ratio can be fixed to a single value through an equality constraint, for example, in case of matching the baseline engine BPR. It can also be allowed to vary within a limit using an inequality constraint to allow the optimizer to explore a better design point, especially in case of change in design requirements, like extracting higher thrust. The isolated engine is optimized for a specific thrust requirement, hence the net thrust of the engine is also constrained. This net thrust is the sum of all the forces experienced by the walls of the engine

and the momentum and pressure forces on the boundary surfaces of the fan face, core and bypass. A mach number constraint is also imposed on the fan face to keep the fan inflow Mach number below 0.6 to avoid shocks on the fan blades.

In addition to these performance constraints, the aeropropulsive coupling also requires consistency constraints between the the CFD and propulsion models for matching the state variables on the bypass and core exits as explained in subsection 3.2.3.

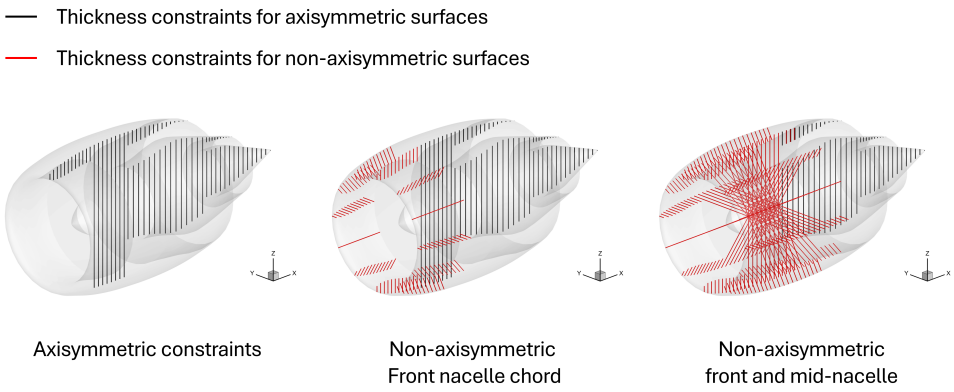

Figure 3.16: Thickness constraints for different engine optimization cases

3.5.3. ENGINE-AIRFRAME DESIGN CONSTRAINTS

In case of engine-airframe integration, the geometric constraints for the wing and engine design are the same as explained for the isolated wing and engine optimization cases. In addition to these existing geometric constraints, there is an additional proximity constraint that is used to prevent the intersecting of wing and engine geometries. This is defined similar to a 2D thickness constraint, but unlike the thickness constraint, it is defined in the fluid region between the wing and the engine outer nacelle. Figure 3.17 shows the proximity constraints applied between the external surface of the engine and wing. An absolute range of the thickness can be kept based on the structural requirements, but in the current study these constraints are primarily used to prevent geometric intersections and are allowed to freely change between 0.5 and 1.5 times their baseline length to identify aerodynamically suited engine locations.

The performance constraints in case of engine-airframe integration change slightly with respect to the isolated wing and engine optimization cases. The lift coefficient constraint now also accounts for the lift or downforce generated on the engine. So, it is changed to calculate the aircraft lift coefficient instead of just the wing's lift coefficient. The engine net thrust constraint is replaced by a net zero drag constraint.

This dictates that the net thrust generated by the engine equals the drag generated by the wing. Hence, the total force generated by the engine-airframe configuration in the direction of the flight should be zero. The engine BPR constraint and consistency constraints are calculated in the same way as explained in subsection 3.5.2.

Figure 3.17: Proximity constraints between the engine nacelle and the rear wing

3.6. OPTIMIZATION ALGORITHM: SNOPT

All optimization studies performed in the thesis use the gradient-based sequential quadratic programming algorithm SNOPT [18] which is suited for large-scale constrained optimization problems. This optimizer is accessed in MACH-Aero using pyOptSparse [48], which is an object oriented framework for parallelly solving optimization problems.

CHAPTER SUMMARY

This chapter explained in detail the methodology employed for performing aeropropulsive optimizations of the engine and wing in both isolated and integrated configurations. First, the extended MACH-Aero framework for aeropropulsive optimization was presented. The CFD and propulsion analysis models were defined and verified. Next, the aeropropulsive coupling methodology was explained to ensure disciplinary consistency and to calculate coupled sensitivities. The modeling approach for the CFD and propulsion analyses was then laid out, followed by details of the proposed parameterization scheme and design constraints.

4

RESULTS

This chapter presents the results of the BWB optimization using the methodology described in the previous section. The results are divided into four sections. The first section details the aerodynamic optimization of the isolated BWB wing. The second section discusses the aeropropulsive optimization of the HBTF engine, verifying the effectiveness of the proposed non-axisymmetric engine parameterization scheme at an angle of attack and examining trends in engine design variation for different thrust requirements. The third section combines the BWB wing and engine to perform aeropropulsive optimizations of the propulsion-integrated airframe, with varying levels of design freedom. Finally, the fourth section compares all these results, identifying the differences in the engine and wing designs optimized in isolated versus integrated conditions. To utilize symmetry, all isolated engine and wing cases use only half the geometry. In the case of integrated engine-wing optimization, the design remains symmetric about the wing mid-plane; thus, a full engine is modeled, along with a half wing with a symmetry boundary at its mid-plane.

4.1. AERODYNAMIC OPTIMIZATION OF ISOLATED BWB WING

The wing optimization case involves a single discipline and hence requires a simple optimization architecture. The objective in this isolated wing optimization case is to minimize the drag coefficient ($C_{D,w}$) of the wing at a given lift coefficient ($C_{L,w}$). $C_{D,w}$ and $C_{L,w}$ are calculated using Equation 4.1 with the freestream values at cruise condition provided in Table 4.1. Reference wing area is half the actual value of the wing planform due to symmetry condition at the wing mid-plane and is equal to 736.5 m^2. Wing drag is calculated within the ADflow solver by integrating the forces on the wing surface which takes into account variations in the inflow angle.

Table 4.2 shows the optimization statement for the isolated wing optimization case. The design variables include twist at 11 of the 12 wing sections as discussed previously in subsection 3.4.1, Figure 3.10. The twist section at the symmetry plane is not used for wing-only optimization. Instead an AoA DV is used which changes the angle of attack of the freestream flow, without twisting the wing root. Additionally, 240 local shape design variables are used to deform the wing surface locally.

Table 4.1: Reference freestream values for cruise condition

Symbol	Description	Value	Units
	Altitude	10668	m
M_∞	Mach number	0.85	[-]
v_∞	velocity	252.123	$[m/s]$
ρ_∞	density	0.38045	$[kg/m^3]$

$$C_{D,w} = \frac{\text{Drag}_w}{0.5\ \rho_\infty\ v_\infty^2\ \text{Area}_w} \quad , \quad C_{L,w} = \frac{\text{Lift}_w}{0.5\ \rho_\infty\ v_\infty^2\ \text{Area}_w} \tag{4.1}$$

As per the lift requirement of the second-generation Boeing BWB, $C_{L,w}$ is constrained at a target lift coefficient of 0.206 to support an MTOW of approximately 823000 pounds (373306 kg) [37]. The corresponding lift coefficient constraint ($C_{L,w_{con}}$) is normalized with the target lift coefficient of 0.206 as shown in Equation 4.2. A trim constraint is not used in the current work and is out of the scope of this study. Geometric constraints are used to preserve the wing volume to a minimum of 99% of the baseline wing capacity and thickness constraints are used to allow local thickness variations between 70-150% of the baseline wing geometry.

$$C_{L,w_{con}} = C_{L,w}\ /\ 0.206 - 1 \tag{4.2}$$

Table 4.2: Optimization statement for aerodynamic optimization of the isolated wing

	Variable	Description	Quantity
minimize	$C_{D,w}$	Wing drag coefficient	
	twist	Sectional twist DVs for the wing	11
	$X_{shape,\ w}$	Shape DVs for wing	120
		Total design variables	131
subject to	$C_{L,w_{con}}$	Wing lift constraint	1
geometric	$0.99 \leq g_{vol,\ w} \leq 1.2$	Wing volume constraint	1
constraints	$0.7 \leq g_{geo,\ w} \leq 1.5$	Wing thickness constraints	144
		Total constraints	146

4.1.1. DRAG MINIMIZATION OF THE ISOLATED WING

Based on the optimization statement defined in Table 4.2, this section presents the results of the wing optimization case for drag minimization. The results presented in this section are carried out using the coarse mesh (L2) comprising of approximately 0.23 million volume cells. The optimization was carries out using a feasibility tolerance of 10^{-6} and an optimiality tolerance of 10^{-6}. Such a tight feasibility tolerance is essential to ensure that the design constraints are sufficiently satisfied. A high optimality tolerance ensures that the objective is minimized to the given value of tolerance. However, it is necessary to determine a suitable value of the optimality tolerance to avoid the extra computational cost of optimization iterations when the objective value does not change beyond a significant limit.

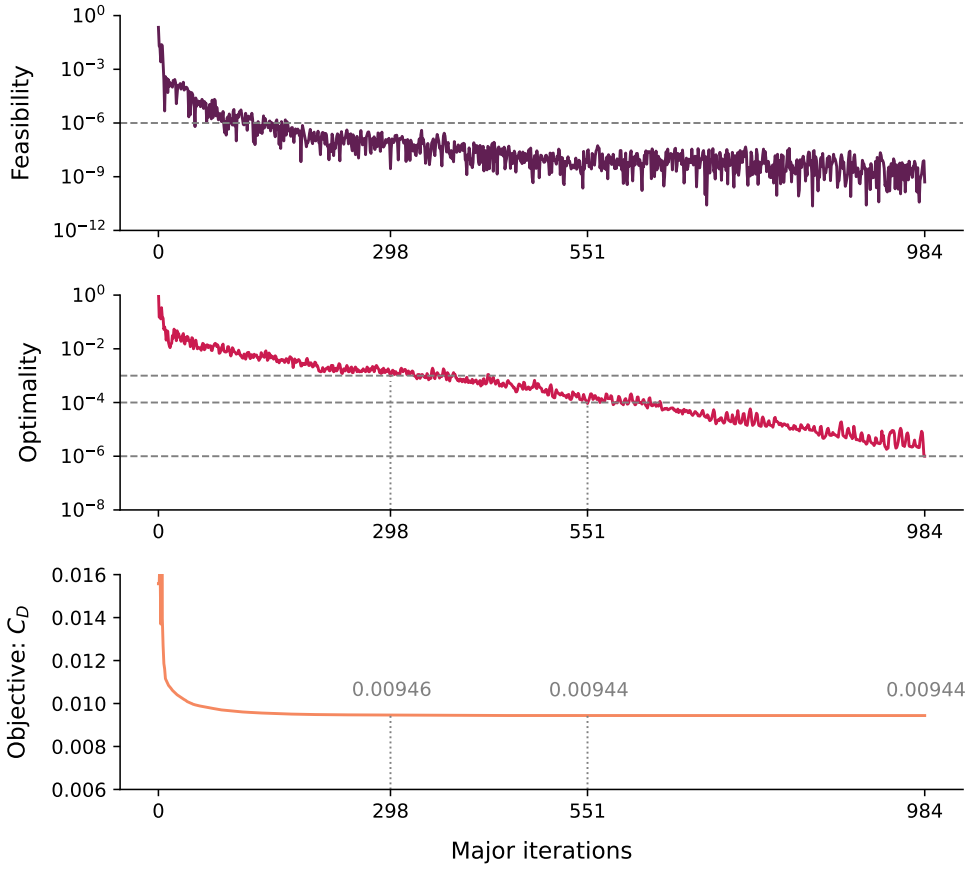

Figure 4.1: Optimization convergence history for the isolated wing case

Figure 4.1 shows the convergence history for this aerodynamic optimization case. It can be observed that the optimizer first tries to rapidly minimize the constraint violation, making it reach the feasibility tolerance in approximately the first 100 major iterations. The optimality value drops at a relatively slower rate. Although an optimality tolerance of 10^{-6} is used for the current optimization, an optimality tolerance of 10^{-4} provides essentially the same optimum for this case. For engineering purposes, an optimality tolerance of 10^{-3} also provides a sufficient reduction in the objective function, with a difference in $C_{D,w}$ within one drag count. It took about 15.4 hours to solve this optimization problem on a single node with 40 cores for the L2 mesh (0.23M cells).

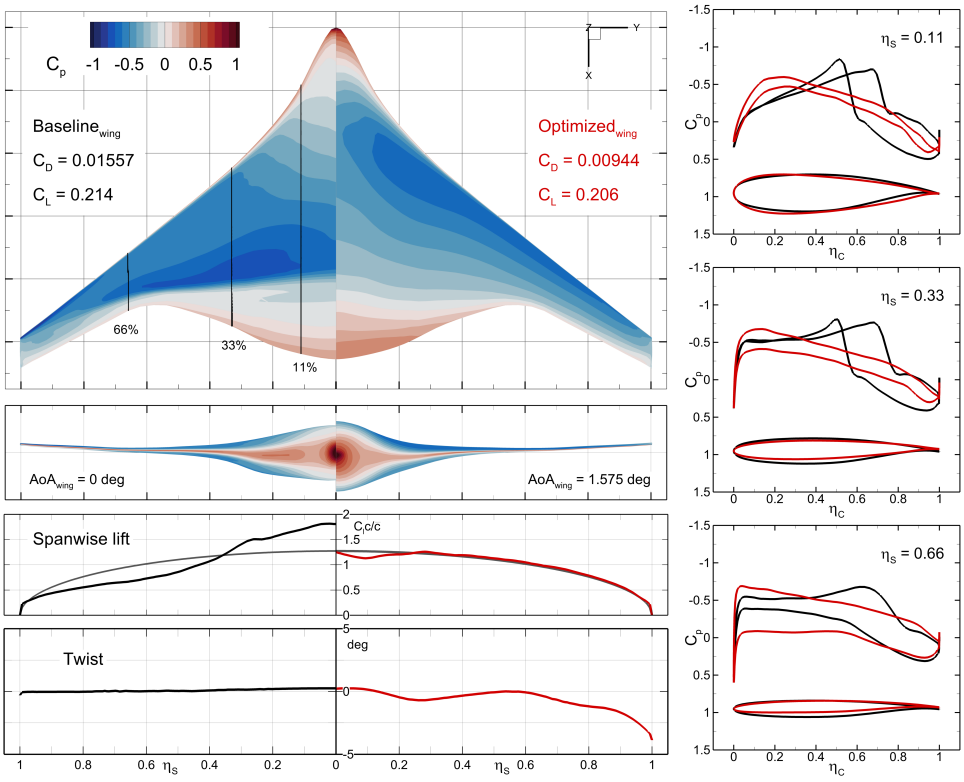

Figure 4.2: Results of aerodynamic optimization of the isolated wing

The results of this wing optimization are presented in Figure 4.2. During the optimization, wing drag reduces by 39% with respect to the baseline unoptimized case from a $C_{D,w}$ of 0.01557 to 0.00944. It should be noted that the baseline wing is analyzed at a 0° AoA and does not satisfy the lift constraint. The optimized wing geometry satisfies the lift constraint at an AoA of 1.575°. Spanwise lift distribution for the optimized wing follows an elliptical distribution, except at the inboard wing.

Outboard airfoils become thinner while the inboard airfoils thicken to satisfy the volume constraint. The loss of lift at the inboard wing is assumed to be due to the volume and thickness constraints restricting the wing to reach a better inboard lift distribution. As opposed to the baseline untwisted wing, the optimized wing geometry has a negative twist distribution.

$$C_p = \frac{p - p_\infty}{0.5\ \rho_\infty\ v_\infty^2} \tag{4.3}$$

Pressure coefficient is calculated with respect to the freestream pressure as shown in Equation 4.3. The contours of pressure coefficient are centered about 0 to show the areas under positive and negative pressure with respect to the freestream in order to identify areas producing positive and negative lift. Near the wing leading edge, the optimized wing has pressure contours running nearly parallel to it. The negative pressure zone near the leading edge is due to the suction peaks at the airfoil sections. On the right side of Figure 4.2, C_p distribution on different airfoil sections shows these suction peaks. The inboard airfoil cross section at 11% of the semi-span shows that the optimized airfoil has eliminated the shocks on both the suction and pressure sides. The outboard airfoil at 66% semi-span has a lower thickness, a relatively flat suction surface and a cambered trailing edge, which is typical of transonic airfoils.

A supplementary wing optimization was carried out with the same optimization statement using the medium wing mesh (L1) starting from the optimized coarse wing design variables and converged till an optimality tolerance of 10^-4 to quantify the change in optimization results due to mesh size. The change in $C_{D,w}$ between the optimized and baseline wing of the medium mesh (L1) is 61.8 drag counts (42.6%) while that in the coarse mesh (L2) was 61.3 drag counts (39.4%). Thus, the change in objective obtained from both the coarse and medium meshes with respect to their respective baselines is almost the same. This trend can be used to make comparative studies with coarse meshes, while using the fine mesh results for refined designs. This trend is further verified for the engine optimization studies in the next section. Table 4.3 summarizes the performance characteristics of the optimized wing designs for both mesh sizes in comparison to their respective baselines.

Table 4.3: Performance characteristics of the optimized wing

Case name	$C_{D,w}$		$C_{L,w}$	AoA$_w$(°)	Mesh size
	value	$\Delta_{\text{drag counts}}$			
Baseline_L2	0.01557	-	0.214	0	L2
W1_L2	0.00944	61.3	0.206	1.575	L2
Baseline_L1	0.01450	-	0.213	0	L1
W1_L1	0.00832	61.8	0.206	1.651	L1

4.2. AEROPROPULSIVE OPTIMIZATION OF ISOLATED ENGINE

Contrary to a single discipline optimization, as in the case of aerodynamic optimization of wing, the aeropropulsive engine optimization cases require a multi-disciplinary approach to transfer functional values between the aerodynamic and propulsion disciplines. To accomplish this, the current study employs an individual discipline feasible (IDF) architecture to pass information from the aerodynamics discipline to the propulsion discipline in a feed-forward manner and couple them using consistency constraints. The aeropropulsive optimization architecture and the corresponding aeropropulsive coupling was discussed in subsection 3.1.1. This section presents the results of aeropropulsive optimization studies of a high-bypass turbofan engine in isolation and is divided into 5 subsections:

1. The first subsection looks at a baseline engine optimization case for a GE90-like engine with a net thrust of 70kN and verifies the optimization convergence.

2. The second subsection verifies the effectiveness of non-axisymmetric nacelle design space for engine optimization at an AoA of 5°.

3. Third subsection presents the effect of including an inequality constraint for the bypass ratio instead of an equality constraint.

4. Fourth subsection looks into the design trends in engines optimized at different levels of thrust output.

5. Fifth subsection compares an engine optimization case with a finer mesh to quantify the effect of change in mesh size for optimized engine design.

The objective of these engine optimization cases is to reduce the engine fuel consumption at a specified FPR and BPR to produce a required net thrust (F_{net}) output, subject to a fan face mach number constraint, aeropropulsive coupling constraints and geometric thickness constraints. The Mach number at the fan face is constrained at 0.6 to prevent the intake fan blades from going into stall and is a typical operability constraint [16]. The net thrust and fan face Mach number constraints are normalized with respect to their target values, while the consistency constraints are normalized using CFD values with respect to their respective PyCycle counterparts. There are 5 non-geometric design variables for the engine optimization. These are the boundary state values at the inlet-outlet boundaries which manipulate the thermodynamic states at these boundaries to control quantities like mass flow rate, BPR, FPR and match the propulsion cycle outputs. These DVs include static pressure at the fan face and total pressure, total temperature at the bypass and core faces. The engine shape is controlled by a set of shape function DVs using the FFD-based parameterization discussed in subsection 3.4.2.

Table 4.4 shows a general optimization statement for all the isolated engine optimization results discussed in this section. The number of shape function DVs and thickness constraints vary with the level of non-axisymmetric design freedom. These design variables and constraints are quantified in Table 4.5 for varying levels of engine shape design freedom.

Table 4.4: Optimization statement for engine-only aeropropulsive optimizations

	Variable	Description	Quantity
minimize	$\dot{m}_{fuel}$	Fuel consumption rate (kg/s)	
with respect to	$p_{s,2}$	Static pressure at fan face	1
	$p_{t,13}$	Total pressure at bypass exit	1
	$T_{t,13}$	Total temperature at bypass exit	1
	$p_{t,5}$	Total pressure at core exit	1
	$T_{t,5}$	Total temperature at core exit	1
	$X_{shape,e}$	(Non)axisymmetric engine shape DVs	*
subject to	$F_{net,con}$	Net thrust constraint	1
	$M_2 \leq 0.6$	Fan face mach number constraint	1
	$6 \leq BPR \leq 10$	Bypass ratio constraint ‡	1
	$FPR = 1.65$	Fixed fan pressure ratio †	-
consistency constraints	$R_{p_s,13} = 0$	Static pressure residual at bypass exit	1
	$R_{\rho_s,13} = 0$	Static density residual at bypass exit	1
	$R_{\dot{m},13} = 0$	Mass flow rate residual at bypass exit	1
	$R_{area,13} = 0$	Area residual at bypass exit	1
	$R_{p_s,5} = 0$	Static pressure residual at core exit	1
	$R_{\rho_s,5} = 0$	Static density residual at core exit	1
	$R_{\dot{m},5} = 0$	Mass flow rate residual at core exit	1
	$R_{area,5} = 0$	Area residual at core exit	1
geometric constraints	$0.99 \leq g_{geo,e} \leq 1.3$	Engine thickness constraints	*

† FPR is not constrained explicitly, instead its value is fixed implicitly in PyCycle
‡ BPR is constrained only for cases with variable BPR, otherwise is fixed at 8.1 in PyCyle
* Varies depending on the level of non-axisymmetric design freedom

Table 4.5: Number of engine shape DVs for different levels of design freedom

	Longitudinal DVs			Radial DVs		
Case Type	Nacelle LE	Nacelle TE	Core-Bypass TE	Front U/L + mid nacelle	All other surfaces	Number of DVs #
E_1	-	-	-	AXIS	AXIS	88
E_2	AXIS	AXIS	AXIS	AXIS	AXIS	91
E_3	NAXIS	AXIS	AXIS	AXIS	AXIS	102
E_4	NAXIS	AXIS	AXIS	NAXIS	AXIS	399

'AXIS': axisymmetric, 'NAXIS': non-axisymmetric, '-' : DV is inactive
Number of DVs for a full 360° engine

4.2.1. BASELINE ENGINE OPTIMIZATION WITH AXISYMMETRIC DVS

An aeropropulsive optimization was performed for the baseline GE90-like engine with a net thrust constraint of 70kN using axisymmetric design variables to establish and verify the optimization methodology. Figure 4.3 shows the convergence history of this optimization. The optimality and feasibility tolerances were tolerances were both set to 10^{-6} for all engine-only optimization cases. Similar to the isolated wing optimization case, the optimizer first satisfies the feasibility constraints. At an optimality value of 10^{-4}, the objective value ($\dot{m}_{fuel}$ in kg/s) is 1.018, where the feasibility tolerance is satisfied. As the optimizer reaches the optimality tolerance of 10^{-6}, the change in objective function is less than 0.02%.

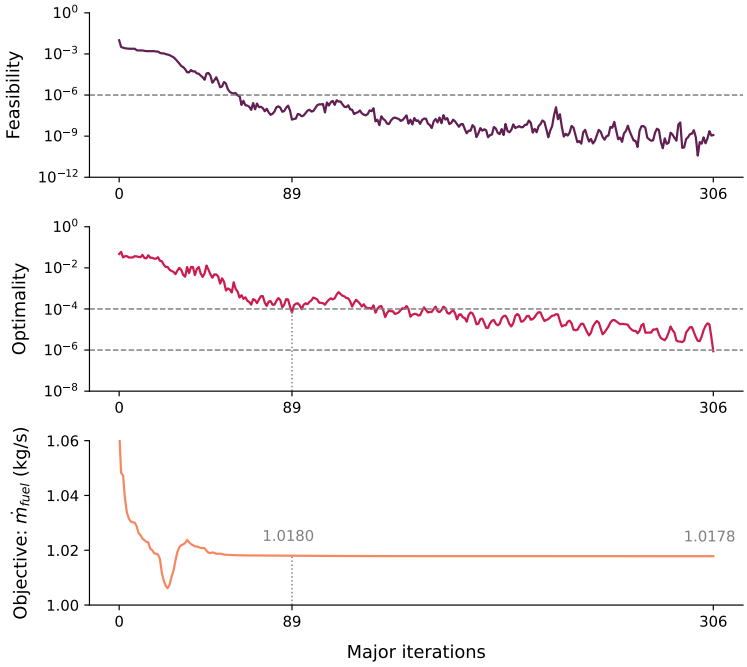

Figure 4.3: Optimization convergence history for the baseline engine optimization case with a net thrust constraint of 70 kN

Figure 4.4 further shows the convergence history of all the constraints in the engine optimization case. While the consistency and fan face Mach number constraints are relatively easily satisfied early on in the optimization, the net thrust constraint is the most difficult to satisfy. The objective function ($\dot{m}_{fuel}$) and net thrust constraint compete against each other as a lower engine thrust favours a lower fuel requirement. As the optimizer tries to reduce the objective, the net thrust constraint is initially violated, this results in a sharp drop in $\dot{m}_{fuel}$ seen in the initial iterations in Figure 4.3. As the optimizer tries to satisfy the thrust constraint, the

objective function first increases until all the constraints become feasible and then drops gradually as the engine design is optimized. The fan face Mach number constraint limits the dynamic pressure rise at the fan face. For a net thrust of 70kN, this constraint is active ($M_{2,con}$ =-1.4e-3). This effect is discussed further in subsection 4.2.4. For this baseline optimization case, the FPR and BPR values were implicitly fixed at 1.65 and 8.1 within the PyCycle analysis module and are not explicitly constrained. These values are indirectly constrained within the CFD solver through consistency constraints for the thermodynamic state variables and areas.

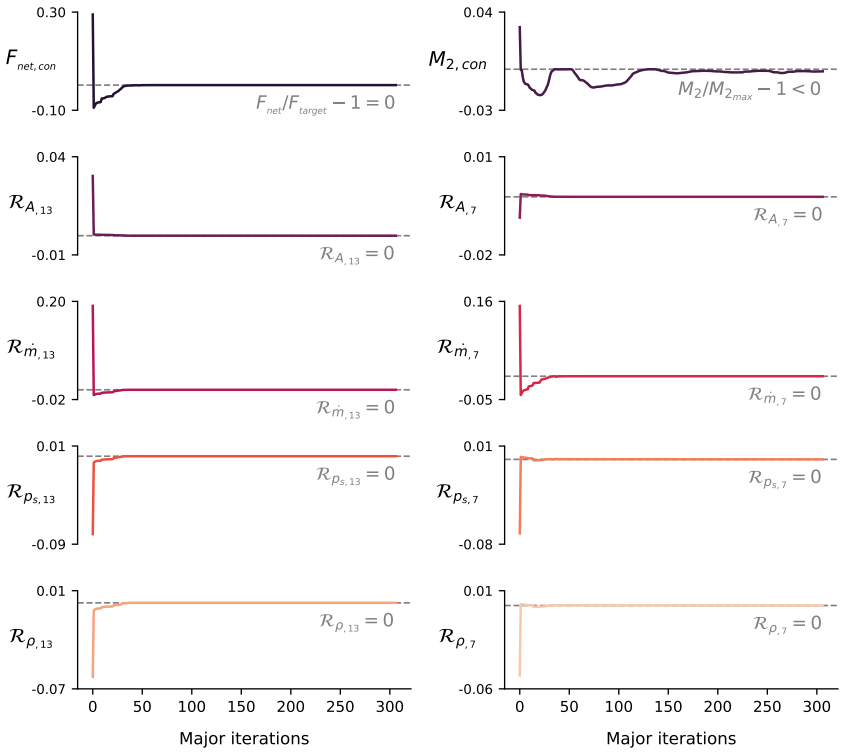

Figure 4.4: Constraint convergence history for the baseline engine optimization case with a net thrust constraint of 70 kN with fixed FPR and BPR

The optimized and baseline engine designs are compared in Figure 4.5 and Figure 4.6. The optimization starts from an infeasible initial design, with initial guess values for the engine BC estimated from a standalone PyCycle analysis. The optimized design is feasible and produces the required net thrust of 70kN. The optimizer adjusts the fan face area to control the required mass flow rate to meet the thrust constraint. Based on the inlet mass flow the bypass and core areas and states are modified to match the required FPR and BPR. The outer surface of the nacelle is modified to relieve shocks and reduce the nacelle drag

while simultaneously tweaking the bypass exit flow to relieve trailing shocks in the jet stream. As the engine operating point has a high Fan Pressure Ratio (FPR) and Bypass Ratio (BPR), the bypass nozzle is choked to ensure maximum mass flow rate, resulting in optimum pressure recovery and enhanced thrust efficiency. The core nozzle is unchoked and has a Mach number of about 0.68 at the nozzle exit. The characteristics of this optimized engine at 70kN are outlined in Table 4.6.

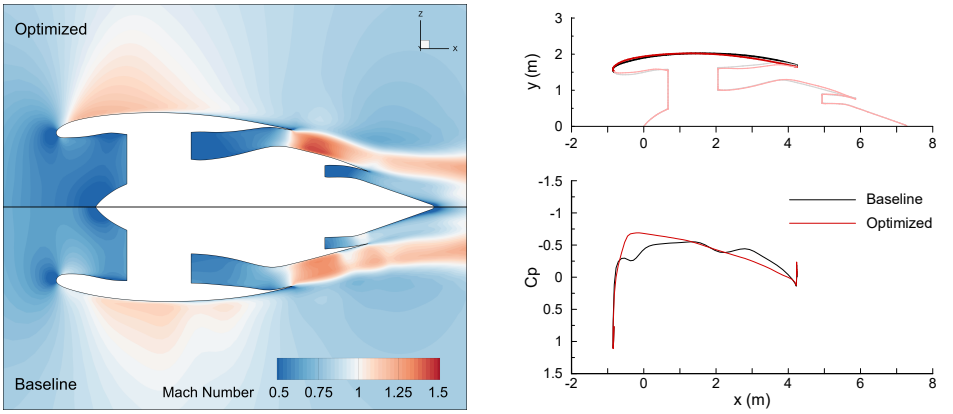

Figure 4.5: Mach number contours at the symmetry plane and C_p distribution over the outer nacelle for the baseline and optimized engine at 70kN thrust

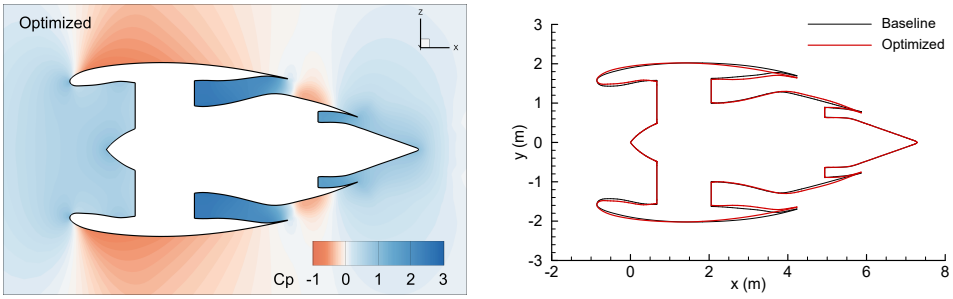

Figure 4.6: C_p contours at the symmetry plane for the optimized engine at 70kN thrust and comparison of its outline with the baseline geometry

Table 4.6: Characteristics of optimized engine at 70kN thrust with fixed FPR and BPR

Case name	$\dot{m}_{fuel}$ (kg/s)	F_{net} (kN)	BPR	FPR	Mesh size
E_1_70_L2	1.0178	70	8.1	1.65	L2

4.2.2. ENGINE OPTIMIZATION AT AN ANGLE OF ATTACK

To verify the capability of the proposed non-axisymmetric parameterization, an engine optimization study was carried out with the freestream flow at 5° AoA for the same net thrust constraint. The optimization statement for this problem is the same as the baseline engine optimization case, except for the change in angle of attack and the number of design variables and constraints. Four different optimizations are carried out with varying levels of design freedom. The results of this optimization study are shown in Table 4.7.

Table 4.7: Results for engine optimization at 5° AoA with varying levels of non-axisymmetric design changes for a thrust of 70kN

		Longitudinal DVs			Radial DVs	
Case Name	$\dot{m}_{fuel}$ (kg/s)	Nacelle LE	Nacelle TE	Core - Bypass TE	Front U/L + mid nacelle	All other surfaces
E_1_AoA_L2	1.0137	-	-	-	AXIS	AXIS
E_2_AoA_L2	1.0121	AXIS	AXIS	AXIS	AXIS	AXIS
E_3_AoA_L2	1.0117	NAXIS	AXIS	AXIS	AXIS	AXIS
E_4_AoA_L2	1.0099	NAXIS	AXIS	AXIS	NAXIS	AXIS

'AXIS': axisymmetric, 'NAXIS': non-axisymmetric, '-' : DV is inactive

As evident from Table 4.7, adding non-axisymmetric changes to the nacelle design at an angle of attack does offer benefits in fuel consumption. Adding axisymmetric chord DVs for the nacelle LE, TE and core-bypass TE walls reduces the fuel consumption by 0.16% in comparison to the axisymmetric engine design. Non-axisymmetric nacelle LE DVs with axisymmetric nacelle TE and core-bypass TE walls helps in a slightly lower value of $\dot{m}_{fuel}$. Adding radial non-axisymmetry to the upper and lower surfaces of front and mid nacelle in addition to non-axisymmetric length changes in the front nacelle offers a reduction of 0.38% in $\dot{m}_{fuel}$ with respect to the axisymmetric design. A comparison of fuel consumption with the baseline at 0° AoA is not made since a front nacelle DV was found to be touching its lower bound in the baseline case, which restricted it from contracting the inlet to reduce the mass flow rate. This is addressed in later studies.

Although the percentage gains in $\dot{m}_{fuel}$ are quite low, the improvement in flow quality, specially at the nacelle inlet is significant. Mach number contours in Figure 4.7 show that the flow over the outer nacelle wall, in the case of non-axisymmetric chord and radial DVs (E_4_AoA_L2), significantly improves on both the top and bottom nacelle surface as compared to the axisymmetric design. The supervelocities at the inlet lip are also reduced to a large extent. The E_4_AoA_L2 nacelle has a downward droop angle of about 5.76°. Interestingly, the expansion fans in the bypass stream are also affected by the incoming flow at an angle of attack. The lower bypass stream attains a higher mach number than the upper bypass stream after the exit, leading to asymmetric exhaust plumes.

This improvement in flow over the nacelle can also be seen in Figure 4.8a which shows the variation in pressure coefficient on the outer and inner nacelle surfaces at on the top and bottom side ($\psi = 0°, 180°$). The optimized nacelle shape follows a pressure distribution similar to that of a supercritical airfoil. The shocks on the lower side of the outer nacelle wall are eliminated almost entirely in the case of full non-axisymmetric design freedom (longitudinal + radial). It is interesting to note that the non-axisymmetric parameterization proposed by Tejero *et al.*[21] had weak shocks on the lower nacelle even in the optimized designs (MOO) (Figure 4.8b) while they are eliminated almost completely in case E_4_AoA_L2. Although, a finer mesh is required to capture the shocks more sharply in the current study.

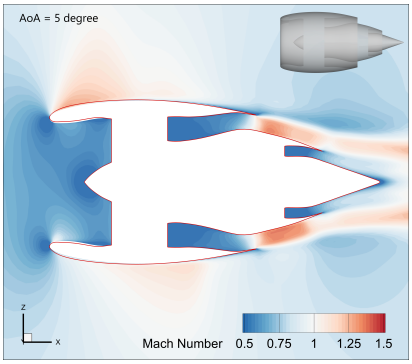

(a) Case - E_1_AoA_L2

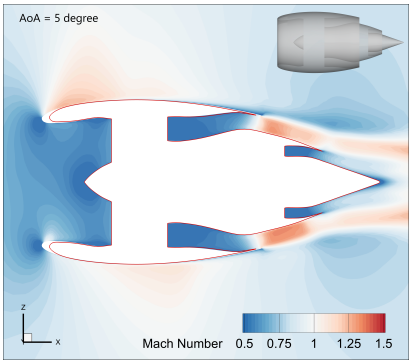

(b) Case - E_2_AoA_L2

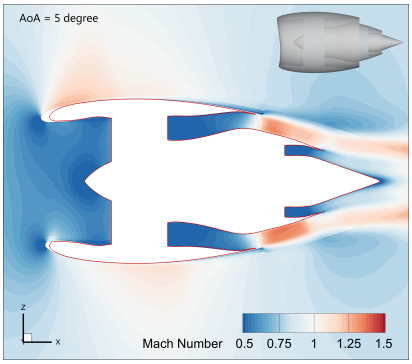

(c) Case - E_3_AoA_L2

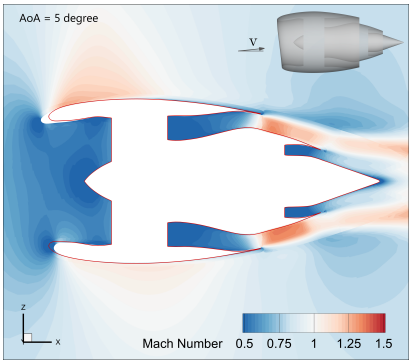

(d) Case - E_4_AoA_L2

Figure 4.7: Mach number contours for optimized engine designs at 5° AoA. The incoming flow is at 5° w.r.t. the horizontal. Red line represents a slice of the optimized engine at $AoA = 0°$ and 70kN net thrust for comparison.

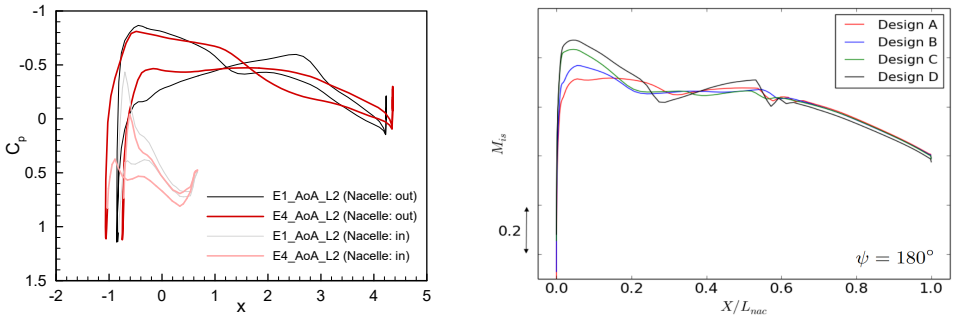

(a) C_p over the top and bottom nacelle

(b) M_{is} over the bottom nacelle [21]

Figure 4.8: (a). Plot of pressure coefficient variation from the current study using axisymmetric and non-axisymmetric nacelle DVs; (b). A comparison with optimized non-axisymmetric nacelle drag results from [21]

4

4.2.3. ADDITION OF BYPASS RATIO INEQUALITY CONSTRAINT

Previous results were obtained with a fixed value of the bypass ratio, along with a fixed fan pressure ratio, while the FPR is kept fixed at 1.65. To add this BPR constraint, the mass flow rate of the bypass boundary was passed additionally to the PyCyle model from the CFD domain and its coupled derivatives were also set up in MACH-Aero. The bypass ratio is defined as shown in Equation 4.4. It is defined as the ratio of mass flow rate at the bypass boundary in ADflow to the mass flow entering the core, which is the difference between fan flow rate and bypass flow rate. It is not defined with respect to the mass flow rate at the core boundary in ADflow because the core outflow has an added mass flow rate of the combustion fuel and bleeds. The bypass ratio constraint is set as an inequality constraint between a BPR of 6 - 10, which is typical of high bypass ratio turbofans. The net thrust constraint for this study is kept at 70kN, same as the baseline and the results are presented in Table 4.8.

$$BPR = \frac{\dot{m}^a_{13}}{\dot{m}^a_2 - \dot{m}^a_{13}} \tag{4.4}$$

Table 4.8: Characteristics of optimized engine at 70kN net thrust with a fixed value vs an inequality constraint for the BPR

Case name	$\dot{m}_{fuel}$		F_{net} (kN)	BPR	FPR	Mesh size
	value (kg/s)	Δ (%)				
E_1_70_L2	1.0178		70	8.1 (fixed)	1.65	L2
E_1_70_{BPR}_L2	1.0085	0.91	70	8.73 (6-10)	1.65	L2

For the optimized design at 70kN net thrust, the BPR converges at a value of 8.73, which is well withing the constraint range, meaning it is an inactive constraint. This variability in BPR provides a better optimum, improving the objective by 0.91%. Figure 4.9 shows total pressure contours for the two cases with different BPR. For the variable BPR case, the total pressure at the core exit nozzle decreases, which means a higher overall-pressure ratio and hence improved fuel efficiency. This reduction in total pressure is due to a reduction in both the dynamic and static pressure. Figure 4.10 shows a comparison of the engine outline and Mach number contours for these two cases. The Mach number at the core jet exit reduces from 0.68 for a BPR of 8.1 to 0.57 for the 8.73 BPR case. This reduced jet velocity for the core jet leads to higher propulsive efficiency for the unchoked core. It also causes a delayed mixing with the bypass exhaust resulting in a longer shear layer due to a larger difference in the velocities between the two jet streams. However, the total length of the combined jet is still dominated by the high-speed bypass flow.

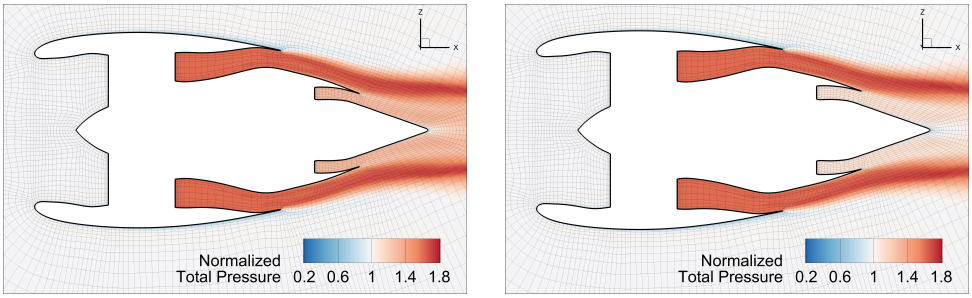

(a) BPR constrained at 8.1 (b) BPR constrained between 6-10

Figure 4.9: Total pressure contours at engine mid-plane with and without an inequality constraint for the bypass ratio

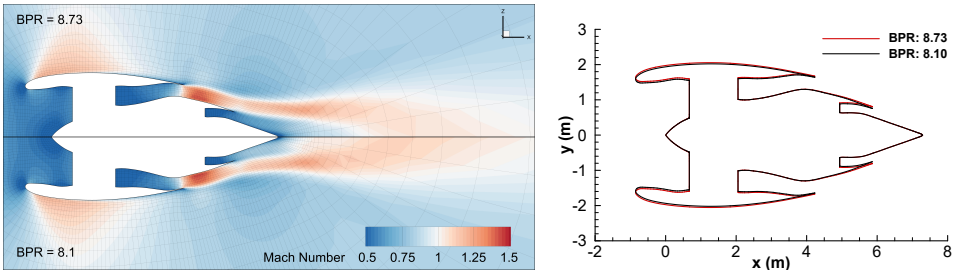

Figure 4.10: Contours of Mach number at the symmetry plane with and without an inequality constraint for BPR and comparison of their outlines

Figure 4.11 presents a comparison of the pressure and momentum force contributions from the fan face, core and exhaust boundaries. It can be seen that for the core exit, the pressure force reduces by a larger extent than the momentum force due to a larger change in the exit static pressure. The minor reduction in core momentum force, and the corresponding mach number, is due to a higher bypass ratio. This reduction in core thrust is compensated by an increased bypass thrust to maintain a net thrust of 70kN, in exchange for having a lower total pressure at the core exit for a higher OPR. The increased bypass thrust comes at the cost of an increased drag due to momentum force at the fan face. Since the FPR is fixed, to maintain an adequate mass flow through the core while increasing the bypass ratio, the fan area increases to increase the inlet mass flow rate, leading to a trade-off between the fan and bypass force components.

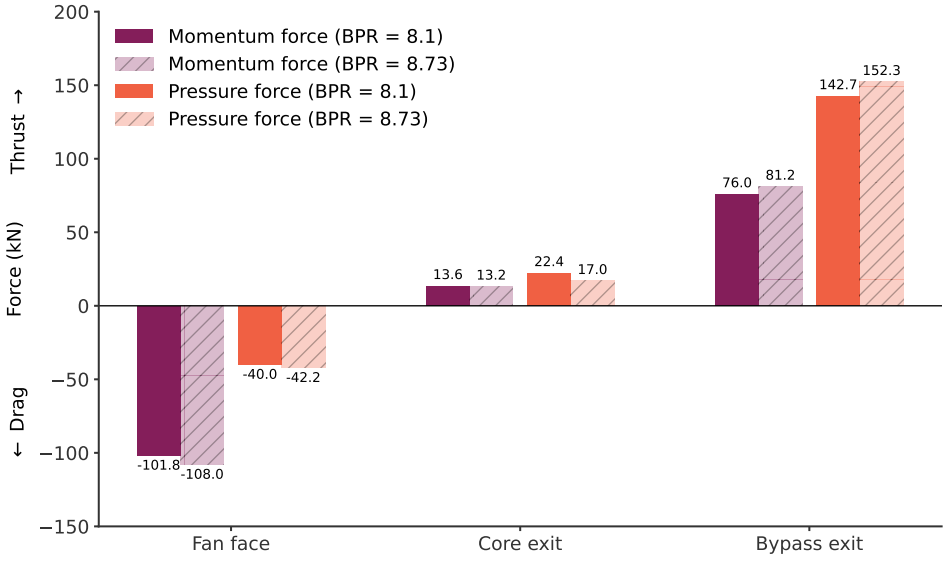

Figure 4.11: Comparison of momentum and pressure forces on the inlet/outlet boundaries for the two BPR constraint cases

Thus, adding an inequality constraint for the BPR, leads to an optimum BPR at a fixed FPR. All further studies this work include this BPR inequality constraint. In an effort to quantify the contribution of forces from the walls and boundaries of the engine, Figure 4.12 presents a detailed drag and thrust breakdown for the optimum BPR case. The bypass nozzle produces the majority of the net thrust, which is typical for a turbofan engine. The contribution of outer nacelle drag is quite small as it produces a drag of approximately 4kN (5.7% of the net thrust). However, this is expected to be greater when the engine is mounted onto the airframe. The inner lip of the nacelle produces a small positive thrust since the shape of the inlet essentially increases the pressure of the incoming flow by acting as a diffuser.

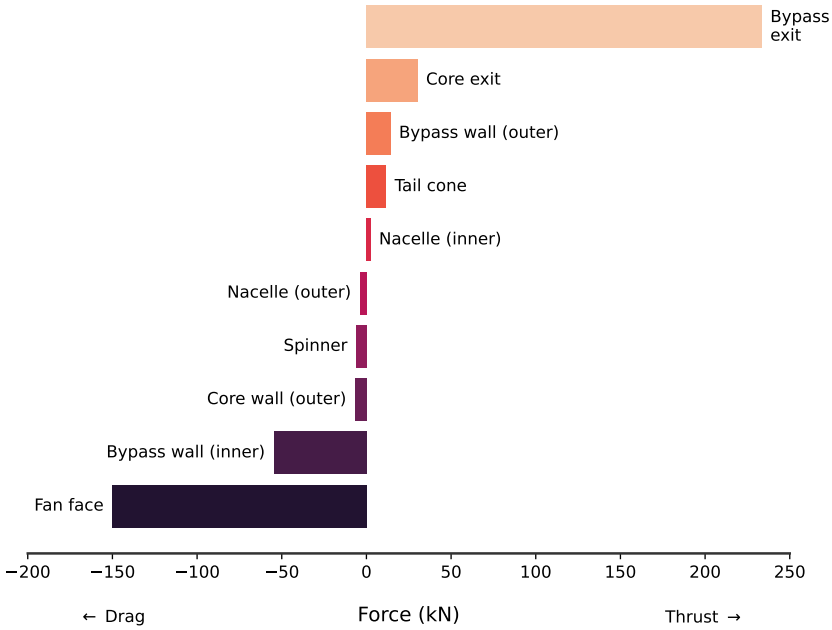

Figure 4.12: Breakdown of forces on the engine surfaces for engine optimization case at 70kN thurst and an optimum BPR of 8.73 at a FPR of 1.65

4.2.4. EFFECT OF ENGINE THRUST VARIATION

To understand the optimum design and performance of engine under different thrust requirements, a thrust variation study is performed with a net thrust constraint varying from 70kN to 100kN. This range of thrust constraint is selected because the optimized isolated wing has a net drag of 84kN ($C_{D,wing}$ = 0.00944) and integrating the engine onto the wing will result in a further increase in wing drag. An inequality constraint is used for the BPR bounded between 6 to 10 and a fixed FPR of 1.65.

Table 4.9: Results of the engine optimizations for different net thrust constraints

Case name	$\dot{m}_{fuel}$		F_{net}	TSFC	$\dot{m}_2$	BPR	FPR	Mesh
	value (kg/s)	Δ (%)	(kN)	(g/kN/s)	(kg/s)	(6-10)	(fixed)	size
E_1_70$_{BPR}$_L2	1.0085		70	14.408	293.5	8.730	1.65	L2
E_1_80$_{BPR}$_L2	1.1468	13.7	80	14.335	333.8	8.729	1.65	L2
E_1_90$_{BPR}$_L2	1.2862	12.2	90	14.291	374.3	8.728	1.65	L2
E_1_100$_{BPR}$_L2	1.4256	10.8	100	14.256	414.9	8.728	1.65	L2

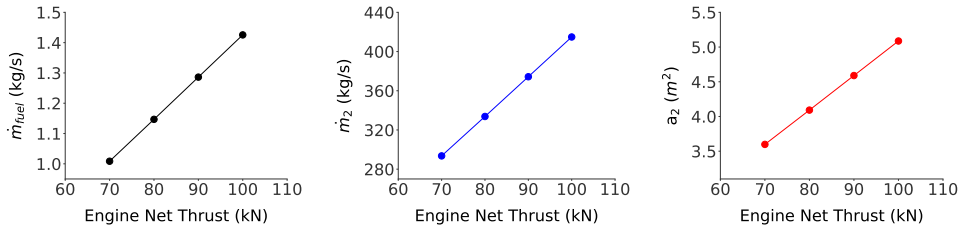

Figure 4.13: Variation of $\dot{m}_{fuel}$, $\dot{m}_2$ and fan face area (a_2) for optimum engine designs at different net thrust constraints

Table 4.9 outlines the performance of these optimized engine designs at different thrust constraints. The engine fuel consumption increases almost linearly with increasing thrust for the fixed FPR, with an almost constant thrust specific fuel consumption (TSFC). For all values of the net thrust constraint, the BPR constraint converges at 8.73. The increase in engine thrust is purely driven by an increase in the engine inlet mass flow. As the fan face Mach number is a limiting constraint, this increase in fan mass flow is obtained by increasing the fan face area, which also grows linearly with thrust due to a linear growth in the fan mass flow. This linear growth of engine fuel consumption, fan face mass flow rate and fan face area are visualized in Figure 4.13 and the corresponding mach number contours with inlet streamlines are presented in Figure 4.14. The overall flow features remain consistent in all the designs, the main feature being that the engine radius increases to accommodate the required increase in mass flow rate at higher thrust constraints.

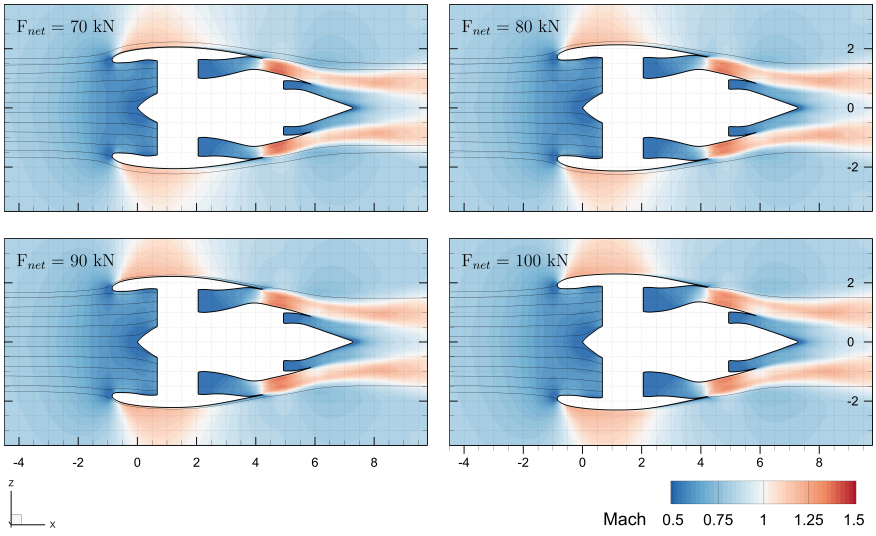

Figure 4.14: Mach number contours at the symmetry plane with streamlines at the inlet nacelle for optimized engine designs at different thrust constraints

4.2.5. COMPARISON OF FINE AND COARSE MESH ENGINE OPTIMIZATIONS

In order to verify the use of a coarse mesh optimizations for trade studies, a comparison of coarse (L2) and medium (L1) mesh optimization is carried out at a net thrust constraint of 95kN. The results of these optimizations with different mesh sizes are presented in Table 4.10. As shown previously in subsection 3.3.4, the difference in fuel consumption for the baseline unoptimized engine using L1 and L2 mesh was 1.21%. For a net thrust of 95kN, the difference in the optimized engine fuel consumption is 1.76%. This difference in the refinement error is expected due to a error in the averaging of the fan face, bypass and core boundaries. Figure 4.15 shows the outlines and mach number contours with mesh overlay for the 95kN thrust optimized designs with L1 and L2 meshes. In the optimized L1 design, the bypass flow reaches a higher mach number than the coarse optimized design. There are minor changes in flow velocities ahead of the fan face, but overall flow features are the same for both the designs. A comparison of their outlines in Figure 4.15b shows that the main difference in the two designs is in the nacelle lip highlight diameter. As also observed in the wing optimization results with medium and coarse meshes, the trend studies within a specific mesh size are consistent with the optimizations using finer meshes. These coarse mesh optimization results also serve as a good starting point for future fine mesh optimizations.

Table 4.10: Comparison of optimized engine designs with different mesh sizes

Case name	$\dot{m}_{fuel}$		F_{net}	TSFC	$\dot{m}_2$	BPR	FPR	Mesh
	value (kg/s)	Δ (%)	(kN)	(g/kN/s)	(kg/s)	(6-10)	(fixed)	size
E_1_95$_{BPR}$_L1	1.3325		95	14.027	401.8	9.08	1.65	L1
E_1_95$_{BPR}$_L2	1.3560	1.76	95	14.274	394.6	8.73	1.65	L2

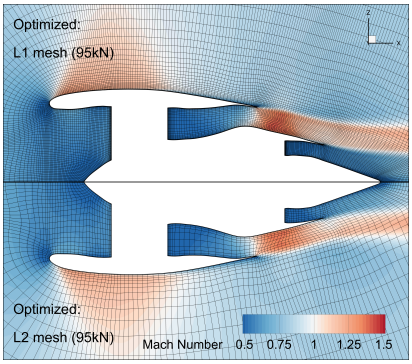

(a) Mach number contours

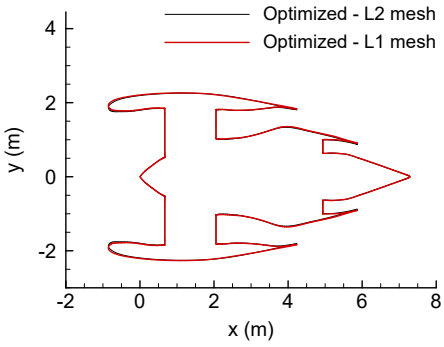

(b) Optimized engine outlines

Figure 4.15: Comparison of coarse (L2) and medium (L1) mesh optimized designs and flow features at the symmetry plane for a net thrust of 95kN

4.3. AEROPROPULSIVE OPTIMIZATION OF ENGINE - INTEGRATED AIRFRAME

In order to realize and quantify the complete benefits of non-axisymmetric nacelle designs, it is essential to look at the engine performance in combination with the aircraft wing. For this purpose, this section looks at the combined performance of the engine-integrated airframe. Although minimizing the wing drag could be a good objective, a better objective is to look at the engine fuel consumption rate, $\dot{m}_{fuel}$ (kg/s), since this value directly translates into the aircraft operating cost. Hence, the objective of the integrated engine-airframe optimization studies performed in this section is to minimize $\dot{m}_{fuel}$. This objective also enables to make a direct comparison with the performance of the unmounted engine. Table 4.11 shows a general optimization statement for the integrated engine-airframe aeropropulsive optimizations performed in this section.

The design variables for this engine-wing integrated optimization are a combination of the design variables for the isolated wing and engine optimization cases. Additionally, there are two translation DVs for the relative change in position of the wing, with respect to the engine. This mimics the engine being translated in the frame of reference of the wing. Since the current study does not take into account the trim constraint, the engine and the freestream flow are fixed at 0° AoA. To achieve this, the global AoA DV is removed and the central wing section twist is added as a design variable to change the angle of attack of the entire wing with twist DVs. The wing shape can also change using 120 local shape DVs. Additionally the engine nacelle can have both axisymmetric and non-axisymmetric design changes. Except the nacelle DVs, all other engine DVs provide axisymmetric deformation. This integrated engine-airframe parameterization was explained in detail in subsection 3.4.3.

Due to the presence of the engine model and the aeropropulsive coupling, all engine design and consistency constraints are the same as the isolated engine optimization case. The only change is that the engine net thrust (F_{net}) constraint is removed and replaced by a net zero drag constraint ($Drag_{w+e} = 0$). In the cruise flight condition a horizontal force balance exists and the net forces in the flight direction are balanced. This constraint on $Drag_{w+e}$ ensures that the net thrust generated by the engine counters the net drag produced by the wing. Additionally the lift constraint is modified to the take into account the lift generated by the entire engine-wing system ($C_{L,w+e} = 0.206$). The geometric constraints for the wing and engine are also the same as in the isolated optimization cases. The only additional geometric constraint is the proximity constraint which prevents the wing and engine geometries intersecting with each other. All these constraints are normalized with their target values. These design constraints were explained in subsection 3.5.3. Due to the large computational size of this problem (1M cells), based on the results of unmounted engine and wing optimizations, an optimality tolerance of 5e-4 was used for these studies with a feasibility tolerance of 1e-6.

This section contains results of the aeropropulsive optimization of the integrated engine-wing system with increasing levels of design freedom. At first, the optimization is performed with the engine and wing locations being fixed at an initial location to establish a baseline, with the nacelle having only axisymmetric DVs (E_1WI-1). The second study looks at the effect of optimizing the relative location of the engine with respect to the wing, by translating the wing in the frame of reference of the engine, with the nacelle DVs still being axisymmetric (E_1WI-2). The third study takes into account the non-axisymmetric nacelle DVs in addition to the relative engine placement DVs (E_4WI-3). These increasing levels of design freedoms help quantify the sensitivity of engine fuel consumption to these design variables.

Table 4.11: Optimization problem statement for integrated engine-airframe aeropropulsive optimization case

	Variable	Description	Quantity
minimize	$\dot{m}_{fuel}$	Fuel consumption rate (kg/s)	
with respect to	$p_{s,2}$	Static pressure at fan face	1
	$p_{t,13}$	Total pressure at bypass exit	1
	$T_{t,13}$	Total temperature at bypass exit	1
	$p_{t,5}$	Total pressure at core exit	1
	$T_{t,5}$	Total temperature at core exit	1
geometric design variables	twist	Sectional twist DVs for the wing	12
	$X_{shape,w}$	Shape DVs for the wing	120
	$X_{shape,e}$	(Non)axisymmetric engine shape DVs	88 (399)
	$\Delta_{x,w}$	Horizontal translation of wing w.r.t. engine	1
	$\Delta_{z,w}$	Vertical translation of wing w.r.t. engine	1
subject to	$C_{L,w+e} = 0.206$	Aircraft lift constraint	1
	$Drag_{w+e} = 0$	Net zero drag constraint	1
	$M_2 \leq 0.6$	Fan face mach number constraint	1
	$6 \leq BPR \leq 10$	Bypass ratio constraint	1
consistency constraints	$R_{p_s,13} = 0$	Static pressure residual at bypass exit	1
	$R_{\rho_s,13} = 0$	Static density residual at bypass exit	1
	$R_{\dot{m},13} = 0$	Mass flow rate residual at bypass exit	1
	$R_{area,13} = 0$	Area residual at bypass exit	1
	$R_{p_s,5} = 0$	Static pressure residual at core exit	1
	$R_{\rho_s,5} = 0$	Static density residual at core exit	1
	$R_{\dot{m},5} = 0$	Mass flow rate residual at core exit	1
	$R_{area,5} = 0$	Area residual at core exit	1
geometric constraints	$0.5 \leq g_{proximity} \leq 1.5$	Engine-wing proximity constraint	10
	$0.99 \leq g_{vol,w} \leq 1.2$	Wing volume constraint	1
	$0.99 \leq g_{geo,e} \leq 1.3$	Engine thickness constraints	65
	$0.7 \leq g_{geo,w} \leq 1.5$	Wing thickness constraints	144

4.3.1. ENGINE-AIRFRAME OPTIMIZATION AT BASELINE ENGINE LOCATION

The initial chordwise engine location is estimated based on the BWB-400 nacelle location [4], while the spanwise location was based on the limiting moment of one-engine out condition. The initial vertical placement of the engine was arbitrary and chosen to help ease the structured mesh generation for the engine-airframe configuration. For this fixed initial engine location, Figure 4.19 shows the Mach number contours of the baseline and optimized design with an axisymmetric nacelle. The presence of a strong shock in the contraction region between the nacelle and wing can be very clearly observed for the baseline case in both the Mach number and the qualitative shadowgraph contours. The baseline wing also has shocks on the pressure and suction sides.

In the absence of an wing translation DV, the optimizer increases the local twist for the wing section at the engine location in an attempt to increase the distance between the wind and the nacelle to slow down the local flow. In addition to this, a negative camber is present at the trailing edge in the optimized wing, which follows the outer nacelle contour for a smoother flow in the channel between the engine and the wing. These changes together with local shape changes in the engine design, weaken the shock present in the contraction region. A weak shock is also present at the upper inlet lip of the nacelle.

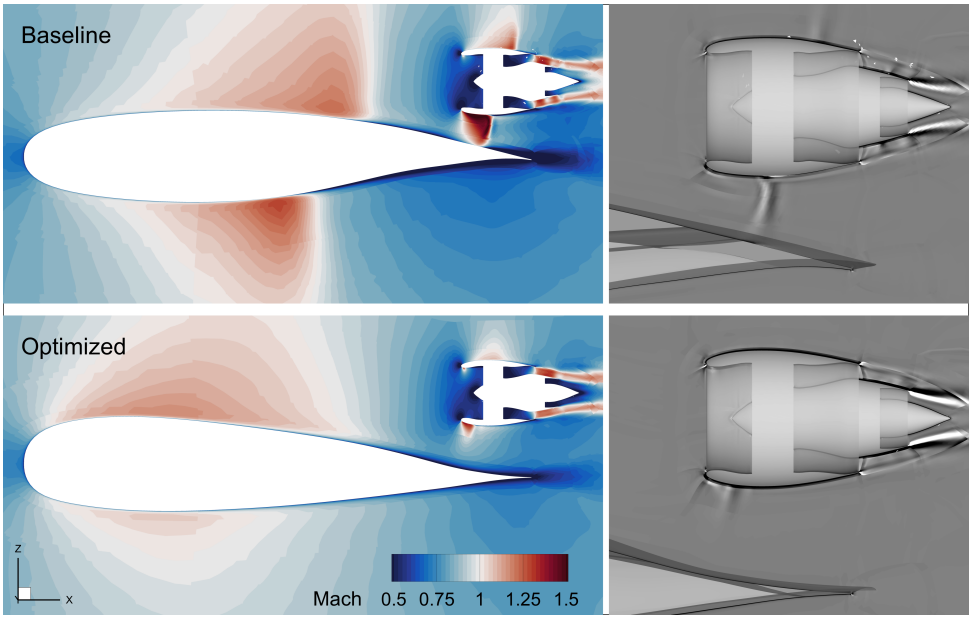

Figure 4.16: Mach number contours at the engine mid-plane and qualitative shadowgraphs for the baseline engine-airframe design vs the optimized design at initial engine location with an axisymmetric nacelle

Although the initial design was infeasible, the optimized design satisfies all the constraints to achieve the feasibility tolerance. Thus the net aircraft drag is zero and satisfies the required lift coefficient of 0.206. Details of the optimized aircraft design are shown in Figure 4.19. A high engine location and local wing modifications to remove the shocks in the contraction region, lead to a loss of lift at the inboard wing. Away from the engine, this wing has a twist and lift distribution similar to the optimized isolated wing. To compensate the loss of lift in the inboard region, the optimized wing has the outboard wing at a relatively higher AoA using a larger twist value. However, this increased lift at the outboard section comes at the cost of higher wing drag. The optimized wing design has a drag of 107 kN with a $C_{D,w}$ of 0.012011, which is much higher than that of the optimized isolated wing (84 kN). To achieve an equivalent net thrust, the engine intakes a large mass flow of 809.6 kg/s, with a high BPR of 9.03. This high thrust requirement leads to a fuel consumption rate of 1.349 kg/s. Interestingly, this fuel consumption is less than that of the unmounted engine at 100 kN thrust. This reduction in fuel consumption is due to a higher total pressure of the engine inflow in the presence of the wing. This benefit of the OWN BWB configuration for the engine performance is discussed later in section 4.4. The characteristics of the optimized design for this case are given in Table 4.12.

Table 4.12: Results of engine-airframe optimization at the initial mounting location

Case name	$\dot{m}_{fuel}$ (kg/s)	$C_{D,w}$	$C_{D,w+nac}$	$C_{L,w}$	$\frac{p_{t,2}}{p_{t,\infty}}$	BPR (6-10)	FPR (fixed)
E_1WI-1	1.3491	0.01201	0.01199	0.20776	0.99394	9.03	1.65

4.3.2. EFFECT OF RELATIVE ENGINE PLACEMENT DV

The mounting location of the engine on the wing significantly affects the drag characteristics of the integrated engine-airframe. Sensitivity studies by Renganathan *et al.* [9] found that for a CTW-OWN configuration the engine-airframe drag reduces as the nacelle moves closer to the wing in the vertical direction, while the pressure recovery of the engine improves as the engine moves vertically away from the wing. They predicted that due to the non-linear behaviour of installation drag with the spanwise engine location, a local minima might exist when the nacelle inlet is close to the trailing edge. The following study looks into these claims for the case of an over-the-wing mounted engine for the BWB, by optimizing the engine and wign shape simultaneously with design variables for wing translation to optimize the engine mounting location.

Figure 4.17a shows the Mach number contours and the optimized engine geometries for this engine placement optimization study. The engine moves closer to the leading edge and vertically downward close to the wing as compared to the initial location. The strength of shocks at the outer lower lip and the upper inner

lip are reduced as compared to case E_1WI-1, where the engine location was fixed. The negative camber present at the wing trailing edge in the previous study is no longer present. **The addition of an engine placement design variable reduces the wing drag by a significant 11.5%** compared to the optimized design in the case E_1WI-1 where the engine location was kept fixed. This results in a 2.32% decrease in engine fuel consumption rate. This confirms the high sensitivity of wing drag and engine performance to the engine mounting location. It was observed that the wing translation DVs were well within the bounds for the optimal design. Thus there is an optimum location for the placement of the engine in an OWN BWB configuration for minimum fuel consumption. Table 4.13 lists the performance characteristics of this optimized design.

Table 4.13: Results of engine-airframe optimization with engine placement DV

Case name	$\dot{m}_{fuel}$ (kg/s)	$C_{D,w}$	$C_{D,w+nac}$	$C_{L,w}$	$\frac{p_{t,2}}{p_{t,\infty}}$	BPR (6-10)	FPR (fixed)
E_1WI-2	1.3178	0.01063	0.01145	0.20637	0.99432	8.72	1.65

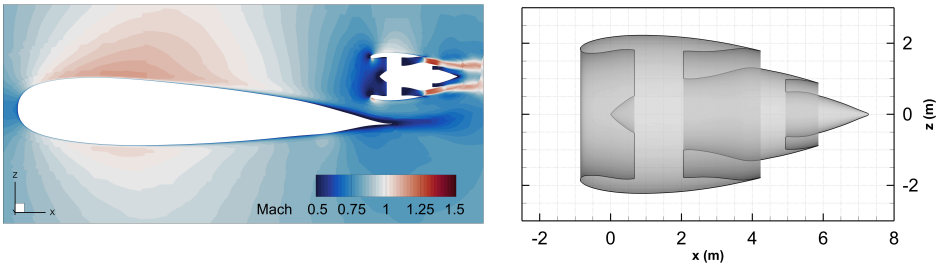

(a) Optimized design for case: E_1WI-2

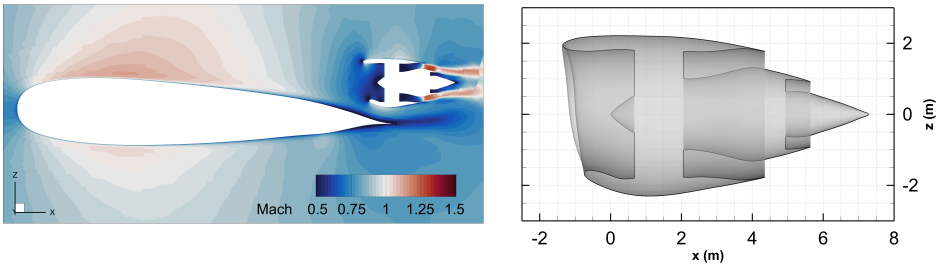

(b) Optimized design for case: E_4WI-3

Figure 4.17: Mach number contours at the engine mid-plane and optimized engine geometries for Engine-Wing Integration cases E_1WI-2 and E_4WI-3

4.3.3. EFFECT OF NON-AXISYMMETRIC NACELLE DESIGN

The benefits obtained in the engine placement optimization with an axisymmetric nacelle are quite significant. However, the shocks at the inlet lip of the nacelle were still present. subsection 4.2.2, a non-axisymmetric nacelle design can reduce shocks over the inlet nacelle lip in cases where the incoming flow is at an angle of attack. The presence of wing ahead of the engine, causes a change in the direction of the local engine inflow, which changes with the change in the shape of the engine and wing and their relative location. Hence, this optimization study looks into the effect of adding non-axisymmetric nacelle design variables to the E_1WI-2 case where the engine mounting location could be varied.

The optimized engine design and the corresponding Mach number contours at the engine-mid plane are presented in Figure 4.17b. A qualitative comparison with Figure 4.17a shows that the shocks at the inlet lip have been removed in the optimized design with non-axisymmetric DVs. The optimized engine has a downward droop and a small scarf angle. Since the nacelle design is highly non-axisymmetric, these parameters are not quantified. The quantitative performance parameters for the optimized design are listed in Table 4.14 and are compared with the previous two integrated engine-wing optimization cases.

Table 4.14: Results of engine-airframe optimization with engine placement DV

Case	$\dot{m}_{fuel}$		$C_{D,w}$	$C_{D,w+nac}$	$C_{L,w}$	$\frac{p_{t,2}}{p_{t,\infty}}$	BPR	FPR
name	(kg/s)	Δ (%)					(6-10)	(fixed)
E_1WI-1	1.3491		0.01201	0.01199	0.20776	0.99394	9.03	1.65
E_1WI-2	1.3178	2.319	0.01063	0.01145	0.20637	0.99432	8.72	1.65
E_4WI-3	1.3033	1.104	0.01072	0.01173	0.20553	0.99495	8.72	1.65

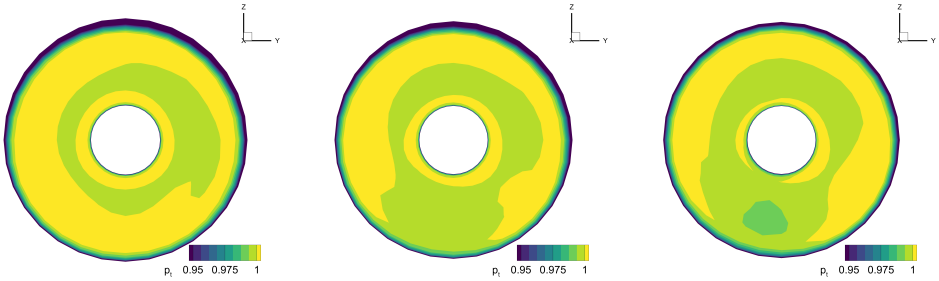

(a) Case: E_1WI-1 (b) Case: E_1WI-2 (c) Case: E_4WI-3

Figure 4.18: Normalized total pressure contours at the engine fan face for all three engine-wing integration cases

Adding the non-axisymmetric nacelle design variables reduces the fuel consumption rate by 1.1% compared to the axisymmetric optimal design in E_1WI-2 and by 3.4% compared to the optimal design in E_1WI-1. The optimized nacelle in the E_1WI-2 study, produces a very small thrust instead of drag. This is due to the presence of a shock in the lower nacelle, which increases the pressure near the aft nacelle in the contraction region, causing a small amount of thrust. The optimizer finds a trade-off for reducing the nacelle drag at the expense of the wing drag while trying to improve the fuel efficiency due to a restricted design space. An interesting feature to observe in these optimization studies is that the optimal design with a non-axisymmetric nacelle in E_4WI-3 has a higher wing and nacelle drag in comparison to the axisymmetric nacelle design in E_1WI-2, while the non-axisymmetric design has a lower fuel consumption. There is a difference of 2.5kN in the combined wing-nacelle drag between the two designs. This means that the design for minimum engine fuel consumption is not the one with the minimum wing and nacelle drag. There is a weak trade-off between the combined wing-nacelle drag and a higher pressure ratio at the fan face to obtain a better fuel efficiency. It is recommended to further verify these results with a finer mesh and check if this trend holds even in the presence of a trim constraint with acceptable engine moments.

Inlet efficiency (η_i) is defined as the ratio of total pressure at the fan face ($p_{t,2}$) to the total pressure in the freestream ($p_{t,\infty}$). Figure 4.18 shows the normalized total pressure (with respect to the freestream) at the engine fan face which reflects the inlet efficiency. The difference can be mainly seen in two regions: at the fan tip region near the nacelle wall and at the lower region of fan face which is closer to the wing. Changing the engine location improves the intake pressure ratio mainly at the lower fan face. The non-axisymmetric nacelle design also improves the pressure recovery at the fan tip region, by eliminating the shocks at the nacelle lip and reducing flow separation. However, there is a need to quantify the fan face distortion parameter and add a suitable constraint to reduce this distortion.

Figure 4.19 provides a further detailed comparison of the changes in the optimum design with engine placement and non-axisymmetric nacelle DVs (E_4WI-3) versus the axisymmetric optimal case at the fixed initial engine location (E_1WI-1). A rear engine placement in the optimal E_4WI-3 design improves the spanwise lift distribution, especially at the inboard region. Since the outboard wing no longer needs to produce extra lift to compensate this loss, the twist distribution has a lower twist for all sections, and hence a lower wing drag. A clean twist distribution was not be obtained from the CFD solver at the location of the engines, leading to sudden drop in the twist at this location. The airfoil pressure distribution shows that the flow improves on both the pressure and suction sides of the wing and the previously present weak shocks near the leading edge at the 33% spanwise section are eliminated. Overall, the engine placement DV has the largest effect on the integrated engine-airframe performance and adding non-axisymmetric design variables to the nacelle can further improve the fuel efficiency by improving the intake flow quality and the pressure ratio.

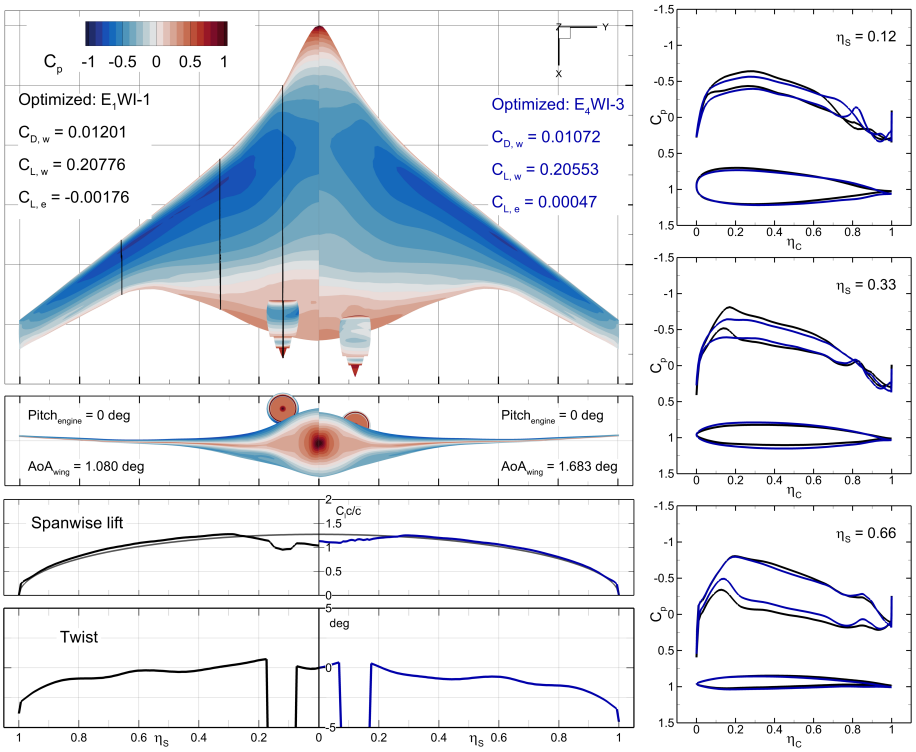

Figure 4.19: Results of aeropropulsive optimization of engine-integrated airframe with design variables for engine placement and non-axisymmetric nacelle

4.4. COMPARISON OF ISOLATED AND INTEGRATED ENGINE-AIRFRAME OPTIMIZATIONS

This section summarizes all the optimization studies and compares key results from the isolated and integrated engine-wing optimization. The main optimization results and the corresponding design variables used in these studies are listed in Table 4.16 and Table 4.15. Table 4.16 compares the performance characteristics of the optimized designs for all the three cases studied in this report: isolated wing optimization, isolated engine optimization and combined engine-airframe optimization. The isolated engine case is presented from the axisymmetric engine optimization study with a 95kN thrust constraint since it matches closely with the thrust requirement in the integrated engine-airframe optimizations. The three cases in the integrated engine-airframe optimization correspond to the optimizations with increasing design freedom: starting with axisymmetric nacelle DVs, then adding engine placement DVs and finally using the non-axisymmetric nacelle DVs in combination with the engine placement DVs.

Table 4.15: Summary of design variables used in the main optimization studies

Case name	AoA$_w$	twist	$X_{shape,w}$	$X_{shape,e}$		BC DVs*	$\Delta_{x,w}$	$\Delta_{z,w}$
				AXIS	NAXIS			
Isolated wing optimization								
W1_L2	•	•†	•					
Isolated engine optimization								
E$_1$_95$_{BPR}$				•		•		
Integrated engine-wing optimizations								
E$_1$WI-1	‡	•	•	•		•		
E$_1$WI-2	‡	•	•	•		•	•	•
E$_4$WI-3	‡	•	•	•	•	•	•	•

* BC DVs: Boundary Condition DVs for engine: $p_{s,2}$, $p_{t,5}$, $T_{t,5}$, $p_{t,13}$, $T_{t,13}$
† Twist DV is inactive for central section, AoA DV is used to change wing's AoA
‡ Twist DV is active for central section to change wing's angle, AoA DV is not used

Table 4.16: Summary of the main optimization results

Case name	$\dot{m}_{fuel}$ (kg/s)	D_w (N)	$F_{net,e}$ (N)	D$_{nac}$ (N)	$C_{L,w}$	η_i (%)	BPR (6-10)	FPR (fixed)	mesh
Isolated wing optimization									
W1_L2	-	84064	-	-	0.206	-	-	-	L2
Isolated engine optimization									
E$_1$_95$_{BPR}$	1.3560	-	95000	2017	-	99.383	8.728	1.65	L2
Integrated engine-wing optimizations									
E$_1$WI-1	1.3491	106970	106970	-202	0.20775	99.394	9.030	1.65	L2
E$_1$WI-2	1.3178	94658	94658	7294	0.20637	99.432	8.720	1.65	L2
E$_4$WI-3	1.3033	95502	95502	8973	0.20553	99.495	8.728	1.65	L2

All these results are compared at the same mesh level (L2) for both engine and wing meshes to minimize any differences in results due to mesh refinement.

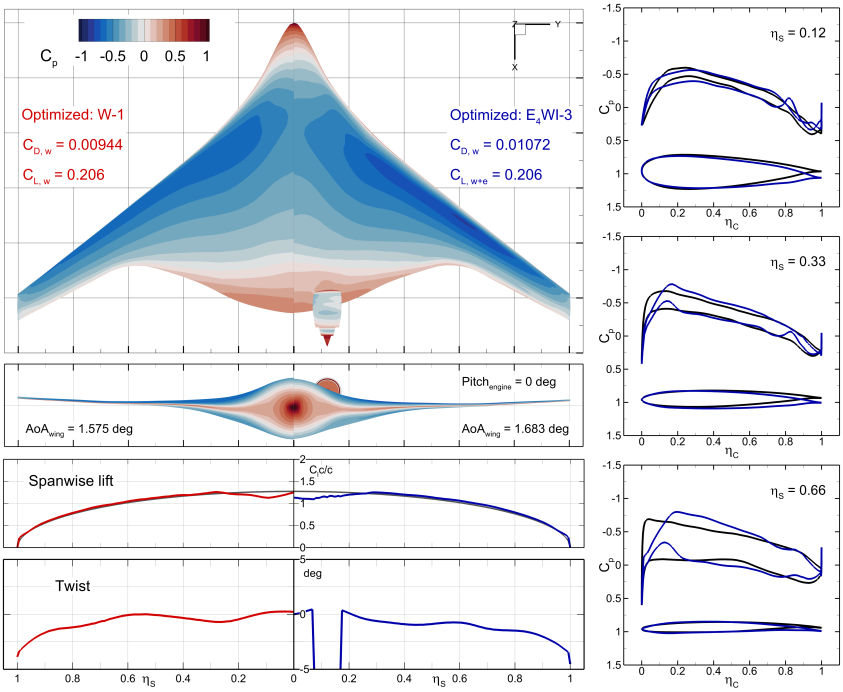

Figure 4.20: Comparison of optimized designs of isolated wing vs engine-integrated airframe (airfoils sections shown for the isolated wing case are untwisted)

From Table 4.16, it can be observed that even for the best integrated engine-wing optimization case, the wing drag is 13.6% higher than the optimized clean wing. This is a significant increase in wing drag, for which the engine needs to be sized for about 95.5kN thrust. The outer nacelle drag increases by 6.96kN from the isolated case, corresponding to a rise of 345%. Figure 4.19 shows that the optimized wing design in isolation vs with an OWN, have different twist and pressure distributions, even in the outboard region away from the engine. This increased drag, together with the differences in the design of the optimized wing in these cases highlights the importance for optimizing the engine and wing in an integrated manner.

Interestingly, comparing the performance of the optimized isolated engine with the optimized over-the-wing mounted engine with a non-axisymmetric nacelle shows that the engine's fuel efficiency improves by 3.89%, resulting in a 4.4% decrease in TSFC. Even for the worst case of 107 kN wing drag, the fuel consumption rate is 0.5% better than that of the isolated engine at 95 kN thrust. This benefit is due to an improvement in the inlet efficiency from the over-the-wing engine placement. As the flow first accelerates and then decelerates over the wing, the flow velocity decreases, and its static pressure rises towards the trailing edge. This precompression and diffusion of the flow before the engine intake results in a higher inlet efficiency than for an engine in isolation, leading to better fuel efficiency.

5

CONCLUSIONS

The work performed in this thesis focused on conducting mixed-fidelity aeropropulsive design optimizations for a Blended Wing Body aircraft using varying levels of design freedom, including engine placement and non-axisymmetric nacelle design variables. This objective was motivated by a gap in the literature, where most studies have examined engine-airframe integration from an aerodynamic point of view without considering its combined effects with the propulsion system. A few studies have explored sensitivity analysis for over-the-wing mounted engine-airframe integration, but a detailed optimization study investigating the benefits of aeropropulsive trade-offs was still lacking. This study addresses these literature gaps and answers the research questions stated in Chapter 1.

5.1. CONTRIBUTIONS

In order to address the research objectives, a coupled aeropropulsive methodology was developed by extending the MACH-Aero framework, which was primarily designed for high-fidelity optimization. An Individual Discipline Feasible architecture was used to connect the ADflow CFD solver with the PyCycle 1D thermodynamic library to perform mixed-fidelity aeropropulsive optimizations. To facilitate gradient-based optimizations with the high-fidelity ADflow solver, a total derivative calculation was implemented in MACH-Aero to calculate the sensitivities of the PyCycle outputs with respect to the CFD outputs. These coupled gradients were verified using finite difference calculations, ensuring optimization convergence.

The engine model developed in this study uses one subsonic outlet boundary condition at the fan face and two subsonic inlet boundary conditions for the bypass and core inlets. During the course of this work, an incorrect implementation of these boundary conditions in the ADflow solver was identified and corrected. Additionally, the existing parameterization schemes in MACH-Aero did not directly allow for non-axisymmetric deformations. To address this, an overlapping, circular FFD-based parameterization scheme was developed, demonstrating the capability to perform complex non-axisymmetric deformations successfully while achieving successful optimization convergence.

5.2. OBSERVATIONS AND ANSWERS TO THE RESEARCH QUESTIONS

To address the research questions stated in Chapter 1, the aeropropulsive optimization of the integrated engine-airframe configuration was explored progressively. First, a single-discipline aerodynamic optimization was conducted to optimize the baseline BWB aircraft wing in isolation. Next, multidisciplinary aeropropulsive optimizations were performed on a GE90-like turbofan engine in isolation to verify the non-axisymmetric parameterization and characterized the isolated engine performance with increasing levels of non-axisymmetric nacelle design freedom. Finally, the engine and wing were integrated in an over-the-wing configuration, and aeropropulsive optimizations were performed to minimize engine fuel consumption and understand the aeropropulsive trade-offs. Based on these studies, the following observations were made, which answer the research questions:

ISOLATED ENGINE OPTIMIZATIONS

- **What impact does the proposed parameterization have on the convergence of the engine optimization? What are the necessary tolerances and computational costs associated with these aeropropulsive optimizations?**

  For the baseline engine optimization using axisymmetric design variables, the coupled aeropropulsive optimization converged well within a reasonable number of optimizer iterations to an optimum design with very tight feasibility and optimality tolerances of 1e-6. The optimized design was feasible and consistent with both the disciplines. The convergence history reveals that an optimality constraint of 1e-4 is sufficient to obtain a reasonably converged design with just a 0.02% difference in the objective compared to a fully converged optimization. This baseline optimization verified the optimization setup and established a baseline for isolated engine optimizations. This optimization was performed on a 0.1 million mesh size and took 10.5 hours on 20 parallel cores.

- **How does the engine design change during an aeropropulsive optimization in the presence of a non-axisymmetric design space?**

  The engine was optimized for the same thrust with the freestream flow coming at an angle of 5° to verify the effectiveness of the non-axisymmetric nacelle parameterization. It was found that a full radial and longitudinal non-axisymmetric design freedom can eliminate shocks on the outer nacelle and reduce the inlet lip supervelocities. This non-axisymmetric design had a 0.37% improvement in engine fuel consumption rate compared to the axisymmetric design. This study demonstrated that the sensitivity of non-axisymmetric design changes for isolated engines is quite low, but the obtained qualitative flow improvements are important for reducing flow distortion. For a positive 5° angle of attack (upward), the nacelle shape has a positive (downward) droop angle.

- **How does the engine design change for varying levels of thrust requirement? Is the proposed parameterization able to handle these changes?**

  Adding an inequality constraint for the bypass ratio instead of keeping it fixed, had a countable reduction of 0.91% on the engine fuel consumption, so it was included in all later studies. A thrust variation study revealed that the optimum bypass remains around 8.73 for a fixed FPR of 1.65 in the range of 70-100kN thrust. The engine fuel consumption grows almost linearly in this region with an almost constant TSFC of about 14.3 g/kN/s. This thrust increase is entirely based on increasing the fan flow rate. But due to a constrained fan face mach number, this increase in mass flow rate is obtained by increasing the fan face area, which grows linearly with the mass flow rate. The proposed non-axisymmetric parameterization was very robust in handling all these design changes.

- **Are there any drawbacks of the proposed parameterization that might affect its usability?**

  The parameterization scheme devised in this work is flexible, robust and can be be applied to other closed surface designs like rockets. The design variables programmed for selective non-axisymmetric deformations can also be easily integrated into the current MACH-Aero framework to be used by the public. However, the initial setup for generating the FFDs in a proper overlap can be cumbersome. Also, the FFD sections are limited by a minimum number of mesh cells between the sections. Depending upon the problem, this could lead to a higher number of FFD section points, hence more shape design variables than desired. Although, this can be overcome by linking the movement of adjacent FFD sections to reduce the number of design variables.

INTEGRATED ENGINE-WING OPTIMIZATIONS

- **What is the effect of adding an engine placement DV on the location and performance of the integrated engine-airframe?**

  Three optimization studies were conducted with the over-the-wing mounted engine for the BWB. These studies examined the effects of engine placement and non-axisymmetric nacelle shape design variables. In the engine-airframe optimization at the baseline engine location, the optimizer reduced the strength of the strong shocks present in the contraction region between the nacelle and the engine but could not eliminate them entirely. The engine placement design variable had a significant impact on the performance of both the wing and the engine. Adding horizontal and vertical translation design variables to set the engine's relative position with respect to the wing improved engine fuel consumption by 2.32%. The optimized engine location is closer to the wing and near the trailing edge to weaken the contraction shocks while positioning the engine in the low-velocity flow near the wing trailing edge.

This location improves intake efficiency, as the incoming flow already has a lower velocity and higher static pressure than the freestream.

- **How do the non-axisymmetric DVs perform in an integrated engine-wing optimization? Is their effect any different from isolated engine optimizations?**

  Adding non-axisymmetric nacelle design variables to this optimization further improved the engine's fuel consumption by 1.1%. Both the inlet lip and the outer nacelle in this non-axisymmetric case were free from shocks. These results demonstrate that although the advantages of non-axisymmetric parameterization were not realized in isolated engine optimizations, they are of both qualitative and quantitative importance in the context of engine-wing integration.

- **What are the differences in the performance characteristics of the wing and engine when they are optimized in isolation versus in an integrated configuration?**

  A comparison between the independently optimized engine and wing designs and the optimized integrated design reveals a 3.89% improvement in engine fuel consumption for the same thrust when placed in an over-the-wing (OWN) configuration with the Blended Wing Body (BWB). This improvement is attributed to the diffused flow near the trailing edge, representing a significant enhancement in fuel efficiency. Additionally, it was observed that nacelle drag increases by more than 3.4 times in the integrated configuration compared to its isolated counterpart, while wing drag increases by 13.6%. Consequently, the engine thrust must account for this increased drag. These observations underscore the importance of optimizing engine and wing designs in an integrated manner, as isolated optimizations fail to capture the significant differences in overall system performance.

- **Are there any design features that are present in the optimized integrated designs that can otherwise be overlooked when optimizing the engine and wing in isolation?**

  The isolated engine optimizations at a 5°AoA showed that the nacelle shape would have a positive droop for a positive angle of attack. The optimized over-the-wing nacelle has a positive droop for an incoming flow at a negative AoA as the flow travels down to the wing's trailing edge. The optimizer shortens the lower lip to relieve the shock in the contraction region and reduce drag on both the wing and the nacelle. This alleviates some of the lift degradation at the inboard wing, but the engine still stays close to the wing to benefit from the diffused flow over the wing. The optimized wing sections for the engine-integrated case have a lower twist than the isolated wing. This is because the inboard twist is restricted by the presence of the engine. The inboard airfoils near the engine have an upward trailing edge reflex to reduce the shock strength in the contraction region. These design features are absent in isolated engine-wing optimizations and demonstrate the design differences which can be easily overlooked in isolated wing and propulsion optimization.

5.3. RECOMMENDATIONS FOR FUTURE WORK

Based on the findings and conclusions presented in this thesis, several recommendations can be made for future research and practical applications in the field of aeropropulsive design optimization. These recommendations aim to enhance the understanding and effectiveness of integrated engine-airframe configurations, address the limitations encountered in this study, and suggest potential directions for further investigation and improvement.

1. The optimization studies performed in this thesis use a relatively coarse mesh. Although the studies show similar trends between fine and coarse optimizations, finer mesh results are required to capture the flow physics more accurately.

2. The coupled gradient calculations in the MACH-Aero framework were set-up manually. These calculations can be automated. A similar effort is being undertaken for the MPhys framework.

3. The meshes used for isolated engine and wing optimizations were of very high quality. But the engine-airframe mesh underwent significant deformation during the engine placement, leading to highly skewed cells. Although this structured mesh approach is more robust than the overset mesh, a new mesh should be constructed after the identification of an approximate initial location of the engine w.r.t the wing.

4. Due to the complexity of implementation involved with the FFD-based parameterization and its propensity to lead to a larger than expected number of design variables for the overlapping cases, it is recommended to develop a simpler parameterization method, while keeping all the design freedom that this parameterization provides.

5. Based on the encouraging results of over-the-wing nacelle placement and the benefits of the aeropropulsive trade studies, it is recommended to perform such coupled aeropropulsive optimization studies for other aircraft configurations, using engine placement and non-axisymmetric design variables.

6. The non-axisymmetric engine design obtained in the engine-airframe integration case in this study could be difficult to manufacture. A use of left-right symmetry is recommended for future studies, which is also implemented in the current parameterization scheme.

7. This study did not take into account some disciplinary constraints, like static longitudinal stability and also did not include other disciplines. Since, longitudinal stability constraints are critical for BWBs which lack a tail, it is highly recommended to use a trim constraint. This should also take into account the weights and CGs of the components to estimate correct moments due to the engine mass and thrust.

8. The engine design considered in this study is restricted by a minimum thickness constraint of 0.99 due to the unavailability of a structural solver to determine the thickness and mass of the engine components. It is recommended to develop an open-source structural sizing tool for engine design, like NASA's WATE++.

9. The current study does not take into account a distortion constraint for the fan face. It is recommended to perform similar optimization studies with a distortion constraint to observe its effect on the engine placement and non-axisymmetric nacelle design.

10. The engine and wing need to satisfy the performance constraint at different conditions of the flight. This study focused only on a single-point optimization. In addition to the cruise flight, The nacelle thickness is also constrained by its performance on the ground, and the engine by its thrust at the top of climb. Hence, future studies should consider multi-point optimizations.

6

APPENDIX-A

A verification study was performed to check the smoothness of the underlying surface under deformation when overlapping FFDs are used. Figure 6.1 shows the overlap strategy and the results of this verification. First, a single FFD was used to deform a rectangular domain by moving only a single FFD point downward by one unit length. In a second study, two child FFDs were overlapped under the global parent FFD and their overlapping FFD points were moved by half a unit length. Both the FFD movements produced very similar deformations in the wall. This shows that the resulting deformation is a superposition of the individual FFD movements. Although, these deformations were not exactly the same, but they were continuous. No sudden changes were observed in the curvature of the wall. The two deformations do not need to match exactly, but the only the underlying surface deformations need to be smooth. This property of superposition of the FFD sections is utilized to construct the proposed overlapping FFD-based engine parameterization in this study.

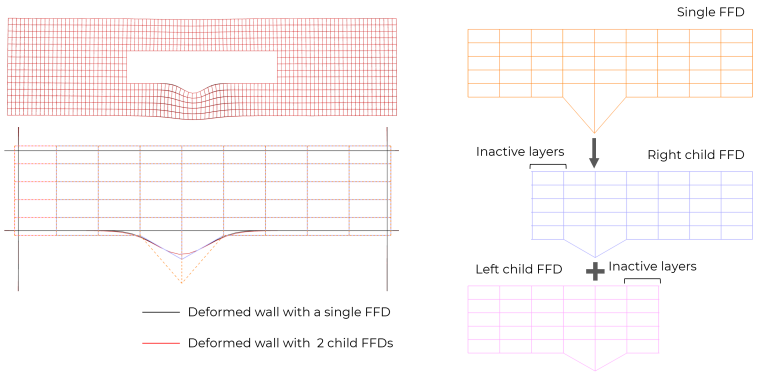

Figure 6.1: Verification of overlapping FFDs for smooth deformation

BIBLIOGRAPHY

[1] "Hydrogen powered aviation: A fact-based study of hydrogen technology, economics, and climate impact by 2050". In: *Fuel Cells and Hydrogen 2 Joint Undertaking* (2020). DOI: doi/10.2843/471510.

[2] P. D. Bravo-Mosquera, F. M. Catalano, and D. W. Zingg. "Unconventional aircraft for civil aviation: A review of concepts and design methodologies". In: *Progress in Aerospace Sciences* 131 (2022), p. 100813. ISSN: 0376-0421. DOI: https://doi.org/10.1016/j.paerosci.2022.100813.

[3] IATA. *International Air Transport Association: Aircraft Technology - Net Zero Roadmap*. 2023. URL: https://www.iata.org/en/programs/environment/roadmaps.

[4] R. H. Liebeck. "Design of the blended wing body subsonic transport". In: *Journal of aircraft* 41.1 (2004), pp. 10–25.

[5] C. L. Nickol and L. A. McCullers. "Hybrid wing body configuration system studies". In: *47th AIAA aerospace sciences meeting including the new horizons forum and aerospace exposition*. 2009, p. 931.

[6] C. Zhenli, M. Zhang, C. Yingchun, S. Weimin, T. Zhaoguang, L. Dong, and B. Zhang. "Assessment on critical technologies for conceptual design of blended-wing-body civil aircraft". In: *Chinese Journal of Aeronautics* 32.8 (2019), pp. 1797–1827.

[7] E. J. Adler and J. R. Martins. "Blended wing body configuration for hydrogen-powered aviation". In: *Journal of Aircraft* (2024), pp. 1–15.

[8] F. Tejero, R. Christie, D. MacManus, and C. Sheaf. "Non-axisymmetric aero-engine nacelle design by surrogate-based methods". In: *Aerospace Science and Technology* 117 (2021), p. 106890.

[9] A. Renganathan, S. H. Berguin, M. Chen, J. Ahuja, J. C. Tai, D. N. Mavris, and D. Hills. "Sensitivity analysis of aero-propulsive coupling for over-wing-nacelle concepts". In: *2018 AIAA Aerospace Sciences Meeting*. 2018, p. 1757.

[10] E. S. Hendricks and J. S. Gray. "pyCycle: A Tool for Efficient Optimization of Gas Turbine Engine Cycles". In: *Aerospace* 6.87 (Aug. 2019). DOI: 10.3390/aerospace6080087.

[11] J. Gray. "Design optimization of a Boundary Layer Ingestion propulsor using a coupled aeropropulsive model". PhD thesis. 2018.

[12] A. Yildirim, J. S. Gray, C. A. Mader, and J. R. Martins. "Coupled aeropropulsive design optimization of a podded electric propulsor". In: *AIAA AVIATION 2021 FORUM*. 2021, p. 3032.

[13] M. G. Turner, A. Norris, and J. P. Veres. “High-fidelity three-dimensional simulation of the GE90”. In: *33rd Fluid Dynamics Conference and Exhibit*. NASA/TM-2004-212981. 2004.

[14] A. Stuermer. “Dlr tau-code urans turbofan modeling for aircraft aerodynamics investigations”. In: *Aerospace* 6.11 (2019), p. 121.

[15] J. S. Gray, A. Yildirim, C. Mader, and J. Martins. “An Aeropropulsive Test Problem: Coupling CFD Simulations with a Propulsion Model”. In: *AIAA Aviation 2020*. 2020.

[16] A. H. Lamkin, A. Yildirim, J. R. Martins, and N. A. Wukie. “Advancements in Coupled Aeropropulsive Design Optimization for High-Bypass Turbofan Engines”. In: *AIAA AVIATION 2023 Forum*. 2023, p. 3591.

[17] M. A. S. Abdul-Kaiyoom, A. Yildirim, and J. R. Martins. “Coupled Aeropropulsive Design Optimization of an Over-Wing Nacelle Configuration”. In: (). DOI: 10.2514/6.2023-0327. eprint: https://arc.aiaa.org/doi/pdf/10.2514/6.2023-0327. URL: https://arc.aiaa.org/doi/abs/10.2514/6.2023-0327.

[18] P. E. Gill, W. Murray, and M. A. Saunders. “SNOPT: An SQP Algorithm for Large-Scale Constrained Optimization”. In: *SIAM Journal on Optimization* 12.4 (2002), pp. 979–1006. DOI: 10.1137/S1052623499350013. URL: https://doi.org/10.1137/S1052623499350013.

[19] J. T. Hwang and J. R. Martins. “A computational architecture for coupling heterogeneous numerical models and computing coupled derivatives”. In: *ACM Transactions on Mathematical Software (TOMS)* 44.4 (2018), pp. 1–39.

[20] H. M. Hajdik, A. Yildirim, E. Wu, B. J. Brelje, S. Seraj, M. Mangano, J. L. Anibal, E. Jonsson, E. J. Adler, C. A. Mader, G. K. W. Kenway, and J. R. R. A. Martins. “pyGeo: A geometry package for multidisciplinary design optimization”. In: *Journal of Open Source Software* 8.87 (2023), p. 5319. DOI: 10.21105/joss.05319.

[21] F. Tejero, D. MacManus, and C. Sheaf. “Impact of droop and scarf on the aerodynamic performance of compact aero-engine nacelles”. In: *AIAA Scitech 2020 Forum*. 2020, p. 1522.

[22] J. R. R. A. Martins and A. Ning. *Engineering Design Optimization*. Cambridge, UK: Cambridge University Press, Jan. 2022. ISBN: 9781108833417. DOI: 10.1017/9781108980647. URL: https://mdobook.github.io.

[23] D. Rodriguez. “A multidisciplinary optimization method for designing inlets using complex variables”. In: *8th Symposium on Multidisciplinary Analysis and Optimization*. 2000, p. 4875.

[24] D. L. Rodriguez. “Multidisciplinary optimization method for designing boundary-layer-ingesting inlets”. In: *Journal of Aircraft* 46.3 (2009), pp. 883–894.

[25] V. T. Silva, A. Lundbladh, C. Xisto, and T. Grönstedt. "Over-wing integration of ultra-high bypass ratio engines: A coupled wing redesign and engine position study". In: *Aerospace Science and Technology* 138 (2023), p. 108350.

[26] J. Hueso-Rebassa, D. MacManus, F. Tejero, I. Goulos, F. Sánchez-Moreno, and C. Sheaf. "Design optimisation of non-axisymmetric exhausts for installed civil aero-engines". In: *Aerospace Science and Technology* 142 (2023), p. 108700.

[27] F. Tejero, D. MacManus, I. Goulos, and C. Sheaf. "Propulsion integration study of civil aero-engine nacelles". In: *The Aeronautical Journal* 128.1320 (2024), pp. 325–339.

[28] J. S. Gray, C. A. Mader, G. K. Kenway, and J. R. Martins. "Coupled aeropropulsive optimization of a three-dimensional boundary-layer ingestion propulsor considering inlet distortion". In: *Journal of Aircraft* 57.6 (2020), pp. 1014–1025.

[29] A. Yildirim, J. S. Gray, C. A. Mader, and J. R. Martins. "Boundary-layer ingestion benefit for the STARC-ABL concept". In: *Journal of Aircraft* 59.4 (2022), pp. 896–911.

[30] J. Ahuja, C. Hyun Lee, C. Perron, and D. N. Mavris. "Comparison of Overwing and Underwing Nacelle Aeropropulsion Optimization for Subsonic Transport Aircraft". In: *Journal of Aircraft* 61.2 (2024), pp. 638–653.

[31] C. A. Mader, G. K. Kenway, A. Yildirim, and J. R. Martins. "ADflow: An open-source computational fluid dynamics solver for aerodynamic and multidisciplinary optimization". In: *Journal of Aerospace Information Systems* 17.9 (2020), pp. 508–527.

[32] G. K. W. Kenway, C. A. Mader, P. He, and J. R. R. A. Martins. "Effective Adjoint Approaches for Computational Fluid Dynamics". In: *Progress in Aerospace Sciences* 110 (Oct. 2019), p. 100542. DOI: 10.1016/j.paerosci.2019.05.002.

[33] A. Yildirim, G. K. W. Kenway, C. A. Mader, and J. R. R. A. Martins. In: *Journal of Computational Physics* (), p. 108741. ISSN: 0021-9991. DOI: 10.1016/j.jcp.2019.06.018.

[34] G. J. Kennedy and J. R. Martins. "A parallel aerostructural optimization framework for aircraft design studies". In: *Structural and Multidisciplinary Optimization* 50 (2014), pp. 1079–1101.

[35] A. Christison Gray. *Geometrically Nonlinear High Fidelity Aerostructural Optimisation for Highly Flexible Wings*. 2020. URL: http://resolver.tudelft.nl/uuid:1a6b5001-d213-40d9-bc2c-5e831eda527d.

[36] Z. Lyu and J. R. Martins. "Aerodynamic design optimization studies of a blended-wing-body aircraft". In: *Journal of Aircraft* 51.5 (2014), pp. 1604–1617.

[37] B. Larrimer. *Beyond Tube-and-wing: The X-48 Blended Wing-body and NASA's Quest to Reshape Future Transport Aircraft*. NASA aeronautics book series. NASA, 2020. ISBN: 9781626830585. URL: https://books.google.nl/books?id=Ps08zQEACAAJ.

[38] R. Liebeck, M. Page, and B. Rawdon. “Blended-wing-body subsonic commercial transport”. In: *36th AIAA aerospace sciences meeting and exhibit*. 1998, p. 438.

[39] B. J. Cantwell. *The GE90 - An Introduction*. 2010. URL: https://www.kimerius.com/app/download/5781574315/The+GE90+-+An+introduction.pdf.

[40] K. Daniel and Bianfable. *From which stages is the bleed air from a GE90?* 2019. URL: https://aviation.stackexchange.com/a/67986.

[41] P. Derakhshandeh, A. Ahmadi, and R. Dashti. “Simulation and technical-economic-environmental optimization of the General Electric GE90 hydrogen turbofan engine”. In: *International Journal of Hydrogen Energy* 46.5 (2021), pp. 3303–3318.

[42] P.-J. Proesmans. “Preliminary Propulsion System Design and Integration for a Box-Wing Aircraft Configuration: A Knowledge Based Engineering Approach”. In: (2019). URL: http://resolver.tudelft.nl/uuid:0d2ebc46-09ee-493f-bb4c-c871133bff6f.

[43] A. B. Lambe and J. R. Martins. “Extensions to the design structure matrix for the description of multidisciplinary design, analysis, and optimization processes”. In: *Structural and Multidisciplinary Optimization* 46 (2012), pp. 273–284.

[44] J. G. Coder, T. H. Pulliam, D. Hue, G. K. Kenway, and A. J. Sclafani. “Contributions to the 6th AIAA CFD drag prediction workshop using structured grid methods”. In: *55th AIAA Aerospace Sciences Meeting*. 2017, p. 0960.

[45] P. Proesmans. *Preliminary Propulsion System Design and Integration for a Box-Wing Aircraft Configuration*. 2019. URL: http://resolver.tudelft.nl/uuid:0d2ebc46-09ee-493f-bb4c-c871133bff6f.

[46] N. Secco, G. K. W. Kenway, P. He, C. A. Mader, and J. R. R. A. Martins. “Efficient Mesh Generation and Deformation for Aerodynamic Shape Optimization”. In: *AIAA Journal* (2021). DOI: 10.2514/1.J059491.

[47] E. Luke, E. Collins, and E. Blades. “A fast mesh deformation method using explicit interpolation”. In: *Journal of Computational Physics* 231.2 (2012), pp. 586–601.

[48] E. Wu, G. Kenway, C. A. Mader, J. Jasa, and J. R. R. A. Martins. “pyOptSparse: A Python framework for large-scale constrained nonlinear optimization of sparse systems”. In: *Journal of Open Source Software* 5.54 (2020), p. 2564. DOI: 10.21105/joss.02564.